POLITECNICO
MILANO 1863

SCUOLA DI INGEGNERIA INDUSTRIALE
E DELL'INFORMAZIONE

Engineering of Rashba spin textures in chalcogenide alloys

Tesi di Laurea Magistrale in
Physics Engineering - Ingegneria Fisica

Author: **Federico Belponer**

Student ID: 945658
Advisor: Prof. Matteo Cantoni
Co-advisors: Christian Rinaldi
Academic Year: 2020-21

Abstract

Spintronics focuses on the integration of the spin degree of freedom in conventional electronics, pushed by the increased demand for computational power density. In order to do so, materials with new functionalities have been investigated to find energy-efficient conversion processes (e.g. *spin to charge conversion* and *spin-orbit torque*) and multi-functional devices (e.g. *in-memory computing architecture*).
The research for new materials brought to the discovery of the FERSC class, whose father compound is GeTe, which shows an intrinsic multi-functionality. The interplay of ferroelectricity (non-volatility) and Rashba bands (spin-transport) was recently proved to take place in GeTe at room temperature, making the material suitable for spintronic devices. In general, other group-IV tellurides are eligible members of this class and among them, SnTe, which has been predicted to belong to this class, under appropriate constraints, while also belonging to the topological crystalline insulators class.
In this thesis, we present the studies conducted on the ternary alloy $Ge_xSn_{1-x}Te$ (GST): exploiting the structural similarity of SnTe with GeTe, we tried to engineer the electronic properties of the first by doping it with Ge atoms. The work consisted of the growth of the GeSnTe samples by molecular beam epitaxy and the characterization of them by means of spectroscopic techniques, either to investigate their chemical and crystalline structure or to study their electronic bands with spin-resolved techniques (S-ARPES).
The studies show how the presence of Ge atoms stabilizes the ferroelectric phase of the alloy up to room temperature, much higher with respect to the pure SnTe (Curie temperature of 100 K). We found that GST presents an increasing Rashba band splitting with the increase of Ge doping, thus allowing for modulation of transport properties by doping. These results are supported by independent density functional theory (DFT) modelling reporting analogous results.
The opportunity to characterize spin-to-charge conversion performances by means of direct in-situ spin-injection pushed us to improve the already existing experimental setup for the generation of a spin-polarized electron beam. The aim is to obtain a highly stable beam with a smaller spot size in order to make it compatible with patterned structures on the scale of 100 μm. The results of this part are also presented in the thesis work.

Keywords: Spintronics, FERSC, Topological Insulators, S-ARPES.

Sommario

La spintronica si concentra sull'integrazione del grado di libertà di spin nell'elettronica convenzionale, spinta dalla rinnovata richiesta di maggiore densità di calcolo. Per fare ciò, sono stati studiati nuovi materiali con nuove funzionalità, per trovare processi di conversione efficienti (e.g. *conversione spin-carica* e *spin-orbit torque*) e dispositivi multifunzionali (e.g. *architettura di computazione in-memory*).
Nel contesto di ricerca di nuovi materiali, la classe dei FERSC, di cui il componente padre è GeTe, si è mostrata avere una intrinseca multifunzionalità. L'interazione tra ferroelettricità (non-volatile) e bande Rashba (legate al trasporto di spin) è stato recentemente dimostrato in GeTe a temperatura ambiente, rendendolo adatto per dispositivi spintronici. In generale, altri telluridi del gruppo IV sono plausibili membri di questa classe e tra questi SnTe. SnTe appartiene già alla classe di isolanti topologici cristallini e, in opportune condizioni, è stato predetto essere anche FERSC.
In questa tesi, presentiamo gli studi fatti sulla lega ternaria $Ge_xSn_{1-x}Te$ (GST): sfruttando la somiglianza strutturale di SnTe e GeTe, abbiamo provato ad ingegnerizzare le proprietà elettroniche del primo tramite drogaggio con Ge. Il lavoro è consistito nella crescita dei campioni tramite epitassia da fascio molecolare e nella loro caratterizzazione per mezzo di tecniche spettroscopiche, sia per investigarne la struttura chimica e cristallina che per studiarne le bande elettroniche con tecniche risolte in spin (S-ARPES).
Gli studi mostrano come la presenza di atomi di Ge stabilizzino la fase ferroelettrica della lega fino a temperatura ambiente, ben superiore rispetto al puro SnTe (temperatura di Curie pari a 100 K). Abbiamo dimostrato che GST presenta una crescente separazione delle bande Rashba con il drogaggio di Ge, quindi permettendo in questo modo di modularne le proprietà di trasporto. Questi risultati sono supportati da modelli di calcolo di densità funzionale (DFT) che hanno portato indipendentemente a risultati analoghi.
La possibilità di caratterizzare le performance di conversione spin-carica tramite una iniezione diretta di spin in vuoto ci ha spinti ad apportare miglioramenti al setup sperimentale già esistente per la generazione di un fascio elettronico polarizzato in spin. L'obbiettivo è ottenere un fascio di elettroni che sia altamente stabile ed abbia una dimensione inferiore a quella attuale, cosi da renderlo compatibile con strutture patternate

nell'ordine dei 100 μm. I risultati preliminari di questa sezione sono presentati anch'essi all'interno della tesi.

Contents

List of Figures

List of Tables

1 Introduction

In the last decades, the increase in computational power offered by the Complementary Metal-Oxide-Semiconductor (CMOS) electronics has been outstanding. This trend was sustained by the miniaturization of transistors, which is now facing a limit due to the minimum physical size of about 10 nm [64]. It was already pointed out by X. Xu et al. [109] that the CMOS downscaling is no more able to meet the increasing request of computational density and that "innovations in architecture, circuit and device are required instead."

This pushed the scientific community to look for different paths. One of these is *in-memory computing* architecture, which takes advantage of information processing performed within the same space used as a memory, thus reducing the need for data transfer between the computational unit and the memory. New functionalities have to be exploited in order to implement these type of devices: ferroelectricity, phase-change effects (e.g. for Resistive Switching RAM [42, 43]), spin orbit coupling effects (in the case of spin-orbitronics devices). At this scope, spin-orbit heterostructures have shown good preliminary results and one example is the Magneto-Electric Spin-Orbit logic (MESO) designed by Intel [63], which combines a nonvolatile memory element and a spin-orbit readout logic within the unit device.

Spintronics(i.e., spin-electronics) and *spin-orbitronics*(i.e., electronics which exploits spin-orbit interaction-based effects) aim to include the spin-degree of freedom in conventional electronics, both in storage and logic devices (spintronic logic) [92]. This field of studies has a strong interest in materials presenting the relativistic effect of Spin-Orbit Coupling (SOC), since they allow for the interplay of charge currents and spin currents. This effect can be found in heavy metals [84, 111], but also in semiconductors.

From this perspective, a class of semiconducting materials presenting SOC is the FErroelectric Rashba SemiConductors (FERSC). These materials are characterized by an intrinsic multi-functional nature, since they combine ferroelectricity and Rashba effect in a semiconductor [77].

FERSC were predicted in 2013 [25, 77] and the father compound of this class is germanium telluride (GeTe). The spin-to-charge conversion in GeTe [82] was proved to be control-

lable by mean of the ferroelectric switching [83]. Furthermore, the spin-locked tunable bands of GeTe were demonstrated to be present at room temperature [98], a fundamental requirement for applications. Some other material have joined the FERSC class in the meanwhile, such as oxide perovskite Bi_2WO_6 [26] and in general group IV monochalcogenides [90], e.g., SnTe.
SnTe is already known for being the father compound of Topological Crystalline Insulators (TCI) [41, 94], a sub-class of Topological Insulators (TI) [65], which are insulating materials with conducting surface states. These materials already showed high efficiency for spin-to-charge conversion (SCC) processes [61] due to their spin-locked topological surface states. The FERSC behaviour of SnTe, on the other hand, has not been studied yet, leaving a gap in the literature: the scope of the present work is to fill this gap.

FERSC investigation

In this work, we investigate the ternary alloy $Ge_xSn_{1-x}Te$ (GST) in order to engineer the band structure of SnTe with a varying Ge doping. A fundamental investigation of this alloy is presented, including the growth process and the chemical, structural, spectroscopic and ferroelectric characterization.
The activity of growth and in-situ characterization was mainly carried out at Polifab, the facility of Politecnico di Milano for the fabrication of micro and nanotechnology. The electronic band structure of GST was investigated ex-situ with ARPES spectroscopy at the Advanced Photoelectric Effect (APE) beamline at the Elettra Synchrotron radiation facility (Trieste). Density functional theory (DFT) calculations of the $Ge_xSn_{1-x}Te$ bands dispersion have been provided by collaborators at CNR-SPIN, UOS L'Aquila in order to support the experimental data.

Electron gun optimization

The characterization of spintronic materials can be performed by mean of electrical measurements, such as spin-to-charge conversion (SCC) experiments. The typical experiment consists in the indirect injection of a spin current in the sample through a ferromagnetic layer (e.g. Spin-pumping used for Fe/GeTe(111) heterostructure [82]). Direct injection of spin current, avoiding the need for the spin injecting layer, could be possible using a spin-polarized electron beam to induce spin-polarization unbalance in the sample. In order to do so, a spin polarized electron beam with a sufficiently small spot size and stability is needed. The setup present at Polifab offers such a beam [16], but some improvements in

performances were needed: easiness of use, dimension of the spot size and stability of the beam.
In this work, a new control unit for the electron optics system is presented, from the design of its electronic components to the characterization of the electron beam obtained. Furthermore, the obtained electron beam could also be used to perform studies on the conduction bands through spin-resolved Inverse Photoemission Spectroscopy (S-IPE) or experiments of spin dependent transmission across magnetic membranes for spin detection.

Thesis ouline

The thesis is structured as follows:

- **Chapter 2** presents the theoretical framework useful for the understanding of the involved materials. These consists in ferroelectricity (section 2.1), Rashba effect and spin-to-charge conversion mechanisms (section 2.2), Topological insulators (section 2.3), FERSC (section 2.4). In the final part (section 2.5), the two case studies of GeTe and SnTe are reported, with the state of art characterization and perspectives.
- **Chapter 3** deals with the experimental techniques used in order to grow and characterize, by mean of spectroscopic analysis and electric measurements, the ternary alloy of GST.
- **Chapter 4** presents the experimental results about the growth (section 4.1) and characterization (sections 4.2 and 4.3) of $Ge_xSn_{1-x}Te$ samples (varying the value x), in comparison with the theoretical prediction (section 4.4).
- **Chapter 5** presents the work regarding the electron gun control unit, from the design of the control electronics (section 5.2) to the characterization of its performances on the electron beam (section 5.3).
- **Chapter 6** draws the conclusions of the work and gives some future perspectives.

2 | Ferroelectric Rashba semiconductors

This chapter is devoted to the theoretical insights into the class of materials involved in this work: Ferroelectric Rashba Semiconductors (FERSC). After presenting the phenomenology and theoretical modelling of ferroelectricity (section 2.1), the Rashba effect (section 2.2) is introduced and finally their combination in GeTe and FERCSs materials in general (section 2.4). An approach to Topological insulators and to their distinguishing properties is given in section 2.3. In the final section the two materials from which the work started, namely germanium telluride (GeTe) and tin telluride (SnTe), are presented, with their state of art characterization (section 2.5) and discussing the expected properties when they are combined together.

2.1. Ferroelectricity

Ferroelectricity is defined as the property of materials in which a spontaneous electric polarization $\mathbf{P}$ is present and can be reversed by the application of an external electric field stronger than the coercive field E_c. This polarization is given by the intrinsic lattice polarization of crystalline materials, originating from the lack of inversion symmetry.
Electric polarization has been proved to persist both in time and down to very small size ($\sim nm$), allowing for developing applications in the field of memories [102] and other nano devices. Some applications of ferroelectricity to electronics can be found in ferroelectric transistors [18, 39] and ferroelectric tunneling junctions [114].
More than 700 ferroelectric materials have been already found [88], the most studied of which are oxides perovskites (such as LNO, or BTO [59]), for their robustness and practical applications [1], while semiconducting ferroelectrics, to which GeTe and SnTe belong, are an emerging field of study of last decades.

[1] The above mentioned applications are mainly based on insulating ferroelectrics.

2.1.1. Phenomenology

As a consequence of the change in orientation of the polarization **P**, an hysteresis loop P-E is observed and a *polarization state* can be defined by discriminating the two considered directions of **P**. This hysteresis loop can be characterized by two main properties, also shown in figure 2.1b:

- **Remanent polarization** P_r, being the value of polarization corresponding to zero external electric field.
- **Coercive field** E_c, being the field for which $\mathbf{P} = 0$ and above which **P** changes sign.

All ferroelectric materials also show piezoelectricity and pyroelectricity, meaning that strain or temperature variations, respectively, can induce a lattice distortion and thus a polarization, while the opposite is not true being ferroelectric materials a sub-class of the pyroelectric ones, as schematically shown in figure 2.1a.

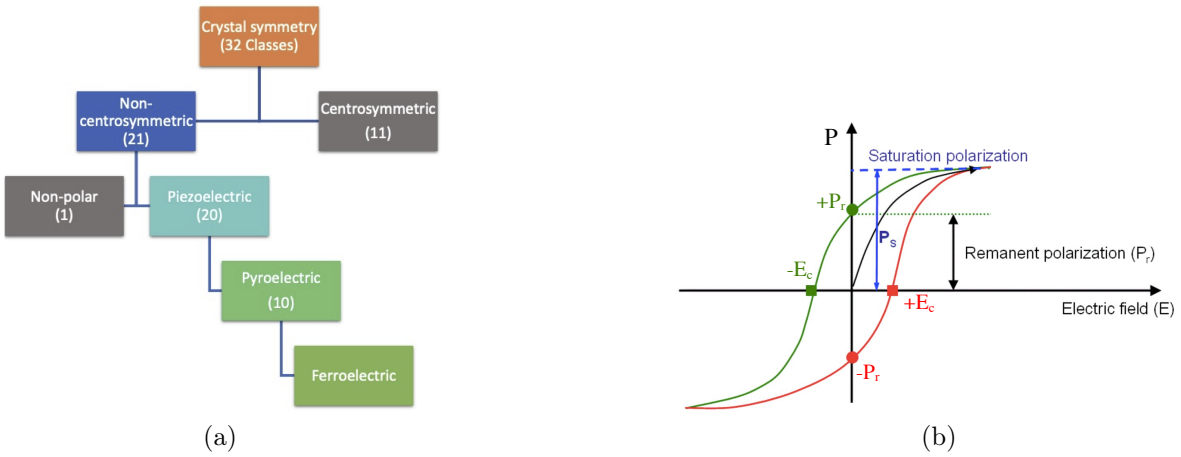

(a) (b)

Figure 2.1: (a) Schematic representation of piezoelectricity, pyroelectricity and ferroelectricity on the basis of crystal symmetry, adapted from [35]. (b) Example of polarization hysteresis loop showing the characteristic parameters for ferroelectric materials, namely the remanent polarization P_r, the coercive field E_c and the saturation polarization.

2.1.2. Theoretical frameworks: Landau-Devonshire model and modern ab-initio theories

The phenomenological description of the paraelectric-ferroelectric phase transition can be given, in analogy to the para-ferromagnetic one, by the Landau theory for second order phase transitions (namely those transitions in which a thermodynamic quantity varies continuously). Landau theory is a mean field theory, meaning that a high-dimensional

stochastic system with many interacting components is studied by mean of a simpler model in which different contributions are averaged, thus reducing its complexity to a single-body problem. This approach neglects local fluctuations of thermodynamic variables in favour of an overall simpler description. It follows that Landau's theory is only capable of a macroscopic description, while a microscopic insight of this phenomenon requires fully quantum mechanical calculations, as performed in the modern theory of ferroelectrics by Resta and Vanderbilt [81], whose work goes beyond the scope of this chapter.

For the case of ferroelectrics, the first application of Landau theory comes from Devonshire, from which the name of Landau-Devonshire theory [24]. Starting by considering the thermodynamic state of a bulk ferroelectric material as a function of temperature (T), polarization (P), external electric field (E) and strain, an order parameter of the system must be introduced in order to give an analytical expression for the free energy. This parameter is the quantity characterizing the phase transition (i.e. being zero in one phase and different form zero in the other) and corresponds to the electric polarization in ferroelectrics. The free energy of the system $\mathcal{F}_p$ is written as a function of the order parameter, as reported in equation (2.1), and the equilibrium configuration for the system is obtained minimizing it with respect of that same parameter:

$$\mathcal{F}_p = \frac{1}{2}aP^2 + \frac{1}{4}bP^4 - EP \tag{2.1}$$

with equilibrium condition

$$E_{eq} = aP_0 + bP_0^3 \tag{2.2}$$

The simplest expression for the a and b parameters, obtained empirically, is $a = a_0(T - T_0)$ and $b = b_0$. A second order phase transition is predicted by these equations as for $T \geq T_0$ a single minimum with $P = 0$ is predicted, while for $T < T_0$ two equal minima with opposite polarization $P \neq 0$ are present, as shown in figure 2.2a. The T_0 is identified as the Curie Temperature, $T_c = T_0$, of the transition. While this first approach is useful for the understanding and qualitative representation of the process, it doesn't allow for quantitative predictions, such as the values of polarization and Curie temperature, and only provides a macroscopic view of bulk materials. Landau-Ginzburg theory further develops the Landau-Devonshire theory by including local fluctuations of polarization in the model [17]. In order to study low dimensional systems, boundary conditions are included in the Landau-Ginzburg model, as shown in [19].

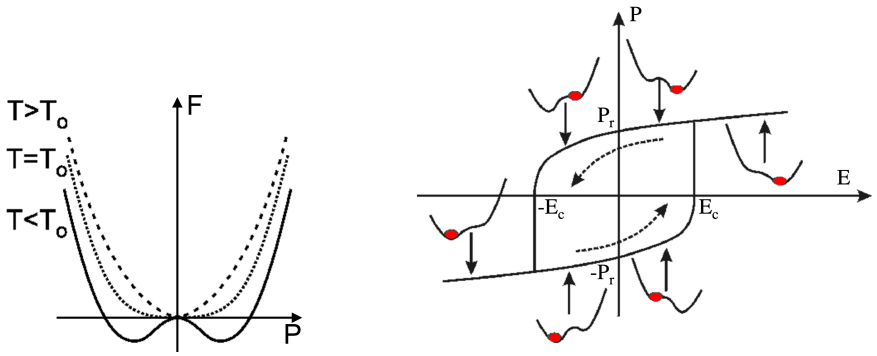

Figure 2.2: (a) Free energy for a continuous second order phase transition as a function of the electric polarization, considered as the order parameter. The dotted line for $T > T_0$ corresponds to the paraelectric phase, while the solid line corresponds to the ferroelectric phase at $T < T_0$. (b) Hysteresis loop for the electric polarization in the ferroelectric phase, with the external electric field dependent curves of the free energy. The remanent polarization P_r and the coercive field E_c are indicated on the figure. Adapted from [19].

2.2. Rashba splitting and connected effects

Rashba effect is a relativistic effect caused by the spin-orbit coupling (SOC) in non-centrosymmetric systems that leads to a momentum dependent energy shift for the two states of spin polarization. This loss of spin degeneracy is more evident in heavy atoms, which present a stronger SOC. The effect is activated by an externally applied electric field, thus allowing for tuning of spin properties of the bands and so affecting the spin-to-charge conversion (SCC) mechanisms.

2.2.1. Theoretical overview of Rashba effect

A first understanding of the Rashba Effect can be given by a two dimensional free electron gas (2DEG) system, in which the inversion symmetry is broken by an externally applied electric field perpendicular to the plane of motion of electrons. Electrons are confined in the xy-plane and moving at relativistic speed $\mathbf{v}$, so that they experience a magnetic field, in their frame of motion, according to the Lorentz transformation between different coordinate frames.

$$\mathbf{B} = \frac{\mathbf{E} \times \mathbf{v}}{c^2 \sqrt{1 - \frac{v^2}{c^2}}} \tag{2.3}$$

The magnetic field $\mathbf{B}$ defines the quantization axis for the electron and couples to its spin magnetic momentum $\mu_s = -g_s \mu_B \boldsymbol{\sigma}$ (where $\boldsymbol{\sigma}$ is the Pauli matrix for the spin operator

$\mathbf{S} = \frac{1}{2}\boldsymbol{\sigma}$) through the Zeeman interaction[2], having the following form:

$$H_{Zeeman} = -\boldsymbol{\mu}_s \cdot \mathbf{B} \tag{2.4}$$

So that combining equation (2.3) and equation (2.4) one obtains the resulting form for the SOC hamiltonian:

$$\begin{aligned} H_{SOC} &= \frac{e\hbar}{4m^2c^2}(\mathbf{E} \times \mathbf{p}) \cdot \boldsymbol{\sigma} = \\ &= -\frac{e\hbar}{4m^2c^2}\mathbf{E} \cdot (\boldsymbol{\sigma} \times \mathbf{p}) = \\ &= \boldsymbol{\alpha}_R \cdot (\boldsymbol{\sigma} \times \mathbf{k}), \end{aligned} \tag{2.5}$$

being $\mathbf{p} = \hbar\mathbf{k}$ for free electrons in a 2DEG. The Rashba field $\boldsymbol{\alpha}_R = \alpha_R \cdot \mathbf{z}$ is proportional to **-E**, depends on the considered system and its characteristic parameters (effective mass of the electron, energy gap, intensity of SOC).
The electronic bands result from the solution of the eigenvalue problem of the total Hamiltonian including the Rashba term:

$$det(H - EI) = det[(H_0 + H_R) - EI] = 0 \tag{2.6}$$

From which one obtains:

$$E_{\pm} = \frac{\hbar^2 k^2}{2m} \pm \alpha_R |k| \tag{2.7}$$

being k the wave-vector of electrons, m their effective mass (being their rest mass in the case of free electrons) and α_R the Rashba parameter. The additional term in the total H transforms the electronic bands of the 2DEG from a parabola with two-fold degeneracy with respect to the spin, given by the first term in equation (2.7), to two parabolas split in term of spin and wave-vector, as shown in figure 2.3c.

Given the eigenvalues, the eigenstates $\psi_{\pm}$ of the system can be computed from the equation:

$$\begin{aligned} H\,|\psi_+\rangle &= E_+\,|\psi_+\rangle \\ H\,|\psi_-\rangle &= E_-\,|\psi_-\rangle \end{aligned} \tag{2.8}$$

The expectation value [3] for the spin vector is always orthogonal to the electron's wave vector, as presented in figure 2.3c, with a spin texture circulating in k-space with opposite chirality for the E_+ and E_-. The components of the spin polarization are computed in

[2]The difference with respect to the actual Zeeman interaction is that in this case, no static externally applied magnetic field is present and therefore also the outcoming hamiltonian for SOC will be similar but not the same as for the Zeeman effect

[3]The expectation value for an observable A in a state ψ_+ corresponds to $\langle A \rangle_{\psi_+} = \langle \psi_+ | A | \psi_+ \rangle$

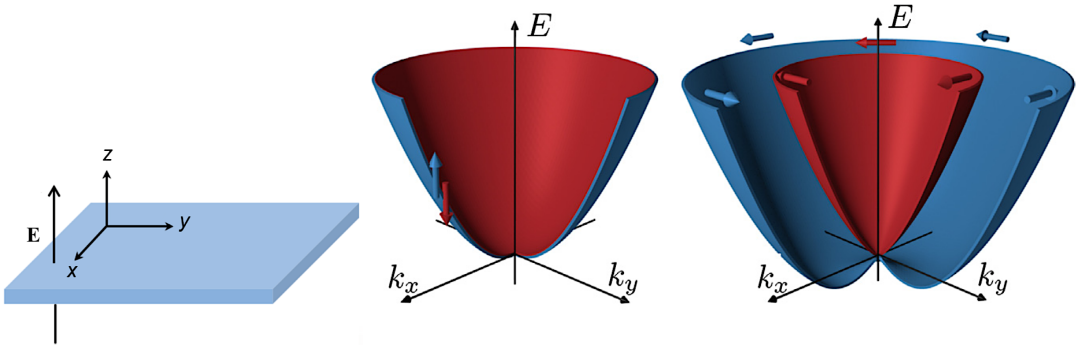

(a) (b) (c)

Figure 2.3: (a) Reference frame for a 2DEG system with externally applied electric field in the z-direction. (b) Electronic bands for the 2DEG before breaking the symmetry of the system by applying the electric field as in (c).

equation (2.9), referring to one of the two Rashba bands (the other shows opposite sign).

$$\begin{aligned} \langle \sigma_x \rangle_{\psi_+} &= \frac{k_y}{|k|} = \sin\theta_k \\ \langle \sigma_y \rangle_{\psi_+} &= \frac{k_x}{|k|} = -\cos\theta_k \\ \langle \sigma_z \rangle_{\psi_+} &= 0. \end{aligned} \tag{2.9}$$

The presence of a directional relation between spin and momentum, also called spin texture, takes the name of *spin-momentum locking* of the energy bands.
From a practical point of view, this band splitting can be seen as a **k**-dependent effective magnetic field which is affecting the carrier's velocity depending on its spin, thus leading to spin-to-charge conversion mechanisms (section 2.2.2).
The Rashba spin splitting can also be found as an intrinsic property for some semiconducting materials such as BiTeI [103] and GeTe [57]. These systems present Rashba splitting in their bulk states, differently to most of Rashba systems that present the splitting in their surface states, allowing for an increased robustness of the phenomenon. Moreover, the bulk spin splitting is caused by an internal field resulting from the breaking of the inversion symmetry in the crystal, also causing the ferroelectricity of the material, making it non-volatile and tunable.

2.2.2. Coupling between spin and charge currents

Non magnetic systems presenting a strong SOC can be exploited for the generation of spin currents from charge currents. High efficiency for SCC can be found in heavy metals (Pt and Ta [84, 111]), Rashba systems [69] and topological insulators [61]. Being able to

tune this interconversion by mean of external fields allows for reconfigurable spin logic devices [63] and so makes these materials appealing for spin-orbitronics applications.
The model used to describe the spin and charge current has been developed by Valet and Fert in 1993 [96] using the *two channels approximation*, in which the conduction takes place in indipendent channels for the spin up $(\uparrow) and spin down (\downarrow) electrons$.
$Defining the charge current (\mathrm{J}_c)$ as the net flux of charges through a surface S in the unit of time:

$$J_c = \frac{e}{N}\frac{dN}{dt} \tag{2.10}$$

the spin up (down) current can be defined by analogy as the flux of spin:

$$J_{\uparrow(\downarrow)} = \frac{\hbar}{N}\frac{dN_{\uparrow(\downarrow)}}{dt} \tag{2.11}$$

In order to express the spin current with same units of the charge one, it must be multiplied by the Josephson constant $(2e/\hbar)$ and the net charge (J^c) and spin (J^s) currents can be written as:

$$\begin{aligned} J^c &= J_\uparrow + J_\downarrow \\ J^s &= J_\uparrow - J_\downarrow \end{aligned} \tag{2.12}$$

Going to the three dimensional case, charge current is represented by a vector, while the spin current by a tensor both representing the flow direction and spin polarization components. Differently from the charge current, the spin one is invariant with respect to time inversion, making it a dissipationless current.
During propagation, electrons undergo scattering events that can both affect the charge velocity and spin orientation (spin-flip events), determining a diffusive propagation for both types of currents, described by the drift-diffusion model [27].
The effect of this propagation is the coupling between the two currents, leading to spin-charge interconversion by the mechanisms of spin Hall and Rashba-Edelstein effect.

Spin Hall Effect

The Spin Hall Effect (SHE) consists in the generation of spin currents from charge currents in paramagnetic SOC systems without the need of an external magnetic field. Considering a slab of material in the xy-plane, the electric field on the x-direction generates a pure spin current in the y-direction, with spin polarization along the z-axis (figure 2.4a).
This phenomenon has been first reported by M. I. D'yakonov and V. I. Perel [28] addressing the cause of the effect to spin-dependent scattering asymmetry due to SOC effect (e.g. charge carriers with spin up (↑) have higher probability to scatter towards the negative y direction than the spin down (↓)). The result is a spin accumulation on the sides of the

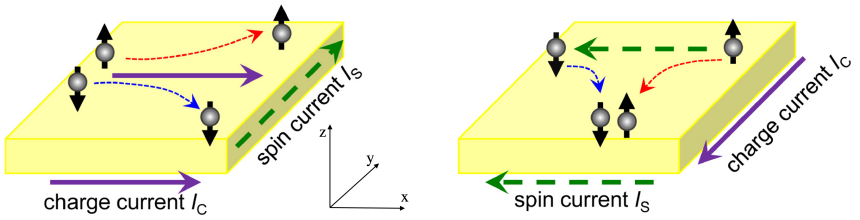

Figure 2.4: (a) Schematic representation of the SHE and (b) ISHE presenting the spin polarization along the z-direction.

slab, without any Hall voltage.

The opposite of this effect, known as Inverse Spin Hall Effect (ISHE), is shown in figure 2.4b. ISHE consists in the generation of a charge current as a consequence of a pure spin current flowing in the orthogonal direction. The origin for this effect is still the spin-dependent asymmetry of scattering events in the materials due to SOC.

The combination of these two effects plays a fundamental role in spin-based technologies [63] requiring generation and detection of pure spin currents, otherwise not detectable as readable voltages/currents.

The conversion between spin and charge current according to SHE and ISHE can be described as follows:

$$\mathbf{J}^{c,ISHE} = \theta_{SHE}\,\mathbf{J}^{s} \times \boldsymbol{\sigma} \tag{2.13}$$

were the $\boldsymbol{\sigma}$ is the unit vector for the direction of the spin and θ_{SHE} is the spin Hall angle, accounting for the conversion efficiency and proportional to the SOC intensity. In order to obtain an expression for θ_{SHE}, the spin Hall conductivity tensor σ_{ij}^{k} has to be considered (i, j, k can take values x, y, z):

$$\begin{aligned} \sigma_{xy}^{z} &= -\frac{J_{y,z}^{s}}{E_x} \\ \theta_{SHE} &= \frac{\sigma_{x,y}^{z}}{\sigma_{xx}} \end{aligned} \tag{2.14}$$

with $J_{y,z}^{s}$ the tensor for the spin current and σ_{xx} the conductivity along the charge current's channel.

Being the spin Hall angle proportional to the intensity of SOC, high conversion efficiency is found in heavy metals and their alloys (Pt, Ta, Au [53, 101]), but also in semiconductors like GaAs [51] and ZnSe [93], and 2DEG materials such as (110) AlGaAs quantum wells [89].

This effect can be differentiated by its origin:

- *intrinsic*, if caused by anomalous speed of electrons in the solid, depending on a

peculiar feature of electronic bands structure of a symmetry-broken crystal defined as Berry curvature [7].

- *extrinsic*, if caused by structural defects in crystals, causing skew scattering [36],related to the asymmetric scattering due to SOC on the impurity which changes the wave-vector direction, and side-jump scattering [56], preserving the wave-vector direction.

Rashba-Edelstein Effect

Rashba-Edelstein effect (REE) consists in the charge-to-spin current conversion in systems having a fixed dependence between carriers momentum and spin, such as Rashba 2DEG of the previous subsection. This effect has been initially discovered measuring a charge current as a consequence of a spin injection in the system, corresponding to the Inverse REE (IREE), and originally named Spin Galvanic Effect (SGE [32]). In such systems, a non-equilibrium spin density $\mathbf{S}$ generates a charge current density $\mathbf{J}_c^{IREE}$ [62]:

$$\mathbf{J}_c^{IREE} = -\frac{e\alpha_R \mathbf{z} \times \mathbf{S}}{\hbar} \tag{2.15}$$

while the opposite effect, the REE can be expressed as:

$$\mathbf{S} = \frac{\alpha_R \mathbf{z} \times \mathbf{J}_c}{e\hbar} \tag{2.16}$$

Experimentally, the spin accumulation $\mathbf{S}$ in IREE can be induced either optically or electrically [108].

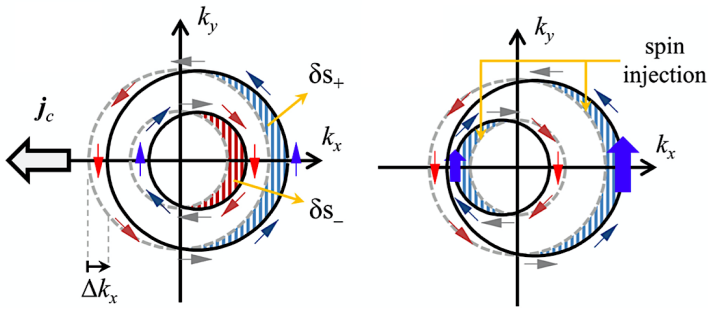

Figure 2.5: Representation of the Fermi contours of the Rashba bands for the (a) Rashba Edelstain Effect (REE) and (b) Inverse REE, with the unperturbed state represented by the dashed line and the state with currents flowing represented by the solid line. Adapted from [99].

The REE can be understood having a look at the Fermi contours of the Rashba bands presented in figure 2.5a: a charge current (J_c) injected at the interface along negative x induces a shift $\Delta k_x = -(e\tau/\sigma\hbar)J^c$ of both Fermi contours, resulting in a spin accumula-

tion polarized along the y-axis due to the inequivalence of the two contours. The opposite happens in the IREE, figure 2.5b, in which spin current is injected perpendicularly to the 2DEG with the spin polarization along the y-axis, so that the bands have to shift in order to accommodate the spin population, leading to a displacement of $\pm\Delta k_x$, corresponding to a net charge current perpendicular to the spin polarization unbalance.

2.3. Topological Insulators

Topology is a branch of mathematics that studies the properties of objects that are invariant under smooth transformations, for which a trivial example is a doughnut that can be transformed into a coffee cup, while it is topologically different from a solid sphere (not presenting any hole in its structure). This topological distinction can be also applied to solid-state physics and scientists started to classify phases of matter using topological order [105].
In recent years, a new class of materials, namely Topological Insulators (TI), was predicted to have quite fascinating properties originating by its topology [31, 47, 48]. A topological insulator (TI) presents, like ordinary insulators, a band gap in bulk states. However, on the surface (edge) states, these materials present conductive states that are protected by the time-reversal symmetry. Before introducing the Topological Crystalline Insulators (TCI) involved in this work, it is worth mentioning what the origin of these states is and what the protection of them by symmetry implies.

2.3.1. Morphology of Topological states

The characterization of whether a material is topological or not originates from band structure theory [12] on the base of the integer number called Chern number n [68]. The mathematical treatment of electronic bands in order to derive the Chern number goes beyond the scope of this thesis and it is enough to mention that different values of it identify different band structure topology. In order to understand the topological origin of these states, it is effective to consider two materials with different n, e.g. one with even n, being a trivial insulator, and the other with odd n, being a topological insulator.
When two such materials are put in contact, like in figure 2.6a, a discontinuity of n is created at the interface. Since the band structures of the two cannot smoothly deform one into the other, the system introduces some new states, localized at the surface, to relax the discontinuity.
This is the case of a TI in contact with a trivial insulator, but it also take place when a TI is in contact to vacuum, which is topologically trivial.

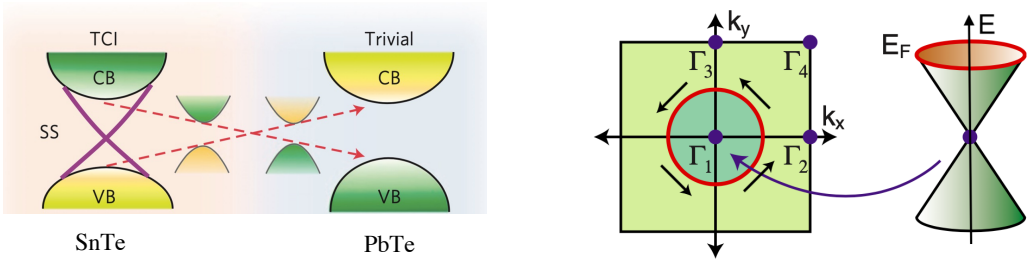

(a) (b)

Figure 2.6: (a) Band topology of two different material, being PbTe (trivial insulator) and SnTe (topological insulator). The bands symmetry (origin of the difference in Chern number) is highlighted in green and yellow and the contact between the two leads to the formation of the surface states (SS) highlighted in purple. In panel (b) the typical Fermi circle for a topological insulator is presented, with the spin polarization revolving around the Dirac cone (arrows describing the direction of it). Adapted from [94] and [37] respectively.

The origin of this topological difference resides in symmetry properties of a material, thus giving to these states protection against small deformations and defects.
Three main characteristics can be highlighted for topological surface states (TSS), whose example is reported in figure 2.6b:

- **Gapless Dirac cones**. TSS present the morphology of Dirac cones, with a energy distribution of massless particles.
- **Spin-momentum locking**. They are not degenerated with respect of spin with spin polarization rotating with the momentum **k** around the Fermi surface.
- **Symmetry protection**. They are protected by inversion $\mathcal{P}$ and time-reversal $\mathcal{T}$ symmetry.

The implications following these properties are many. The band dispersion of massless particles allows to obtain extremely energy efficient transport properties (theoretically dissipationless). The 2D massless Dirac hamiltonian is:

$$\mathcal{H}(\mathbf{k}-\mathbf{K}) = \hbar v_f(\mathbf{k}-\mathbf{K})\cdot\vec{\sigma} \tag{2.17}$$

with k the crystal momentum of electrons and K the momentum at the Dirac cone's centre.
The spin-momentum locking allows to obtain spin-to-charge conversion, e.g. using REE (section 2.2.2). The difference with respect to Rashba materials shown in figure 2.5 is that only one circular Fermi contour is shifting, thus giving even higher conversion efficiency.
The symmetry protection allows an electron in motion to be unaffected by the presence

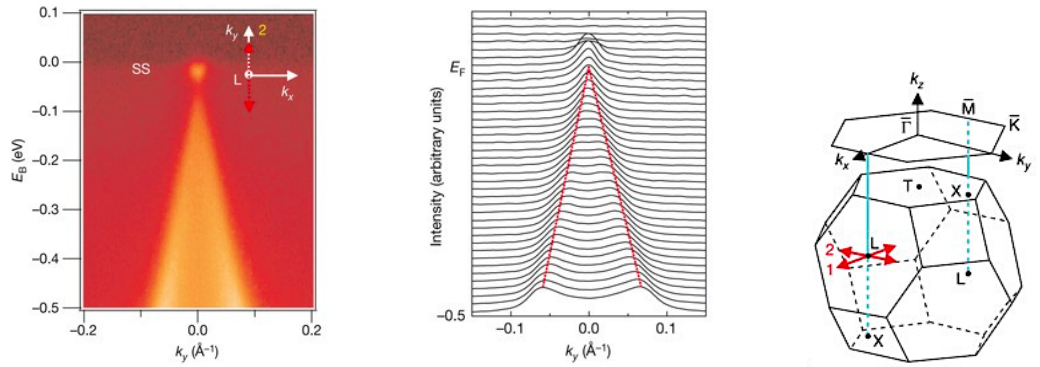

(a) (b) (c)

Figure 2.7: (a) ARPES intensity map for a **k**-space cut at the L point of the bulk 3D Brillouin zone for $Bi_{0.9}Sb_{0.1}$ and (b) the momentum distribution curve corresponding to the intensity map. The Brillouin zone for the considered sample is represented in panel (c). Adapted from [40].

of disorder since surface electrons cannot be localized as long as the bulk energy gap is present [72]. The protection of these states remains independently of the smoothness of an interface, because it originates from the change of the Chern number.

The first three dimensional TI to be identified has been the semiconducting alloy $Bi_{1-x}Sb_x$ [40], whose particular band structure has been observed by ARPES and is shown in figure 2.7. After this, it has been found that a main requirement for these material was strong spin-orbit coupling (enough to modify significantly the electronic structure), thus suggesting heavy metals with small bulk band gap.

The research for new materials culminated with the discovery of Bi_2Se_3 and Bi_2Te_3 [112] showing the same behaviour as their ancestor at higher temperatures thanks to the bigger bulk bandgap ($> 0.1\,\text{eV}$).

2.3.2. Topological Crystalline Insulators and SnTe family

A new class of materials has been predicted in 2010 [30, 41], to show the topological nature of electronic bands as a consequence of crystal symmetries. SnTe, in particular, was predicted to show an even number of Dirac cones on high-symmetry points of the Brilluoin zone and this was later demonstrated experimentally [94].

SnTe has a simple rocksalt structure and presents its bandgaps at the four equivalent L points of the fcc Brillouin zone. In [41] the proof of SnTe being a TCI is interestingly been performed by showing that PbTe has a trivial nature and using the topological argument of their Chern number being different: as discussed in section 2.3.1, two materials with different n belongs to different topological groups.

The difference in Chern number originates from their band structure (shown in fig-

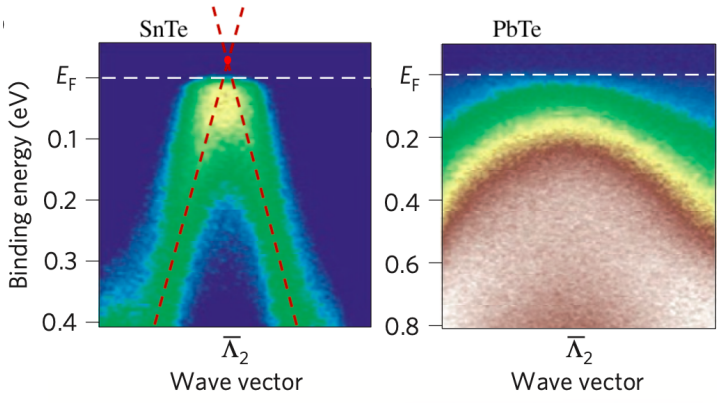

Figure 2.8: Experimental intensity maps, obtained through ARPES spectroscopy, for SnTe, showing Dirac cone-like band dispersion, and PbTe, showing the opening of a bandgap. Adapted from [94].

ure 2.6a): valence band of PbTe presents a strong Te contribution while in SnTe the strong Te contribution is found in conduction band, thus implying an inverted morphology of the band structures. The trivial nature of PbTe is obtained by the fact that its crystalline band structure can be smoothly connected to the atomic limit, in which Pb orbitals are empty and Te ones filled. By contrast, this proves that SnTe belongs to TI class, as also confirmed by the ARPES measurements shown in figure 2.8.
As it will be presented in section 2.5.2, the SnTe also presents a typical rhombohedral distortion along the [111] axis at low temperatures, making the crystal ferroelectric. In this configuration, the symmetry-breaking only removes two out of four Dirac cones present at different points of the Brillouin zone, therefore the material remains topological. The presence of a ferroelectric state with spin-momentum locked bands makes SnTe suitable as a FERSC material (section 2.4).
Topological insulators already found their application in spin-orbit torque (SOT) devices for improvements in efficiency, beyond the bulk spin-orbit coupling in heavy metals [107].

2.4. FERSCs

In the quest for combining different properties into the same material, a new class of materials has been found by density-functional theory [77]. These materials are the FerroElectric Rashba Semi-Conductors (FERSC), particular materials hosting three different as fundamental properties:

1. *Ferroelectricity*, allowing for the switchability of material's polarization by an electric field, as traditionally exploited in non-volatile memory elements,

2. *Rashba effects*, bringing in the spin-degree of freedom and opening the way to spintronics and SCC mechanisms,

3. *Semiconductivity*, granting the integration with existing semiconductor-based technology.

The interplay of these properties allows for new functionalities to be exploited, such as the control of the spin texture by mean of the intrinsic polarization of the material [83]. In order for a material to belong to this class, a quite difficult condition needs to be satisfied, as suggested by Bahramy et al. [5, 45]: they pointed out that in order to have a large Rashba splitting is required to have the same orbital character, meaning the same symmetry, for the states across the gap, mixed upon SOC (condition not easily met in usual ferroelectrics, e.g. oxides). At the same time, a compromise needs to be found for the bandgap, since a small bandgap increases the SOC, required for Giant Rashba splitting, while the semiconductivity requirement pushes into the other direction. As a reference, the father compound of this class, GeTe, presents $E_{gap} \sim 0.8$ eV [83].
The research for these materials is still ongoing and while a first group with possible members are binary or ternary IV-VI chalcogenides (e.g. the ones investigated in this work, SnTe, GeTe, BiTe and more [55]), other members could be found in known ferroelectrics materials with "heavy" elements (for high SOC) and small bandgap.
The study of the ternary alloy $Ge_xSn_{1-x}Te$ originates by this research, while also investigating the effects of the Ge doping on the SnTe crystal. The possibility of doping or inducing strain effects to these materials would allow to tune their structural and electronic properties for further improvements. The main application for these devices, so far, consists in energy efficient spin-to-charge conversion systems, easily implementable on Si-based devices, thus making this approach fully compatible with the universal CMOS technology.

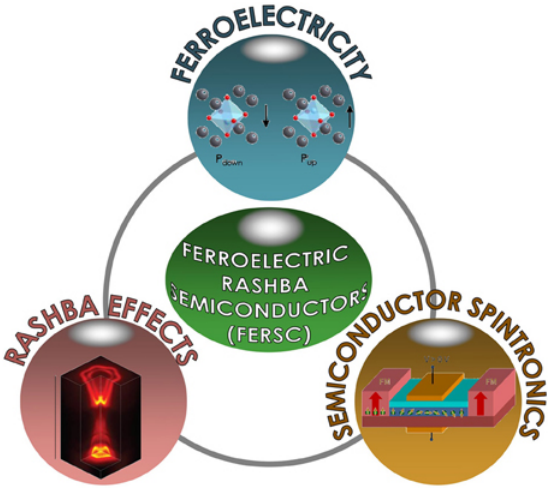

Figure 2.9: Schematic representation of the physical properties of ferroelectric Rashba semiconductors (FERSC), as reported in [77].

2.5. Case studies: GeTe and SnTe

Chalcogenides already find their application in every day life being widely employed as memory devices (e.g. in re-writable phase change optical memories [2]) and photovoltaic materials [87]. A notable compound is $Ge_2Sb_2Te_5$ (GST), used as a phase change material [71] in non-volatile resistive memory devices (PCRAMS) with large ON/OFF ratio thanks to great conductivity difference between the crystalline and amorphous phase (these two phases can be reversibly obtained by the application of specific current pulses) [50]. The new role of chalcogenides in spintronics arose only in the last decade, pushed by the research for new energy-efficient spin-charge conversion materials [25, 49, 77]. With the accent on this new focus, we'll present on one side the GeTe, showing a Giant Rashba splitting and being the father compound of the FERSC class of materials, while on the other side the SnTe, showing topologically protected surface states and being the father compound of the TCI class.

2.5.1. Germanium telluride

Germanium telluride is a prototypical crystalline ferroelectric, with two atoms in the primitive cell [54]. It undergoes a Peierls distortion at a Curie temperature T_c of 720 K, passing from a paraelectric cubic (β-GeTe, above T_c) to a reduced symmetry rhombohedral phase (R3m or α-GeTe, below T_c), as presented in figure 2.10b. α-GeTe is the stable structure at room temperature, which makes the characteristics of this phase more relevant for applications: a ferroelectric polarization of $\sim 60\mu C \cdot cm^{-2}$ results from the shift of Ge and Te atoms from the cubic positions along the [111] direction[58].
GeTe is also a narrow gap semiconductor with $E_{gap} \sim 0.8$ eV and a strong p-doping intrinsic character caused by Ge vacancies [15, 104], leading to a high density of hole carriers $p \approx 2 \times 10^{20}\,cm^{-3}$. The high conductivity of germanium telluride makes it similar to a polar metal and also introduces high robustness of the spontaneous polarization to external fields: the strong internal screening of the surface polarization charges generated by free carriers minimizes the effect of the depolarization field, thus leading to a high stability of the FE state. While making the FE state stable to external perturbation, this also makes more difficult the external control of the polarization through gate voltages. Nevertheless, it has been demonstrated that the applied electric field can sufficiently penetrate thin enough polar metals/semiconductors [29], and this is also the case for GeTe, as proved in [98] with gating experiments on micrometric structures.
This compound presents all the requirements for the Giant Rashba splitting:(i) lack of inversion symmetry, (ii) the valence band maximum (VBM) and the conduction band

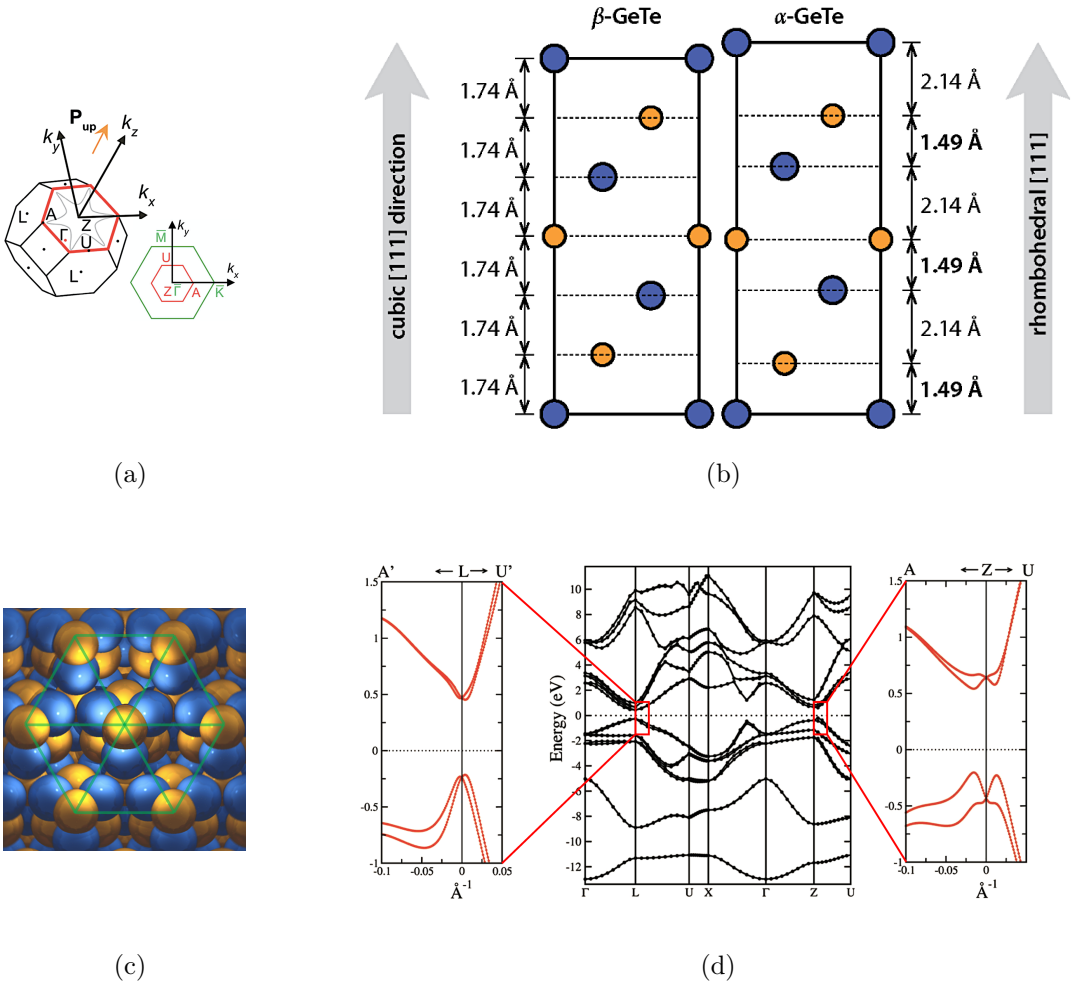

(a) (b)

(c) (d)

Figure 2.10: (a) First brillouin zone of bulk GeTe and, on the right lower corner its surface brillouin zone. (b) Structure of the two stable phases, α and β, of GeTe, showing the different position of the atoms within the unit cell. (c) DFT prediction of the surface of GeTe for a (111) oriented crystal, clarifying the origin of the hexagonal symmtry. (d) Bands diagram calculated by DFT, with the zoom on the right presenting the region of interest for the experiments conducted, ZA and ZU, and the one on the left presenting the band splitting along the LA' and LU', showing how the rhomboedral distortion breaks the equality between the brilluoin surfaces L and Z. Adapted from [57], [23] and [25].

minimum (CBM) that have the same symmetry character, (iii) large SOC and (iv) a narrow gap. So that it presents a large Rashba parameter ($\alpha_R \sim 5\,\text{eV}\,\text{Å}$) with respect to other materials (e.g. BiTeI has $\alpha_R \sim 3.8\,eV$ Å [5, 45]). Despite the Rashba effect being usually found on metallic surfaces and interfaces, a Rashba Hamiltonian can arise also in the bulk bands as a consequence of the structural distortion (along the [111] direction for the GeTe case), leading to a structural inversion asymmetry (SIA). A giant Rashba splitting is found both in valence and conduction bands around the Z point of the Brillouin zone, as shown in figure 2.10d, for the carriers with crystal momentum within the plane orthogonal to the ΓZ direction, with the hexagonal shape delimited by the ZU and ZA directions (see figure 2.10a as a reference for the reciprocal space directions).
The Rashba Hamiltonian in the bulk GeTe can be expressed as in equation (2.18), under the $\mathbf{k}\cdot\mathbf{p}$ framework, with k_x and k_y corresponding respectively to the ZA and ZU directions.

$$H_R = \alpha(\sigma_x k_y - \sigma_y k_x) + \lambda(k_+^3 + k_-^3)\sigma_z \tag{2.18}$$

with $k_\pm = k_x \pm ik_y$ and the Rashba parameter corrected for the case of bulk systems, $\alpha_k = \alpha_R(1 + ak^2)$, so that both the terms in the Hamiltonian present a cubic dependency on the wave-vector. This Hamiltonian leads to an asymmetric band splitting (ΔE_S) on the two axes ZA and ZU, such that it is maximum along the first and minimum along the second, as obtained by equation (2.19).

$$\Delta E_S = 2(\alpha_k^2 k^2 + 4\lambda^2 k^6 \cos 3\theta^2)^{\frac{1}{2}} \tag{2.19}$$

where θ stands for the angle between $\mathbf{k}$ and k_x (i.e. $\theta = 0$ along ZA and $\theta = 90°$ along ZU). The maximum energy splitting is $E_R \sim 250\,\text{meV}$, with $k_R \sim 0.1\,\text{Å}^{-1}$.
The fact of the Rashba splitting and ferroelectricity being both connected to the structural deformation of GeTe has a relevant importance, since it allows to switch both the polarization and spin texture of Rashba bands by inverting the distortion direction. As previously mentioned, this can be performed on thin films by voltage gating in order to obtain tunable Rashba spin-locked bands, extremely interesting for the spintronics playground.

2.5.2. Tin telluride

SnTe is another notable chalcogenide and it is mainly known for showing topological states. Its structure is quite similar to the one of GeTe, presenting a rhombohedral distortion at low temperature, giving rise to α-SnTe, while above this temperature it has a simple rocksalt structure. The schematics of the two structures are shown respectively in

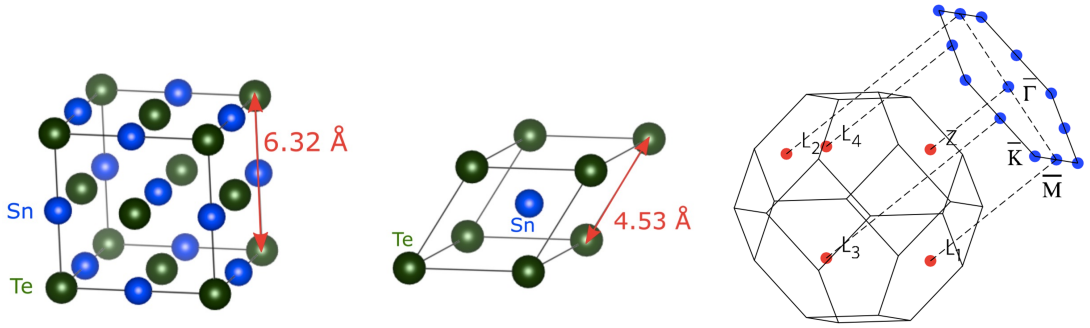

(a) (b) (c)

Figure 2.11: (a) Rocksalt-like, paraelectric β phase of SnTe. (b) Rhombohedral, ferroelectric α phase of SnTe. (c) First brillouin zone of bulk SnTe with the projections for the (111) surface.

figures 2.11a and 2.11b.

The Curie temperature for SnTe ($T_c \sim 100\,\mathrm{K}$) is much lower than for GeTe and, in particular, it also strongly depends on the carrier concentration: the growth of SnTe is affected by the same vacancy problem of GeTe and the amount of Sn vacancies determines both the p-doping character of the material and its Curie temperature (i.e. the Curie temperature decreases with the increase of the p-doping, which is proportional to the density of vacancies [44, 94]).

In the α phase, it is ferroelectric, with a predicted polarization $\sim 40\,\mu\mathrm{C\ cm}^{-2}$ along the [111] direction. In this phase, it also satisfies the conditions for a giant Rashba splitting, but the low temperature required by this phase is a problem for applications. In 2016, it has been proved that T_c could be raised up to $\sim 270\,K$ for the in-plane polarization of ultra-thin SnTe, down to 1-Unit Cell limit thickness [20]. Nevertheless, for the purpose of compatibility with GeTe, as for our studies, the interesting polarization is the out-of-plane one, for which the issue still holds.

In its simple cubic structure, see figure 2.11a, SnTe has been demonstrated to show topologically protected surface states in correspondence of the bulk band gap, as anticipated in section 2.3.2. This takes place at the four equivalent X points, along the $\Gamma - X$ direction, corresponding to the (001) surface states (and other equivalent planes). Accounting for the (111) surface plane, two Dirac cones are found along the $\bar{\Gamma}\bar{Z}$ axis, which are reported in figure 2.11c. Even in the presence of the distortion typical of the α phase, the symmetry along [111] axis is preserved and the topological surface states are still present.

The DFT work presented in [79] has shown how the distortion of the cubic structure in the intermediate region between the α and β phases can effectively modify the band dispersion of SnTe leading to the cohexistance of different states, from a $\mathbb{Z}_2$(TI)+FERSC, to TCI+FERSC, until the pure FERSC state at full rhombohedral distortion, as shown in figure 2.12. The λ parameter quantifies the rhombohedral distorsion along the [111]

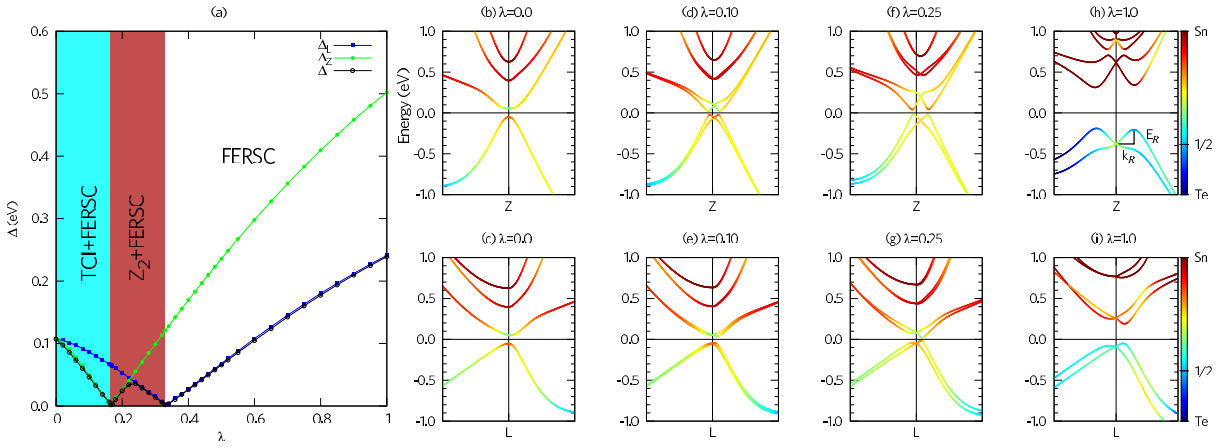

Figure 2.12: Ab initio DFT. (a) Topological phase diagram estimated from the evolution, as a function of λ, of the energy gaps around Z (Δ_Z) and L (Δ_L). The "minimal" energy gap (Δ) over the whole BZ is drawn in black. The band structures in proximity to Z point (along the directions $B \to Z \to P$) and L point (along the directions $\Gamma \to L \to B_1$), respectively, are shown in panels (b) and (c) for $\lambda = 0$, in panels (d) and (e) for $\lambda = 0.10$, in panels (f) and (g) for $\lambda = 0.25$, in panels (h) and (i) for $\lambda = 1$. The orbital character of bands is shown by color map going from dark blue (Te) to dark red (Sn), with $1/2$ corresponding to the equally mixed anionic and cationic character. For clarity, we report in panel (h) the graphical definition of the Rashba momentum offset, k_R , and of the Rashba energy splitting, E_R. Adapted from [79].

direction ($\lambda = 0$ for the β, $\lambda = 1$ for the α phase). Such bands show the possibility of having both TCI and Rashba properties at the same time, but also the general possibility of engineering the band structure of such a material.

Following these results, we here started investigating an alternative approach to SnTe band engineering: introducing a band modulation and a lattice distortion by mean of doping.

Considering the stable rhombohedral space group (R3m) of α-GeTe at room temperature, we investigated whether a germanium doping in the SnTe matrix (presenting a cubic phase Fm3m at room temperature) would induce a lattice distortion proportional to the amount of doping. This corresponds to the study of the ternary alloy $Ge_xSn_{1-x}Te$ with a variable contribution x of Ge atoms. At the two extremes of this alloy are the GeTe ($x = 1$) and SnTe ($x = 0$). The engineering of the alloy band structure has been performed in this thesis work and presented in chapter 4 together with DFT calculations supporting the results.

3 | Experimental Methods

3.1. LASSE

Most of the growth and characterization activities of this work have been carried out at Polifab, a facility of PoliMi for micro and nanotechnologies fabrication. Here, the principal instrument that has been bused is LASSE (LAyered Structures for Spin Electronics). LASSE is a multi-chamber system, working in high vaccum (HV) and ultra-high vacuum (UHV) conditions [8], dedicated to growth and characterization of films and heterostructures for spin electronics. Different materials can be used for this purpose, from metals to semiconductors and oxides (ferro-, ferri- and antiferro-magnetics, ferro-electrics, half metallic).
In order to improve samples' quality and reduce contamination, the system is kept in UHV and HV (ranging from 10^{-10} $mBar$ to 10^{-7} mBar) thanks to independent vacuum pumps in every chamber: rotary, turbomolecular, non-evaporable getter (NEG) and ion pumps.
LASSE is composed by five chambers (figure 3.1): the Introduction Chamber (IC), the Pulsed Laser Deposition Chamber (PLDC), the Sample Preparation Chamber (SPC), the Measurement Chamber and the Photocathode Preparation Chamber (PPC).
In order to preserve the UHV condition in the chambers, all separated by vacuum valves and independently pumped, a first Introduction Chamber (IC) is used to interface the vacuum system with the ambient at atmospheric pressure: a N_2 flux is used to vent the system in order to avoid contamination, while a first step of rotative pump (down to $\sim 10^{-3}$ mBar) and a second of turbomolecular pump are used to quickly restore the HV conditions (down to 10^{-8} mBar). From IC, the sample can be moved, by magnetic arms, to the two preparation chambers, SPC and PLDC.
SPC is dedicated to sample preparation (annealing and sputtering processes) and growth of heterostrustures by Molecular Beam Epitaxy (MBE), performed in ultra-high vacuum conditions (pressure lower than 10^{-9} mBar). The preparation of samples consists of an ion beam sputtering process, using argon ions accelerated towards the sample surface by a high voltage (1.5 kV), and/or an annealing process that can be used both for re-

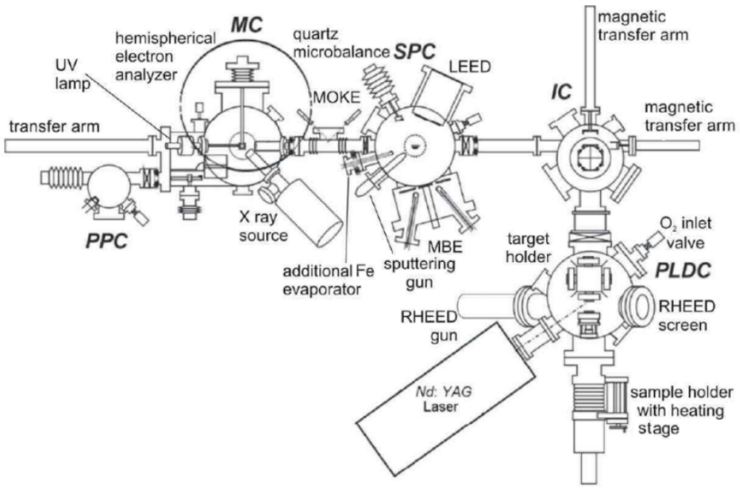

Figure 3.1: Schematic representation of LASSE (LAyered Structures for Spin Electronics) multi-chamber system.

ordering/crystallization of disordered structures (e.g. after sputtering cleaning) or for thermal de-capping of samples (e.g. in the case of capping more volatile than the structure beneath). Moreover, a Low Energy Electron Diffraction (LEED) tool is also available and can be used to promptly investigate the surface crystallinity.

The PLDC, on the other side of IC, is dedicated to the Pulsed Laser Deposition (PLD) growth technique in which a high energy pulsed laser beam (Nd-YAG) impinges on a target, which vaporizes creating a high energy plasma of material that is deposited on the sample. Reflection High Energy Electron Diffraction (RHEED) is present in this chamber to either monitor the epitaxial growth quality or to investigate surface order, in a similar way to LEED, in finished films.

From the SPC, the sample can be moved to the MC, entirely dedicated to measurements of stoichiometry, structure and electronic properties. Here, many measurement techniques are available, comprehending electron spectroscopies and diffraction techniques[1]: X-ray and ultraviolet photoemission (XPS, UPS), spin-polarized inverse photoemission (SPIPE), x-ray photoelectron diffraction (XPD).

The fifth chamber is the PPC, dedicated to the preparation of the GaAs photocathodes used to generate the electron beam employed in Inverse Photoemission Spectroscopy (IPES) and Adsorbed Current Spectroscopy (ACS) (details in section 3.6). Being this beam characterized by a spin polarization, up to 25%, it is possible to exploit it for spin sensitive experimental techniques: spin dependent ACS (as in [10]) of magnetic materials and membranes, spin dependent IPES [21] or novel experiments of spin-to-charge currents conversion (e.g. Inverse Spin Hall Effect, ISHE) performed directly on samples grown in UHV, without the need of capping layers. This new experimental technique related to

[1]both the mentioned techniques will be described in the following sections

spintronic reveals a new approach to this kind of experiments, usually performed after capping and contacts deposition (e.g. four probes measurements), but requires some improvement of electron gun's performances, which will be discussed in chapter 5, and the addition of controllable contacts within the vacuum environment, not discussed in this work.

3.2. MBE

Molecular Beam Epitaxy (MBE) is an epitaxial deposition technique carried out in Ultra High Vacuum (UHV) conditions that allows the growth of high quality epitaxial heterostructures of metals, semiconductors and insulators. The MBE (figure 3.2) is a Physical Vapor Deposition Technique (PVD), in which the deposited material goes from a vapor phase to the condensed one, while no chemical reaction occur in the gaseous phase of materials to be deposited, differently respect to Chemical Vapor Deposition (CVD). It is possible to define three main physical processes taking place during deposition, each one of them confined by its spatial region(as shown in figure 3.2):

- Molecular beam generation, in which the material we want to deposit is heated up to its evaporation or sublimation point, depending if the source is in liquid or solid state;
- Propagation of the molecular beam towards the sample's surface;
- Crystallization process, in which the depositant beam reaches the substrate surface and interacts with it.

Molecular/atomic beam generation

In the MBE present in LASSE, Knudsen cylindrical cells (figure 3.3) are heated by electron bombardment guarantying small and controlled deposition rates, necessary for the quality of epitaxial growth.
Effusion, within the evaporation phenomena, is described by a dynamic balance of emission and recondensation that is studied in the kinetic theory of gasses and synthetized in the expression of the mass effusion rate, known as Hertz-Knudsen equation[2]:

$$\frac{dN_e}{Adt} = a_v(p_{eq} - p)\sqrt{\frac{N_a}{2\pi M K_B T}} \qquad [m^{-2}s^{-1}] \tag{3.1}$$

[2]Eq. 2.2 in ref [38]

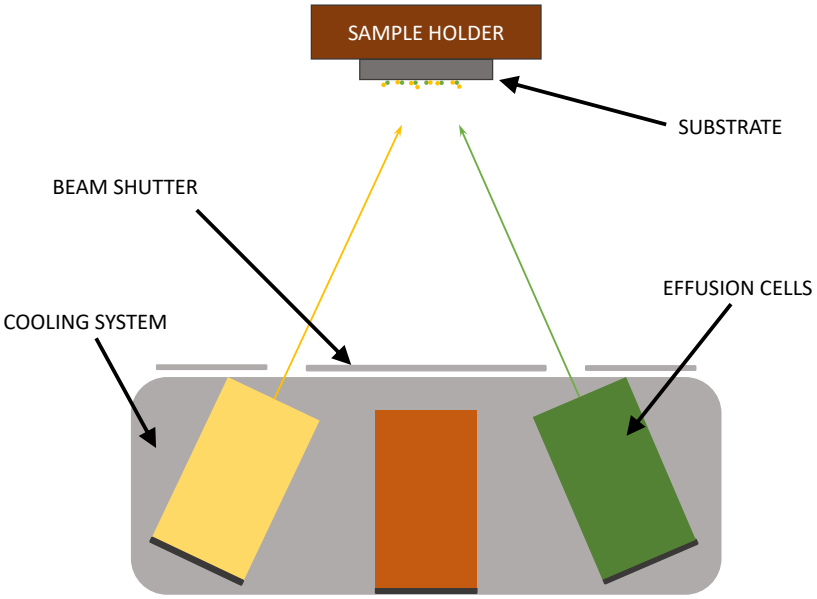

Figure 3.2: Schematic representation of an Molecular Beam Epitaxy setup.

where p_{eq} is is the equilibrium pressure at the surface of the material, p the pressure of the environment and a_v is a parameter empirically introduced by Knudsen, such that it represents the re-deposited fraction $(1-a_v)$. M is the molecular weight of the evaporating species, T the evaporating temperature and k_B and N_a are the Boltzmann and Avogadro constants, respectively.

Given this equation, we can define a first evaporation mode, described by Langmuir [3] as evaporation from free surface. This mode makes use of low environment pressure and material in a boat-like container in order to reach high evaporation rates: due to low pressure, the vapor phase is considered in equilibrium with the material's surface and no re-condensation takes place ($a_v = 1$, $p \simeq 0$). This techniques usually presents higher evaporation rates, with broad angular distribution.

A second evaporation mode, known as Knudsen technique, can be used: it is different from the previous one due to the use of an isothermal enclosure with a small aperture from which the material is evaporated. Within this container, which is called crucible, the equilibrium pressure is maintained and the aperture works as an evaporating surface with $a_v = 1$ (since no actual surface is present there for re-condensation to take place). This crucible shape limits the angular distribution of the emitted material and improves the stability and tunability of the temperature-controlled effusion rate given by the isothermal enclosure. In order to have low deposition rates (1 nm/s), this second evaporation mode

[3] Eq. 2.18 in ref [38]

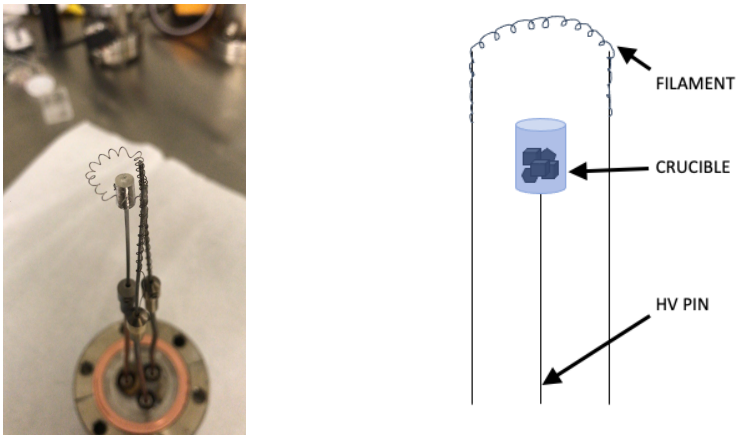

(a) (b)

Figure 3.3: Image of an effusion cell, with the comparison between the schematic of it (b) and a real one (a), namely the Co effusion cell used in LASSE, for which a rod of material is used. The filament is used to produce electrons that are accelerated towards the crucible set at high voltage.

is preferred.

In the used setup (figure 3.3), a current of few amperes flows into a tungsten filament, which emits electrons by thermo-emission. This cloud of electrons is then accelerated onto the cylindric crucible thanks to the high voltage set to it. The power of electron bombardment can be controlled either through the current applied to the filament or the high voltage (few kV) applied to the crucible. The electron bombardment heating, compared to a conventional resistive heater (a filament twisted around the outer walls of the crucible), shows better time response of the evaporant to the heating source and lower heating of the outer walls of the cell. Heating by irradiation and thermo-emission from the filament is also present and can be enough to evaporate highly volatile material like Tellurium without needing the high voltage.

Crucibles are used for materials that are liquid at the used vapor pressure (e.g. Au, Ag, Sn) or solids in the form of powder/fragments (Te, Ge) or insulating materials (such as MgO). For conductive materials that evaporate trough sublimation, it's possible to use directly a metallic rod (such as for Fe, Pt, Co).

Beam propagation and UHV condition

After the effusion, the beam propagates, through a hole in a shutter that limits its spatial broadening, until the substrate mounted on a xyz vacuum manipulator. The cell-to-substrate length is usually $\sim 20\,\text{cm}$, therefore it's requested that the beam can propagate this length without interactions. In order to have this condition satisfied, it's important to

consider the inelastic mean free path of the used atomic species at the chamber's pressure. This can be taken as the reference maximum distance for atoms to be crossed without scattering events and it is expressed by [67]:

$$L = \frac{1}{\sqrt{2}\pi n p^2} \quad \text{, with} \quad n = \frac{p}{k_B T} \tag{3.2}$$

Where p is the chamber pressure, k_B the Boltzmann constant and d the molecule/atom diameter. Therefore, a good estimate for it is:

$$L = 3.11 \cdot 10^{-24} \cdot \frac{T}{p d^2} \tag{3.3}$$

This approximated calculation only accounts for a single particle propagating in the environment, while a more precise model, also accounting for the density of particles emitted, allows to compute more precisely the maximum residual gas pressure or, equivalently, the mean free path of beam's particles (L_b) required in order to neglect scattering events:

$$L_b^{-1} = \sqrt{2}\pi n_b d_b^2 + \pi n_g d_{bg}^2 \sqrt{1 + {}^{v_g^2}/_{v_b^2}} \quad \text{, with} \quad d_{bg} = \frac{1}{2}(d_b + d_g) \tag{3.4}$$

Where n_b, d_b and v_b are concentration, diameter and average velocity of the beam's molecules, while the subscript g refers to the residual gas in the chamber.
Using this formula with standard parameters such as (1) room temperature ($T_a = 300\,K$), (2) a typical semiconductor as Ga ($d_b = 2.7 \cdot 10^{-10}\ m$), (3) a flux rate of roughly $n_b = 2.6 \cdot 10^{16}\ m^{-3}$, (4) $L_b = 0.2\ m$, a N_2 environments and considering the formula for p in equation (3.2) we get $p_g(max) = 7 \cdot 10^{-2}\ Pa$ equivalent to roughly $5 \cdot 10^{-4}\ Torr$. From this, it is evident that scattering events are not a problem in the LASSE's SPC conditions ($10^{-10}\ Torr$) and can be neglected for both a single beam and two materials in co-evaporation.
There's another reason for which UHV is required, which is to avoid surface contamination: the sample's surface is exposed to the residual gas in the chamber and therefore some of it will deposit on it, until the formation of a monolayer of gas adatoms/contaminants. In order to maintain the required purity during growth, the time needed to form a monolayer of contaminants t_c must be much smaller than the one to deposit a monolayer by evaporation t_{ev} (both considered for unit area):

$$t_{ev} \ll t_c \tag{3.5}$$

These parameters can be estimated by the rate of particles striking on the unit surface for second. $t_e v$ is inversely proportional to the evaporation rate set at the Knudsen cell, whose standard values are $10^{19}\ m^{-2}s^{-1}$ for growth rate of $1\mu m/h$ in the case of Ga, which is close to the case of study. For t_c, we need to consider the molecules randomly striking on sample's surface following the kinetic theory of gasses, so that:

$$w = p_i \sqrt{\frac{N_a}{2\pi k_B M_i T}} \tag{3.6}$$

where p_i is the partial pressure of the considered contaminant (let's say N_2 molecules), N_a is the Avogadro number and M_i the molecular weight. For the nitrogen molecule at room temperature, we get $w_i = 5.74 \cdot 10^{22} \cdot p_i$, so that it's possible to see how controllable this is through pressure.
With $p_i = 10^{-7}\ Pa$ ($\sim 10^{-9}\ Torr$) we get approximately $t_c = 10^4\ t_{ev}$. Furthermore, we should consider the sticking coefficient of residual gasses (i.e., the probability of an atom/molecule to stick on a surface after hitting it, usually $\ll 1$), strongly playing in favor of low contamination rates.
All in all, the vacuum condition of the used instrumentation is satisfying the requirements for extremely high purity of the grown samples, as it has been also verified with spectroscopy techniques (XPS).

Deposition and crystallization processes

As said in previous paragraphs, the rate of atoms/molecules impinging on the substrate's surface is determined by the power used to heat the crucible and by geometry factors, while it's not affected by propagation through UHV.
In order to give an estimate of this rate, a quartz crystal microbalance can be positioned in the deposition situ: this device employs a gold plated piezo crystal which oscillates with its natural frequency, which is changing with the amount of material (mass) sticking on its surface and that can be detected, up to a single layer precision, through the Sauerbrey equation [86]:

$$\frac{\Delta f^*}{f_f} = -\frac{2f}{Z_q} m \tag{3.7}$$

with Δf the change in frequency, f_f the fundamental harmonic, Z_q a parameter characteristic of the crystal used and m the deposited mass. Developing the equation under the approximation of solid thin films deposited, causing only a small change in frequency

(e.g. $< 5\%$), we can get the following estimate for the aerial density difference $\Delta\Sigma$[4]:

$$\Delta\Sigma = \frac{\Delta M}{Area} = -C\frac{\Delta f}{n} \quad \text{, with} \quad C = \frac{v_q \rho_q}{2 f_0^2}. \tag{3.8}$$

where n is the number of harmonic frequency considered ($f_n = n \cdot f_0$) and C the sensitivity constant dependent on crystal properties.
Given the $\Delta\Sigma$ it's possible to estimate the deposited thickness (t), by knowing the sticking coefficient (S) the material's density (ρ), with the formula:

$$t = \frac{\Delta\Sigma \cdot S}{\rho} \tag{3.9}$$

where parameters S and ρ are tabulated for the different materials.
The growth of material on the substrate is a process that takes place far from equilibrium, governed by the kinetics of the surface mechanisms occurring when the impinging beams react with the outermost atomic layers of the substrate.
During deposition, four main phenomena take place (presented in figure 3.4a): (i) adsorbtion of atoms(molecules) impinging on the substrate, (ii) surface migration and dissociation of deposited molecules, (iii) incorporation into the crystal lattice and (iv) thermal desorption of not incorpored species.

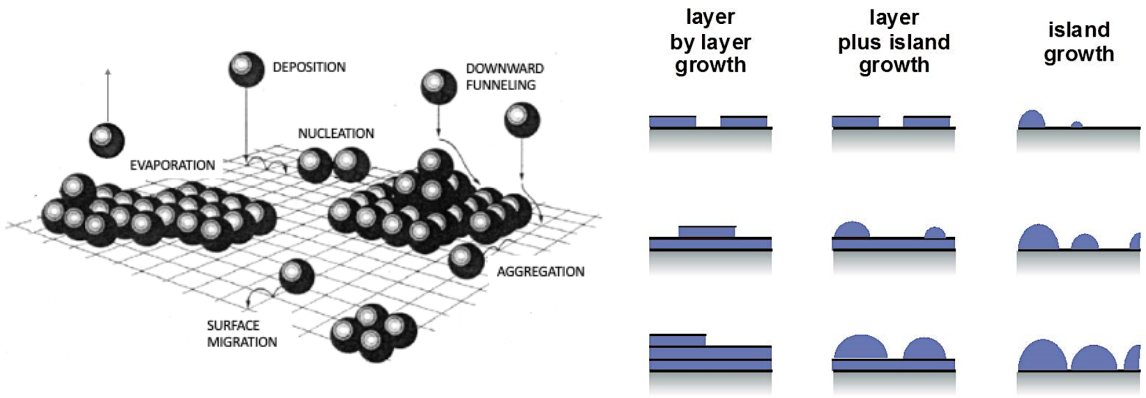

(a) (b)

Figure 3.4: (a) Interplay of kinematic processes taking place during epitaxial growth, while (b) reports the possible growth modes that can be achieved.

The adsorption process is composed by a first step of physical adsorption (weak bonding) and a second of chemical adsorption in which the adsorbate is incorporated in the crystal lattice. Depending on the dynamic of this process, partially controllable with working

[4]expressed in SI units of $kg \cdot m^{-2}$

temperature and evaporation rates, different modes of growth can be achieved, resulting in three distinct surface morfologies (figure 3.4b):

- Layer-by-layer (Frank-Van der Merwe): growth through sequential monolayer formation leading to the most homogeneous samples,
- Island-nucleation (Volmer-Weber): tridimensional clusters are formed on the substrate during growth due to low mobility of adatoms or low wettability[5] of the substrate, resulting in irregular surface.
- Layer-plus-island (Stranski-Kranstanov): after few uniform monolayers formation, clusters start to form. This effect is induced by mismatch strains and by the change of surface energy while the substrate layer seen by adatoms is modified.

The first mode of growth is required in order to obtain high quality crystalline samples; increasing the sample's working temperature can favour this type of growth enhancing the surface mobility of ad-species. The temperature increase also allows for the sample's structure reconfiguration in its most stable phase (the crystalline one), as seen for the case of SnTe deposition ($T \sim 200$°C allows for crystalline growth while the amorphous phase is obtain from deposition at ambient temperature). In order to avoid strain effects that would lead to the Stranski-Kranstanov growth, the choice of the substrate is fundamental: the mismatch between the lattice parameters of the substrate and grown layers should be minimized in order to reduce strain effects and favour the single crystal growth.
In the case of multiple materials co-deposition, it must be considered how the different evaporation temperatures affect the growth, since the single growth rate is not the same of the multi-component one. This could lead to non-stoichiometric samples and therefore the combined growth rate have to be double checked by XPS stoichiometry analysis in order to correctly calibrate the single effusion cells temperatures. This could be the case of GeTe growth, for which the higher evaporation temperature of Ge with respect to Te leads to a Ge vacancy during crystal growth (higher temperature leads to higher mobility and thus to higher probability for desorption). In order to compensate this effect, an increase of Ge effusion rate is required.

[5]The wettability of a material, sometimes also related to the wettability potential [6], can be related to the difference in bond strengths, that leads to the difference in surface energies between the two species.

3.3. LEED

Elastic scattering/diffraction of electrons is a common technique used for obtaining structural information about surfaces.
Low Energy Electron Diffraction (LEED) is based on the collection of low-energy electrons scattered by the Bragg planes at the surface of a single-crystal [75]. The experimental setup for LEED consists of an electron gun producing a primary electron beam and a system aimed for the observation of the Bragg diffraction spots.
The electron beam is produced by thermionic emission from a filament within the Wehnelt cylinder[6] and then accelerated and focused with electrostatic lenses.
Electrons back-scattered from the sample hit the fluorescent screen, aimed to the visualization of the diffraction pattern, after being filtered by three retarding grids (necessary to remove spurious signals coming from inelastically scattered electrons).
The high degree of surface sensitivity comes from the choice of electrons' energies (typically 20 - 500 eV), giving a De Broglie wavelength comparable with the lattice parameter (~ 1 Å) and so a large elastic back-scattering cross-section of the atoms in the sample:

$$\lambda[\text{Å}] = \sqrt{\frac{150.41}{E[eV]}} \tag{3.10}$$

Furthermore, we also have the minimum inelastic mean free path of electrons in the region 30 - 300 eV, guarantying high surface interaction [7].

The requirements for constructive interference at the fluorescence screen are given by the Von Laue condition [4] for constructive interference:

$$e^{i(\mathbf{k}_{out}-\mathbf{k}_{in})\cdot\mathbf{R}} = 1 \tag{3.11}$$

giving as a result energy conservation, demanding that the modulus of the incident wave vector, $\mathbf{k}_{in}$, equals that of the outgoing one, $\mathbf{k}_{out}$, and that the components of these wave vectors parallel to the surface satisfy the equation:

$$\mathbf{k}_{\parallel out} = \mathbf{k}_{\parallel in} + \mathbf{g}_{hk} \ , \tag{3.12}$$

where the reciprocal lattice vector is:

$$\mathbf{g}_{hk} = h\,\mathbf{b}_1 + k\,\mathbf{b}_2 \tag{3.13}$$

[6] cylindrical electrode used for control and focusing of an electron beam in thermionic devices [113].
[7] for this range of energies $\lambda_{IMFP} \simeq 1$ Å.

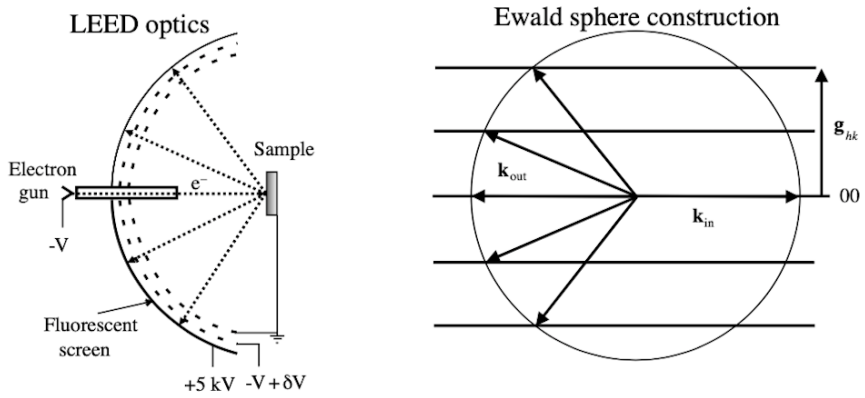

(a) (b)

Figure 3.5: (a) LEED experimental setup and (b) Ewald sphere for elastic back-scattering on a two-dimensional surface. Adapted from [106].

with $\mathbf{b}_1$ and $\mathbf{b}_2$ primitive translation vectors of the reciprocal lattice:

$$\begin{aligned} \mathbf{b}_1 &= 2\pi \mathbf{a}_2 \wedge \mathbf{n}/A \\ \mathbf{b}_2 &= 2\pi \mathbf{a}_1 \wedge \mathbf{n}/A \end{aligned} \quad \text{with} \quad A = \mathbf{a}_1 \wedge \mathbf{a}_2 \cdot \mathbf{n} \tag{3.14}$$

where $\mathbf{n}$ is the vector normal to the considered surface.

The diffraction requirements are conveniently represented using a simplified version of the Ewald sphere used for three-dimensional periodic systems as shown in figure 3.5in which we use rods on the out-of-plane direction (being the conservation of the $\mathbf{k}_\perp$ not required). The main drawback of this technique is that it requires UHV conditions in order to reduce undesired scattering events and hence requires to be employed in vacuum apparatus. The common use of it is to characterize surfaces during growth and preparation processes.

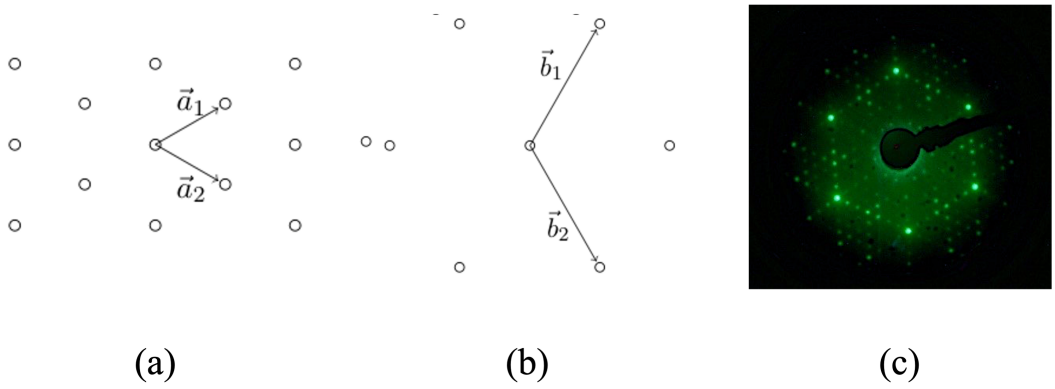

Figure 3.6: (a) Example of an hexagonal two-dimensional lattice and (b) its reciprocal. (c) LEED pattern of a Si(111) presenting a 7×7 surface reconstruction.

3.4. Photoemission spectroscopy

Photoemission spectroscopy is an extremely versatile measurement technique that makes use of photoelectric emission in order to investigate the binding energies of the atoms constituting a material. This can be done for chemical characterization purposes as well as for structure investigation and energy bands analysis.

A monochromatic soft X-rays beam is focused on the sample to excite a region of it (pho-

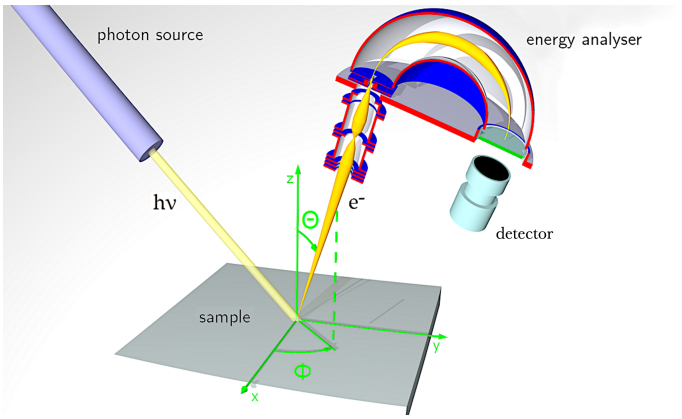

Figure 3.7: Scheme of a photoemission spectroscopy (PES) setup.

ton energies ranging from 8 to $\sim 1490\,\text{eV}$). As a consequence of energy conservation, some electrons are emitted with kinetic energy E_k by the sample according to the photoelectric effect equation:

$$E_k = h\nu - E_b - \Phi \tag{3.15}$$

where $h\nu$ is the photon energy, Φ the work function of the investigated material and E_b the binding energy of the electron involved (see also figure 3.8a). The requirement in order to have emission of an electron from a bond level is $h\nu > E_b + \Phi$.

The emitted electrons can propagate inside the material, before undergoing unelastic events (phonon excitations, plasmon excitations or interband transitions), for a distance comparable to the Inelastic Mean Free Path (λ_{IMFP}), defined as the mean distance between to consecutive scattering events, that can be computed with the universal formula:

$$\lambda_{IMFP}[\text{Å}] = \frac{1430}{E_k^2[eV]} + c \cdot \sqrt{E_k[eV]} \tag{3.16}$$

where $c = 0.54$ for metals and 0.72 for insulators.

According to the Lambert-Beer law, the contribution of emitted electrons intensity from the depth z of a sample is:

$$I(z) = I_0 \cdot e^{-\frac{z}{\lambda_{IMFP}}} \tag{3.17}$$

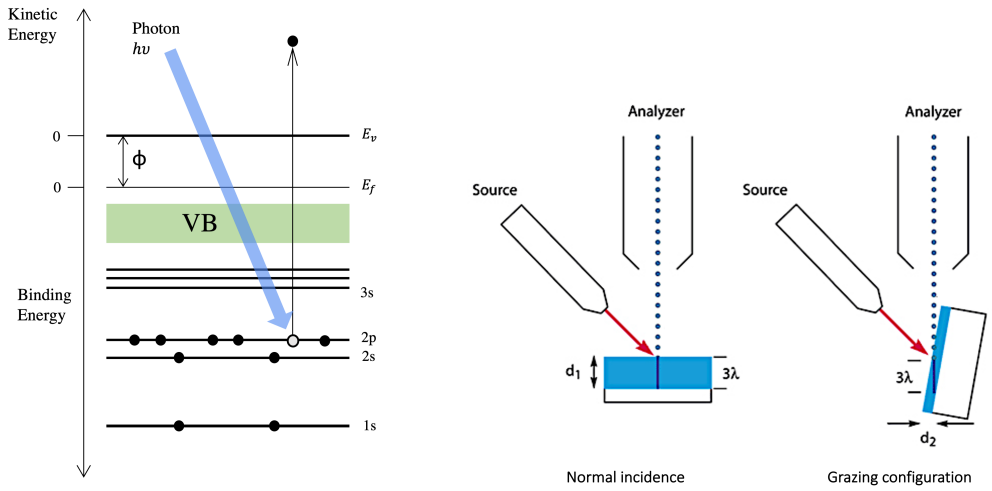

(a) (b)

Figure 3.8: (a) Represents the photoelectric effect while (b) shows how the escape depth changes respect to the collection angle θ.

resulting in a negligible intensity for $z > 3\ \lambda_{IMFP}$. As a result, a good estimate for the surface sensitivity of this investigation technique is the λ_{IMFP}, varying from few Å to few nanometers.

In order to increase, when required, the surface sensitivity, it is possible to increase the collection angle θ of the analyser with respect to the sample's surface normal. For $0 < \theta < \pi/2$, the escape depth can be defined as:

$$d_{ED} = \lambda_{IMFP} \cos\theta \tag{3.18}$$

as reported in figure 3.8b.

Once the electrons are emitted from the sample, they can be acquired by an hemispherical electron energy analyzer, shown in figure 3.7, consisting in a first section of electrostatic lenses to slow down electrons to the pass energy E_p, two hemispherical electrodes (in order to only select electrons with the pass energy E_p) and an electron detector (e.g. a channeltron detector) [60]. The emitted electrons intensity can be resolved[8] in energy by changing the pass energy of the hemispherical detector. By considering how the electrons disperse in the orthogonal direction to the analyzer axis, e.g. along x in figure 3.7, and using a position sensitive detector (e.g. a micro-channel plate), it is possible to resolve the emission angle. This allows for the analysis of bands dispersion in the reciprocal space, as in Angle Resolved PES (see section 3.4.3).

[8]The term *resolution* is often used in spectroscopy experiments to express the capability of distinguish different quantities, e.g. energy, momentum or spin of the detected electrons.

3.4.1. XPS

In X-ray Photoelectron Spectroscopy (XPS) high photon energies are employed to analyse core-level electrons, to study the surface chemical composition and the electronic states of a material. In the LASSE setup, the X-ray tube allows to choose between an $Al - K\alpha$ source, corresponding to a photon energies of 1486.6 eV, or an $Mg - K\alpha$ source with energy of 1253.6 eV. Both of them presents satellite peaks that has to be accounted for when evaluating the spectra[9].
The result of a measurement is a spectrum of electron counts vs kinetic energy in which core-levels peaks are superimposed to the background of secondary electrons. CasaXPS software has been used for spectrum analysis, allowing to subtract the background signal (Shirley or linear profile have been used in this work) and fit the peaks with their components.

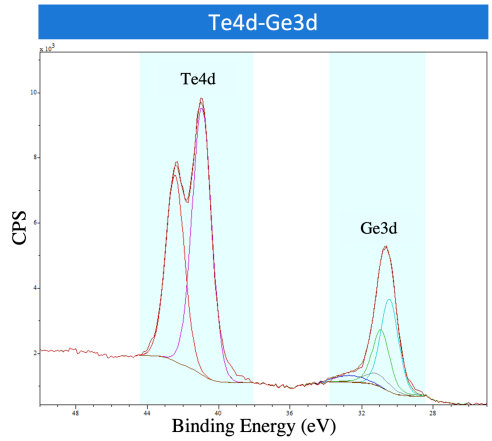

Figure 3.9: Example of Casa-XPS software spectrum analysis reporting Te and Ge peaks used for stoichiometry and the components used during fitting. The figure also reports an example of Shirley background subtraction [100]-

.

Since every peak detected in the spectra is related to a core-level of an atomic species, eventually presenting shift and deformations related to chemical and structural effects, a qualitative analysis of intensity peaks allows, for example, to detect the presence of contaminants in the sample (C residuals after exposure to environment or oxidation of the surface). A quantitative comparison, on the other hand, allows for thickness calculation (considering peaks attenuation through an overlayer) and stoichiometry computations.

[9] A satellite peak is a non negligible second emission line typical of an X-ray lamp, usually with intensity of a few percentage ($\sim 3 - 10\%$) of the main peak, positioned within some dozens from it.

The intensity of a peak can be expressed as:

$$I_i \propto C_i \Phi \sigma_i \lambda_i T_i \tag{3.19}$$

where C_i indicates the concentration of the atomic species i, Φ the photon flux, σ_i the photo-emission cross section, λ_i is the inelastic mean free path of the photo-emitted electrons and T_i is the transmission of hemispherical analyzer.
In actual stoichiometry computation, Φ is constant within a single measure, while when comparing different acquisitions it can be accounted for by normalizing all the spectra to a reference intensity peak (e.g. a Ta 4f peak is used at LASSE, since a tantalium foil is present on the sample manipulator for this purpose, but other stable metals as Au could also be exploited). Both the λ_{IMFP} and T are functions of the electron's kinetic energy E_k. For the common case of $E_{k,i} \gg 100eV$[10], it is possible to approximate $\lambda_{IMFP} \propto \sqrt{E_k}$ and, being $T \propto \frac{1}{\sqrt{E_k}}$ for hemispherical analysers, it results $\lambda_{IMFP} T = \text{const}$. The σ is tabulated as it both depends on the specific core level and on the used photon energy.

3.4.2. XPD

X-Ray Photoelectron Diffraction (XPD) is a diffraction technique employed to probe the structural order of thin films. It typically works in the same energy range of XPS, analysing the diffraction pattern of photoelectrons at a specific energy, associated to a core level of a given atomic species. The main difference with respect to other diffraction techniques is the ability of XPD to be chemically selective, allowing to analyse lattice positions of single atomic species of the compound.

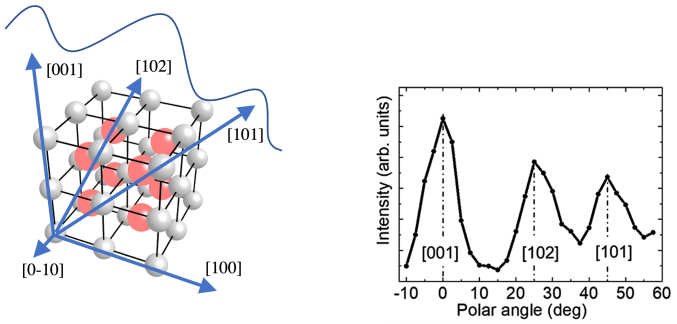

Figure 3.10: (a) Scheme of the forward scattering effect, giving highest intensity along the preferential crystallographic axis. (b) Example of intensity modulation versus the collection angle θ for a simple cubic structure.

[10] for all the considered i peaks

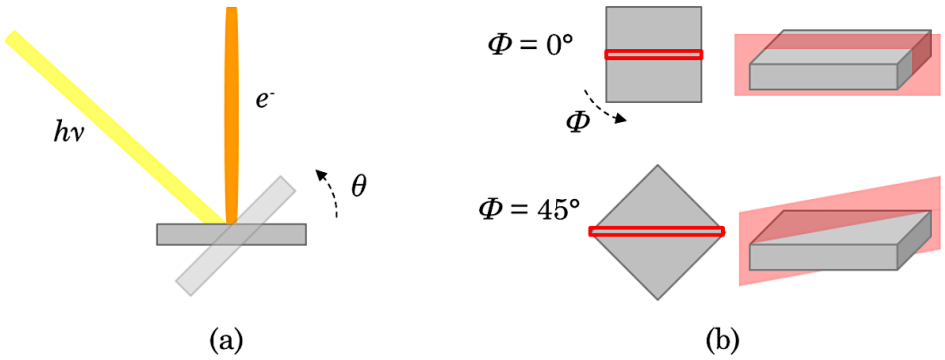

Figure 3.11: (a) Scheme of the typical XPD experiment, with variation of the θ angle, while (b) shows the different diffraction direction considered when tilting the angle ϕ.

In order to understand this technique is necessary to consider every atom in the excitation volume as a scattering centre and electrons in their wave representation: depending on the direction considered by the detector there will be constructive or destructive interference of emitted electrons according to the lattice principal directions, as shown in figure 3.10a. For high energy electrons, e.g. above 500 eV, the scattering amplitude is mainly in the forward direction, leading to the so called "forward focusing", in which the intensity of electrons increases along the particular directions in which there are more scattering centers. Thanks to this interpretation, the increase in the detected intensity is associated to a preferential axis (low Miller indexes axes) of the lattice.
By tilting the sample along the angle θ (collection angle shown in figure 3.11a), is therefore possible to see this effect and retrieve the diffraction pattern. By changing the angle ϕ, corresponding to a rotation in the surface plane of the sample investigated(see figure 3.11b), it is possible to perform diffraction along different crystallographic directions (important in the case of two different main symmetry axes as in the case of GeTe, where it necessary to distinguish between the ZA and ZU directions of reciprocal space).

3.4.3. ARPES and S-ARPES

Angle Resolved Photoemission (ARPES) is a leading surface sensitive technique that enables to measure simultaneously both angle of emission (which, in oriented single crystals, is related to the photoemitted electron momentum $\mathbf{k}$) and kinetic energy of electrons, giving access to the band structure near the Fermi surface of solid materials.
This technique has been exploited during beamtime at Synchrotron Elettra in Trieste, in collaboration with the staff of Advanced Photoelectric Effect (APE) beamline. The purpose of the collaboration has been to investigate the band dispersion and the spin maps of the ternary alloy GeSnTe grown at Polifab.

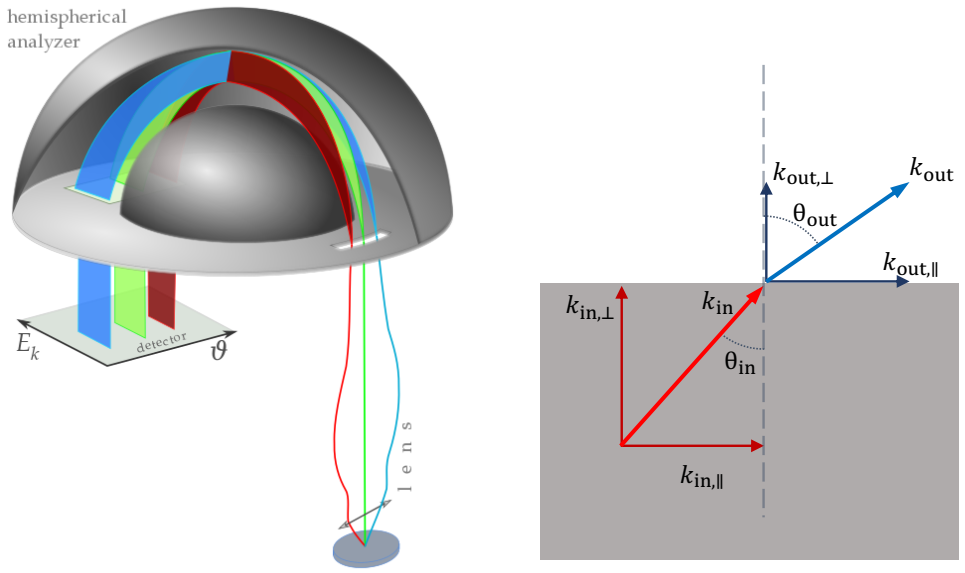

(a) (b)

Figure 3.12: (a) Scheme of ARPES: the difference with respect to traditional PES is the spatial dispersion versus the $\mathbf{k}_{\parallel}$ component. (b) Schematic representation of momentum conservation of electrons escaping into vacuum.

When a photoelectron is created inside the sample, due to momentum conservation:

$$\mathbf{k}_{in} = \mathbf{k}_{bound} - \mathbf{k}_{h\nu} \tag{3.20}$$

where $\mathbf{k}_{bound}$ is the momentum of the electron in the bound state, $\mathbf{k}_{in}$ the one of the excited electron within the material [76].

The beam used at the APE Low Energy endstation (APE-LE) has energy in the range 8-100 eV, i.e. the photon momentum is much smaller than the momentum of one electron in the valence band of the material ($\mathbf{k}_{h\nu} = \frac{2\pi}{\lambda_{h\nu}} \sim 2\pi\, 10^8 m^{-1}$, small with respect to $\mathbf{k}_i = \frac{2\pi}{a} \sim 2\pi\, 10^{10}\, m^{-1}$): it is then possible to consider only transitions in which electron's momentum is conserved (direct transitions) inside the solid $\mathbf{k}_{in} = \mathbf{k}_i = \mathbf{k}$.

An excited electron within the material, with energy $E_k = h\nu - E_b - \Phi$, has to overcome the step barrier given by the inner potential V_0, originated by the symmetry breaking along the normal to the surface [11], at the interface with vacuum. This surface barrier truncates the periodicity of the crystal potential along the direction normal to the surface (z), hence, only the component of the wave-vector parallel to the surface is conserved ($\mathbf{k}_{\parallel}$).

Considering the electron's wave vectors and crystal momentum as presented in figure 3.12b, with energy $E_k = \hbar^2(k_{\parallel} + k_{\perp})^2/2m$ and spatial dispersion along the k_x component (equiv-

[11] The inner potential V_0 can be inferred experimentally observing the periodicity of the dispersion $E(k_{\perp})$ doing experiment at $\theta = 0$ and varying the photon energy $h\nu$.

alent to probing at $\phi = 90°$), one obtains [76]:

$$k_{\parallel,in} = k_{\parallel,out} = \sin\theta_{out}\ k_x\sqrt{\frac{2mE_k^2}{\hbar}} \simeq 0.5\sqrt{E_k[eV]}\sin\theta_{out}\ \ \text{Å}^{-1} \tag{3.21}$$

while for the component normal to the surface:

$$k_{\perp,in} = \frac{1}{\hbar}\sqrt{2m_e(E_k\cos^2\theta_{out} + V_0)} \simeq \frac{1}{\hbar}\sqrt{2m_e(E_k + V_0)} \tag{3.22}$$

being the detected θ_{out} really small and so $\cos\theta_{out}^2 \sim 1$.
By using a both θ_x and θ_y dispersion, two dimensional wave-vector maps (E_k vs k_x and k_y) can be built by fixing the kinetic energy of the acquisition. Introducing proper spin detectors, it is also possible to perform spin-resolved ARPES (SARPES).
As dipole approximation holds, the spin is conserved in photoemission process thanks to the selection rule $\Delta S = 0$ and initial spin state can be inferred from polarization measurements on the photo-emitted electrons [73]. The spin polarization of electrons can be investigated using Very Low Energy Electron Diffraction (VLEED), present at the Elettra synchrotron. This detection system is located after the hemispherical analyzer and employs the spin dependent diffraction coefficient of electrons impinging on a ferromagnet. The ferromagnetic target is a Fe(001)-p(1x1)O ([9–11]) whose in-plane magnetization M can be switched through specific current pulses, leading to different reflection probabilities whereas the spin of incoming electrons is aligned to the magnetization (lower reflection) or not (higher reflection due to the absence of available states for absorption with same spin within the material). This effect is caused by the exchange scattering cross section, calculated by Kessler in [52] as:

$$\left(\frac{d\sigma}{d\Omega}\right)_{exc} = I(\theta)[1 + S(\theta)_{exc}\mathbf{P}\cdot\hat{\mathbf{m}}] \tag{3.23}$$

with $\mathbf{P}$ the electron beam polarization vector and $\hat{\mathbf{m}}$ the magnetization direction of the scattering centers. $S(\theta)_{exc}$ is the effective Sherman function, accounting for the asymmetry performances of the specific target in the case of both a polarized electron beam and an unpolarized one for a fixed geometry.
The reflected polarized beam of electrons is then collected by a channeltron detector located close to the ferromagnetic target and the electrons polarization can be retrieved comparing the electron current intensities detected for the opposite orientations of M (I_{up}

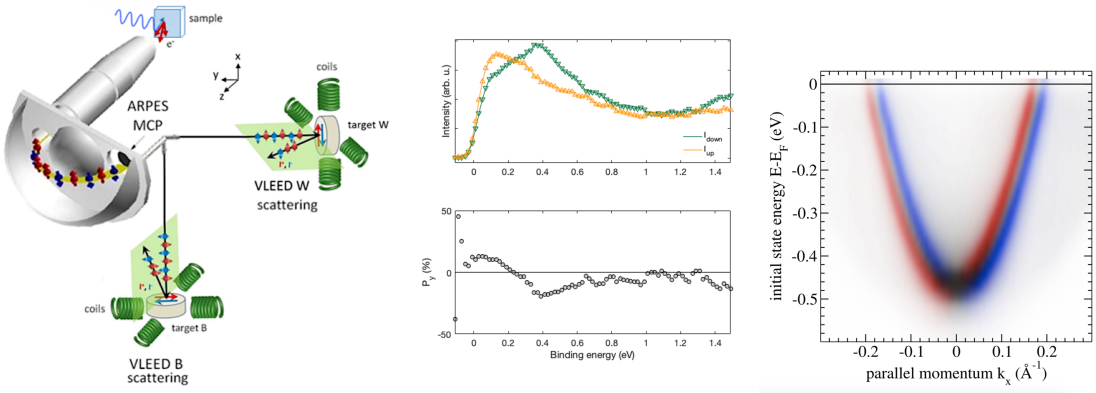

(a) (b) (c)

Figure 3.13: (a) Scheme of the S-ARPES setup with the two VLEED targets in order to investigate the 3D distribution of spin polarization. (b) Example of a spin scan at a particular k_x and k_y and (c) a spin map of Au(111) surface [95].

and I_{down}). The polarization is determined as:

$$S_p = \frac{1}{S(\theta)_{exc}} \frac{I_{up} - I_{down}}{I_{up} + I_{down}} \tag{3.24}$$

During experiments, the Sherman factor needs to be calibrated experimentally on a reference sample by a reference beam with a known degree of spin polarization as:

$$S(\theta)_{exc} = \frac{1}{S_{p0}} \frac{I_{up} - I_{down}}{I_{up} + I_{down}} \tag{3.25}$$

This powerful technique allows for the most complete analysis of energy bands, providing either plots with the electron counts vs E_b for fixed k_x and k_y during acquisition, as shown in figure 3.13b, or spin maps, like the one in figure 3.13c, in which only k_y (or k_x) is fixed and counts are represented by means of colour intensity for the two spin polarizations.

3.5. Ferroelectric characterization by current-voltage methods

The ferroelectricity of samples can be investigated studying the sample's polarization **P** either locally (measurement area $\sim$ nm^2) with Piezoresponse Force Microscope (PFM) or on a larger scale ($\sim 40 \times 40 \mu$m^2) using an electric technique.
PFM consists of an opportunely modified Atomic Force Microscopy (AFM) in which a conducting tip is used to sense the piezoelectric response of a material (exploiting the link between piezoelectricity and ferroelectricity presented in section 2.1), with a space resolution $\sim$ nm^2 given by the size of the tip [1]. Since PFM measures a mechanical quantity rather than a current, it suits both for insulating and semiconducting ferroelectrics [66]. Despite its potential, this technique was not used in our work, for which a large-scale character of ferroelectricity in the samples was considered more relevant.
The second type of measurements, namely current-voltage, has been used in the work: this type of analysis requires metallic contacts to be deposited on the sample (the size of contacts determines the resolution scale of the technique) and a probe station to contact the pads.

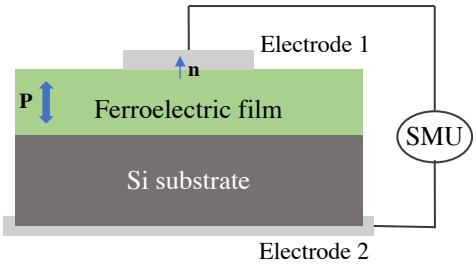

Figure 3.14: Scheme of a typical current-voltage measurement setup, with the signals applied by mean of a source measure unit (SMU).

The prototypical scheme for these measures is to place the ferroelectric film between top and bottom electrodes, as presented in figure 3.14. By applying a voltage between them, it is possible to change the polarization state of the film and detect this effect by measuring the displacement current. The polarization **P** of a material is associated with a charge distribution (surface σ_P and bulk ρ_P), but in the case of ferroelectrics the only charge density present is the surface one, located at the interface with the top and bottom electrodes, $\mathbf{P} = \sigma_P \, \mathbf{n}$, where **n** is the normal to the interface. Therefore, any change in time of **P** gives rise to a displacement current J_D.

This result can be directly obtained from Maxwell equations, considering the displacement field **D**, along the direction perpendicular to the thin films surfaces, e.g. $\mathbf{D} = \mathrm{D}\,\vec{u}_z$:

$$D = \epsilon_0 E + P \tag{3.26}$$

and the displacement current being:

$$J_D = \frac{\partial D(t)}{\partial t} = \epsilon_0 \frac{\partial E(t)}{\partial t} + \frac{\partial P(t)}{\partial t} \tag{3.27}$$

For a paraelectric material $P = \epsilon_0 \chi E$, with χ the dielectric susceptibility of the material, so that equation (3.27) reduces to the capacitor equation $J(t) = \frac{\epsilon_0 \epsilon_r}{d} \frac{dV}{dt}$. For a ferroelectric material instead, $P = P_r + \epsilon_0 \chi E$, so that the remanent polarization gives rise to an additional current term:

$$J_r = \frac{\partial P_r}{\partial t} \tag{3.28}$$

Thanks to this last equation, is possible to retrieve the polarization variation by integrating, over a finite time interval, the displacement current:

$$\Delta P_r = \int_{t_i}^{t_f} J_r \, dt \tag{3.29}$$

3.5.1. PUND

The commonly used current-voltage measurement technique is called Positive Up Negative Down (PUND) and it consists of a series of triangular voltage pulses applied to the electrodes, in the order presented in figure 3.15a, while measuring the total current (superposition of the capacitor current of the film and the displacement current). A first negative voltage pulse is used to initialize the sample's state. After this one, two positive pulses are sent: the first one induces the change in polarization direction and produces a current peak at the coercive field value, while the second is used as a reference background. I_U should be zero in an ideal dielectric, while it's not in the case of leaky materials and spurious effects. These effects are present both in I_P and I_U, so that they can removed by subtraction. The remaining current $I_r = I_P - I_U$ is normalized to the contact area and used in equation (3.29) to retrieve the polarization. The same considerations hold for the negative voltages, where $I_r = I_N - I_D$, so that the hysteresis loop for the polarization is obtained.

An example of this procedure is presented in figure 3.15, for a sample of $BaTiO_3$ taken from [80]. The opening of the current loop in figure 3.15c is related to the equivalent

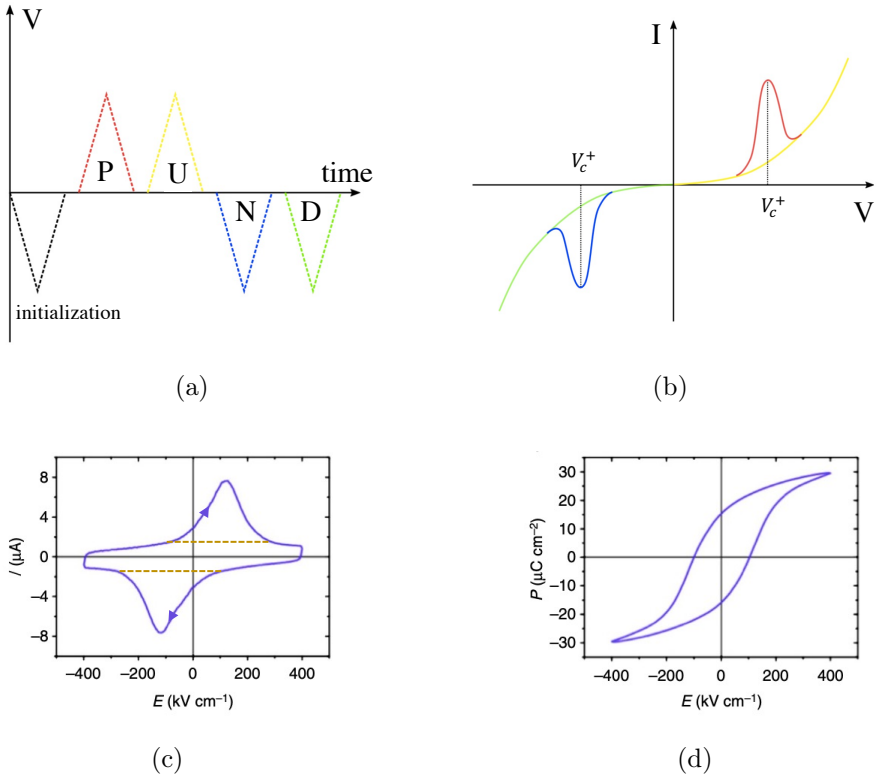

Figure 3.15: Positive Up Negative Down (PUND) working principle. (a) Series of pulses applied to electrodes, while in (b) the related currents (see respective colors) are reported: the peaks on the two sides are the switching currents. (c) and (d) report an example of the measured current and hysteresis polarization loop for a sample of $BaTiO_3$, adapted from [80]. The integration of I_r can be performed with respect to the voltage scale, being linearly proportional to time for voltage ramps.

capacitance of the system (e.g. wider opening corresponds to higher capacitance, since $I(t) = C \cdot \frac{dV}{dt}$ and $\frac{dV}{dt} = \text{const}$ for the applied voltage ramp).
This technique is fast and reliable for ferroelectric oxides, in which the current background (namely I_U and I_D)[12] is small ($\sim 0.3\,\mu A$) and the displacement current is high (typical $P \sim 30\,\mu C/cm^2$), but it is not suited for conductive samples, in which the switching current is buried in the background signal. For example in GeTe, the background current is 10^5 times larger than the expected displacement current. This issue opens the way to other current-voltage techniques, relying on a change in resistance of ferroelectric-metal interfaces, which is presented in the following subsection.

[12]The values presented as a reference are the ones related to the $BaTiO_3$ sample shown in figure 3.15, for which $(100 \times 100)\mu m^2$ electrodes were used.

3.5.2. Macroscopic gating: bipolar resistive switching

In order to overcome the issue of conductive samples in PUND measurements, another current-voltage technique has been developed during the study of GeTe-based devices in the work of S. Varotto et al. [97, 98]. This method focuses on the specific resistance of a metal-ferroelectric film interface.

When a semiconductor is interfaced with another material, its electronic bands experience a bending as a result of the electrostatic potential barrier at the interface. Considering the case of GeTe in contact with a metal, an Ohmic heterostructure is usually obtained due to its high density of free carriers ($p > 10^{19}\,\mathrm{cm}^{-3}$). For a non polar semiconductor, the depletion region (region in which a band bending is present) that forms in the semiconductor is:

$$X_d = \sqrt{\frac{2\epsilon_0\epsilon_r V_{bi}}{qN}} \tag{3.30}$$

Where ϵ_0 is the dielectric permeability in vacuum, ϵ_r the relative dielectric permeability ($\epsilon_r = 36$ in GeTe), V_{bi} the built in potential caused by the difference between the work functions of the two materials and N the dopant density.

The transport properties across the interface depends on the band structure, and the main conduction mechanism for highly p-doped semiconductors is tunneling of carriers across the barrier V_{bi}. The specific contact resistance can be expressed as:

$$\rho_c = \rho_{c,0} \cdot \exp\left(\frac{2V_{bi}}{h}\sqrt{\frac{\epsilon_r m^*}{N}}\right) \tag{3.31}$$

Where $\rho_{c,0}$ is a constant depending on the materials. The dependency of ρ_c on the potential barrier height V_{bi} and dielectric constant ϵ_r is the key to include the resistance dependency on the polarization.

The interface resistance can be retrieved by theoretical models describing electronic bands at the metal-semiconductor interface (known as a Schottky interface [91]) in the presence of a polarization state, with polarization vector perpendicular to the junction. A general model for transport properties of ferroelectric Schottky diodes was developed by P.W.M. Blom in [13], and was found to be suitable also for highly doped semiconductors (as GeTe and SnTe).

Such a model, whose detailed description goes beyond the scope of this thesis, predicts a bistable and hysteretic behaviour of the metal/semiconductor interface barrier by deriving a polarization dependent depletion width.

The result of this model is summarized in figure 3.16: the different orientation of the polarization moves the surface charges in the semiconductor, leading to different band

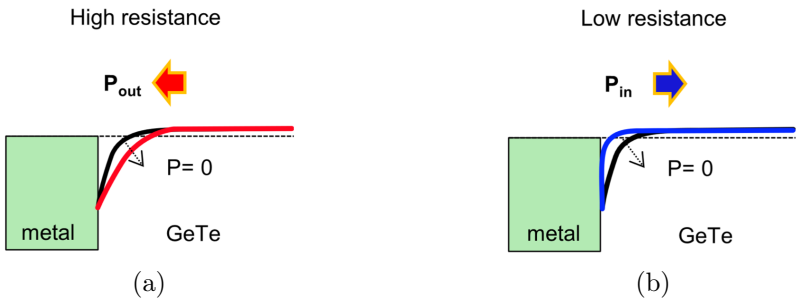

Figure 3.16: Schematic representation of the energy band profiles in a metal-semiconductor interface (metal-GeTe) for the ferroelectric remanent polarization pointing towards the metal (a) and towards the semiconductor (b).

bending at the interface. This results in a different depletion region (equation (3.30)) for the two cases and so in two resistive states (see equation (3.31)).

Bipolar resistive switching

The experimental technique to measure the resistive switching introduced in the previous subsection is here presented. The resistive switching method preserves the working configuration of *electrode-ferroelectric film-electrode*, but opens two different possible measurement geometries, with respect to PUND measurements (section 3.5.1), which are both presented in figure 3.17a: *top-bottom* gating, in which one electrode is located on the top surface of the sample and the other is contacted to the substrate, and *top-top* gating, in which both electrodes are contacted on the top surface of the sample.
When a top-top configuration is exploited, the bipolar switching is expected to take place under both contact pads in an opposite way. The only measured resistive switch correspond to unavoidable random asymmetries in the device. This leads this configuration less suitable for gating with respect to top-bottom, in which the contributions are effectively distinguishable. Nevertheless, this configuration could still be used in the case of rapid test for the ferroelectric behaviour of a material, relying on the asymmetry of measured pads (as a rapid test with no Ag-paste bonding of the sample required).
The probing technique consists of two different steps, presented in figure 3.17b:

- *writing step*, in which a rectangular pulse of variable intensity V_{write} (range ± 15 V) is used to modify the sample's state (e.g. direction of the polarization $\mathbf{P}$).
- *reading step*, in which a voltage ramp is applied to the electrodes while acquiring the current with an ammeter. The maximum applied voltage V_{read} needs to be small (e.g. < 1 V) in order to not perturb the ferroelectric state.

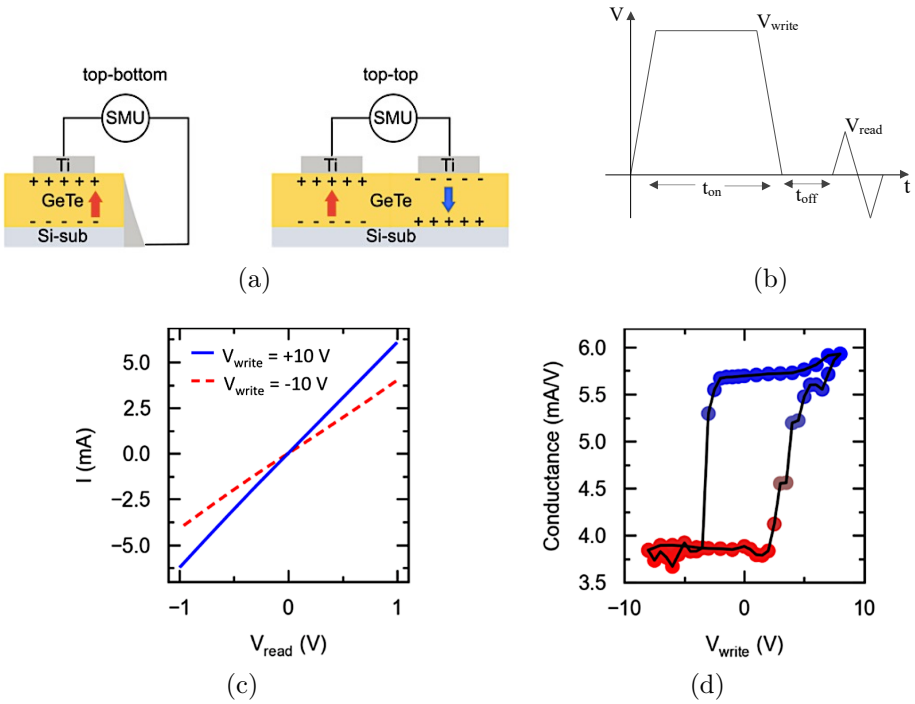

Figure 3.17: Overview of the bipolar resistive switching measurement method. (a) Reports the two possible working scheme: *top-bottom* on the left and *top-top* on the right. (b) Intuitive picture of the two steps of the measurement, *writing step* and *reading step*. (c) I-V curves for the two resistive states. (d) Example of a hysteresis resistance loop. For pictures (c)-(d), red (blue) correspond to low (high) resistance states.

The resistance of the system is then retrieved from the measured I(V) curves, reported as example in figure 3.17c, and, as described in the previous section, the polarization state can be inferred by this last. By changing the value of the writing potential V_{write} it is possible to obtain $R = R(V_{write})$ showing an hysteretic behaviour for ferroelectric materials, as reported in figure 3.17d It must be noted that the reading step allows to read the non-volatile state of the system without perturbing it. This is an appealing feature for memory applications, since in current technology the state-reading process is usually destructive (e.g. FeRAMs [102]) and needs to be written again afterwards.

3.6. Spin polarized electron gun

The scope of this section is to present the working principle of the spin polarized electron gun integrated in the LASSE setup (in the MC, see figure 3.1). The electron gun was first designed in 1992 [22] and modified in 2004 for improved performances [16]. Its original application was spin polarized inverse photoemission (SPIPE), in connection with a photon detector. In this technique, the empty states right above the Fermi level are

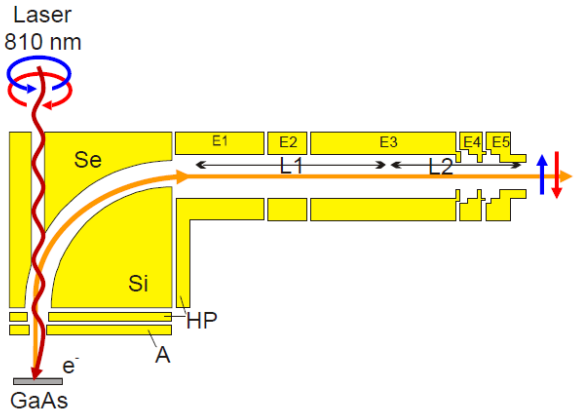

Figure 3.18: Scheme of the electron gun setup present in the Measurement Chamber (MC) at LASSE.

sensed by sending a beam of spin polarized low-energy electrons, which are absorded by the sample releasing a detectable photon [46, 74]. Exploiting the spin polarization of the electron beam, it has been possible to perform spin-sensitive absorption and reflection experiments on magnetic films (e.g. on MgO/Fe(001) samples [9]) and spin-sensitive transmission experiments on magnetic membranes [70].
The system is composed by a GaAs photocathode prepared in negative electron affinity (NEA) condition, a laser used to excite the photocathode and an electron gun made of two sets of electrodes (see also figure 3.18): the first section (composed by anode, Herzog plate and spherical condenser) is used to accelerate the electrons in the lens system at the right energy in order to obtain a collimated beam, while the second (composed by a set of cylindrical lenses) is meant for beam deceleration and focusing.

3.6.1. Electron beam generation

In order to generate the electron beam by photoemission from the photocathode, this last needs to be activated. The activation process prepares the GaAs photocathode to the Negative Electron Affinity (NEA) configuration with a dedicated procedure in the Photocathode Preparation Chamber (PPC) (see figure 3.1), which consists of: (i) annealing at 660 °C in order to desorb topmost layers, in order to remove all the contaminants, and (ii) deposition of a thin film of cesium and oxygen (Cs:O) by alternating Cs thermal evaporation and exposure to a O_2 flux [78]. While the first step leads to a clean GaAs surface, the second step leads to a thin layer of cesium oxide on top of the photocathode in order to create a stable NEA surface [3, 34, 110].
The photocathode is then inserted in the Measurement Chamber (MC), where its surface is excited with laser radiation of energy slightly larger than the GaAs gap ($E_{gap} = 1.422\,\text{eV}$

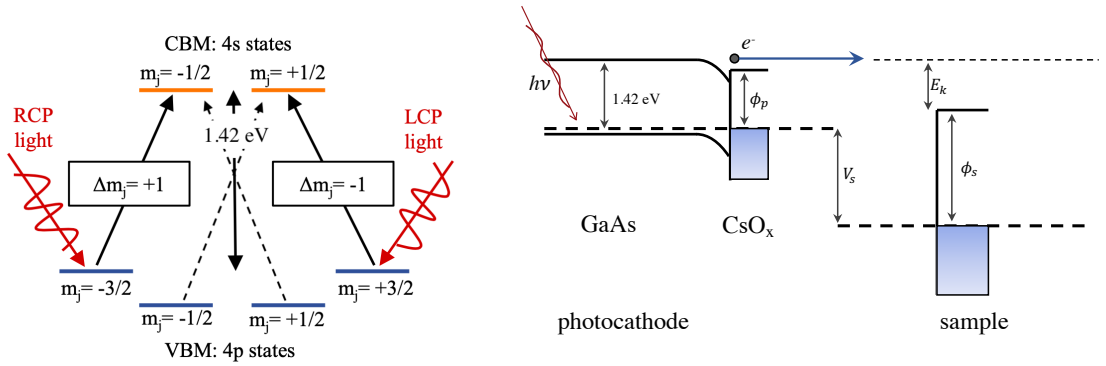

Figure 3.19: GaAs Negative Electron Affinity (NEA) photocathode. (a) GaAs bands triggered during laser excitation in order to produce a spin-polarized electron beam. (b) Energy scheme from electron emission until collection at the sample, with Φ_p and Φ_p being respectively the work function of the photocathode and the sample, V_s the difference in potential between the fermi levels of the two and E_k the kinetic energy seen at the sample. Adapted from [70].

at room temperature, while $h\nu \sim 1.5\,\text{eV}$ for $\lambda = 808$ nm) in order to trigger the transition $4p_{3/2} \rightarrow 4s_{1/2}$. Thanks to the momentum conservation rules during photoemission and a employing a circularly polarized light, it is possible to obtain a spin-polarized electron beam.

The valence band maximum originates from 4p states of As, with a splitted band structure originating from SOC, while the conduction band minimum comes from 4s states of Ga. The initial state has a fourfould degeneracy $(\pm 3/2, \pm 1/2)$ while the final only has twofold $(\pm 1/2)$. During photoemission, according to angular momentum conservation rule, the only transitions allowed are the ones with $\Delta m_j = 0$, for linearly polarized light, or $\Delta m_j = 1, -1$, respectively for right-handed (RCP) and left-handed (LCP) circularly polarized light. It can be seen from the band scheme presented in figure 3.19a.

For instance, with left-handed circularly polarised (LCP) light, the only allowed transitions are $4p_{3/2}(m_j = +3/2) \rightarrow 4s_{1/2}(m_j = +1/2)$ and $4p_{3/2}(m_j = +1/2) \rightarrow 4s_{1/2}(m_j = -1/2)$. Despite both spin polarization are present on the excited state, an unbalance between the two originates from the different transition probability, that are $p[4s_{1/2}(m_j = -1/2)] = 1/3 \cdot p[4s_{1/2}(m_j = +1/2)]$, leading to a beam polarization $P = (3-1)/(3+1) = 0.5$. This value defines the maximum obtainable polarization of 50%, while in real experiments $P \sim 25\%$ is obtained at the output due to the photon energy used, not perfectly resonant with the gap, and the depolarization effects in the GaAs, due to the finite spin coherence length, and in the electron gun.

The beam polarization can be switched passing from to LCP to RCP thanks to a Pockels cell located between the linearly polarized laser and the photocathode, thus obtaining

$P = \pm 25\%$. The Pockels cell induces a phase shift of $\pm 90°$ whether an high voltage of 1500-2000 V is applied in one direction or the other. Careful alignement of the incoming polarization axis with the crystallographic axis of the cell is required in order to obtain the right amount of phase shift.

3.6.2. Electron beam manipulation

Once emitted, the electrons are accelerated towards the electron gun by the anode (A) and Herzog plate (HP) electrodes, as in the ray tracing scheme in figure 3.20b, up to 300 V. The high electric field in the A-HP region allows to obtain a parallel electron beam at the entrance of the spherical condenser. This last is formed by two curved electrodes, Se and Si, set at constant voltages in order to fix the pass energy at $\sim 300\,\mathrm{V}$. Their aim is to rotate by 90° the electron beam propagation direction, while preserving its transverse section area. The second section, composed by the electrodes E2-E5, constitutes the deceleration and focusing section. E2-E5 can be set to variable voltage (0-500 V) in order to reach the best focus condition for every sample voltage V_s, whose meaning is explained in figure 3.19b.

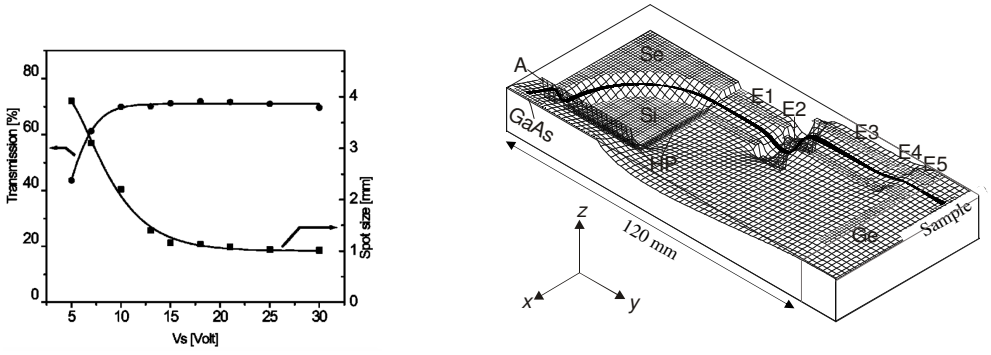

(a) (b)

Figure 3.20: (a) Beam characterization with respect to the voltage difference between the photocathode and the sample Fermi levels V_s as reported in [16]. (b) reports the ray tracing simulation performed for the standard working voltages of the electron gun setup. Adapted from [16].

The operational mode used in chapter 5 consists in keeping the photocathode grounded while the voltage of the sample-holder V_s is modified (positive values) in order to change the kinetic energy of electrons striking on it. A Faraday cup of diameter $d = 0.5\,\mathrm{mm}$ is located on the high precision sample-manipulator and can be used for the beam size and position characterization. In order to have electrons absorption on the manipulator, a positive kinetic energy is needed to overcome the work function of the sample/Faraday

cup (as shown in figure 3.19b, for $V_s < (\Phi_s - \Phi_p)$ no electrons reach the target, since they would have negative kinetic energy), thus setting a lower limit for $V_s \simeq 5 - 25\,\mathrm{V}$. Higher sample's voltage improves both the transmission and focusing of the electron gun, as showed in [16], reaching a stable transmission of $\sim 70\%$ and beam spot size $\sim 1\,\mathrm{mm}$ for $V_s > 15\,\mathrm{V}$.

These values are sufficient for IPE experiments, being the samples big enough, but a smaller beam is needed when dealing with small samples, such as the suspended membranes investigated in [70], with an active area of $1 \times 2\,\mathrm{mm}$. A smaller spot size is also needed for spin-injection experiments for vacuum STC conversion, since the size of devices for these experiments would be small and the presence of contact pads would limit the available area even more. In order to solve this issue, a laser with smaller spot size has been used, together with a modified set of voltages for the electrodes, in order to obtain better focusing. To this scope which a new control unit needed to be designed, improving beam stability and beam size by exploiting a different configurations of electrode voltages, larger than in the actual case. These improvements are shown in chapter 5.

4 | Growth and characterization of $Ge_xSn_{1-x}Te$ chalcogenide alloys

The principal scope of this thesis work has been the realization and characterization of ultra-thin films of the ternary alloy $Ge_xSn_{1-x}Te$, with different germanium concentrations, in order to explore new intermediate states, and their band structure evolution, between the FERSC GeTe and the TCI SnTe. The work is inspired by the previous work of Plekhanov et. al. [79] on the possible breakthrough in electronic bands engineering obtained by adding a lattice distortion to the SnTe cubic crystal, for which we recall section 2.5.2.

The experimental measures are supported by theoretical studies of the electronic bands in this alloy performed by the team of professor Picozzi.

A first attempt of working with the combination of SnTe and GeTe thin layers in a epitaxial heterostructure has been performed in the group where the thesis has been done. The deposition of thin layers of SnTe over a GeTe thin film has shown how the interdiffusion of the Ge atoms in the SnTe matrix is not negligible. This diffusion process, activated at $T \geq 250°C$, has been then investigated as a way to prepare GeSnTe films with controlled stoichiometry, in alternative to co-deposition of Ge, Sn and Te. The doping of the surface layers can be controlled by the thickness of the deposited SnTe (e.g. lower concentration of Ge for thicker SnTe layer).

The following chapter is divided as follows: section 4.1 is dedicated to the growth processes and in-situ characterization performed at Polifab; section 4.2 reports spin- and angle-resolved photoemission spectroscopy (S-ARPES) performed at the APE beam-line of Elettra synchrotron in Trieste; in section 4.3 we present the ferroelectric characterization of the alloy while the final section 4.4 is dedicated to an overall discussion and comparison of the obtained results with the theoretical predictions.

4.1. Growth of samples and in situ characterization

In order to find an application in devices in its ferroelectric phase, SnTe would need to be stable up to room temperature, but its Curie temperature is $T_c = 100\,\mathrm{K}$. In order to stabilize this phase, it has been exploited GeTe(111) as the underlayer for SnTe growth, so that GeTe polarization could favour the α-phase of SnTe through dipolar interaction. Both the polarization vectors for SnTe and GeTe, in their ferroelectric phase, are along the [111] direction, corresponding to the out-of-plane direction.
A great advantage when growing similar crystals heterostructures is to have a small difference between the lattice constants, thus reducing crystal defects produced during the process: in the case of SnTe deposited onto GeTe the mismatch is just $\sim 4\%$, being the lattice constants $a_{GeTe} = 4.373\,\text{Å}$ and $a_{SnTe} = 4.537\,\text{Å}$.
The growth of GeSnTe samples started from films of 18 nm thick GeTe grown by the group of S. Cecchi and R. Calarco at Paul-Drude-Institut for Solid state electronics of Berlin [14]. These samples are grown by physical deposition on a $Si(111)(\sqrt{3} \times \sqrt{3})$ reconstructed substrate; an Sb buffer monolayer is deposited on Si to allow subsequent crystalline growth of GeTe(111) in its α-phase [104]. The GeTe is then capped with $20\,nm$ of tellurium to protect it from air exposure.

4.1.1. Decapping procedure

Before starting the SnTe deposition, some pre-processing steps are necessary. The sample is first cut in $5 \times 10\ \text{mm}^2$ shape in order to fit on the sample holder and then it is cleaned with two acetone and isopropanol rinses in order to remove organic contaminants. Once the sample is inserted in the IC and moved to SPC (see section 3.1 for acronyms), the Te capping is removed by a dedicated procedure.
While the usual decapping procedure consists in an annealing step, this cannot be done directly on the GeTe samples. The evaporation temperature for the Te capping is $\sim 250°C$, temperature at which the oxygene atoms present on the surface (as TeO_x) diffuse within the inner layers and preferentially bonds with Ge atoms. The desorption of oxygen from the GeTe structure would require temperatures higher than the evaporation threshold for the GeTe itself (280°C), making the process not feasible.
The same procedure is applied also for decapping SnTe and GeSnTe samples (capped with a 20 nm of Te) since the issue of oxygen interdiffusion is common to all the three materials. The ad-hoc procedure consists of:

- *Oxide removal.* A rastering sputtering is performed with an Ar ion beam at grazing

incidence, with 1.5 kV energy and Ar partial pressure of $\sim 2 \cdot 10^{-8}\, mbar$, in order to sputter the oxide layer and residual organic components;

- *Annealing.* 30' annealing at 250°C in order to desorb the capping Te layer. A careful control of the temperature is necessary to avoid the evaporation of GeTe layers at $\sim$ 280°C.
- *Crystallinity check and stoichiometry.* The decapped sample's crystallinity is investigated through diffraction tools as low energy electron diffraction (LEED), reflection high-energy electron diffraction (RHEED) or X-ray photoelectron diffraction (XPD). The stoichiometry of the sample is measured from the XPS peaks, upon normalization, for the different elements, namely Ge_{3d} and Te_{4d} (and Sn_{4d} for GST samples).

Some additional stoichiometric analysis are done during the process in order to ensure the complete removal of the oxide while preventing the undesired sputtering of the GeTe thin film (figure 4.1). The presence of the capping layer can be deducted from a much stronger Te_{4d} with respect to the Ge_{3d} (or Sn_{4d}), being these two intensity peaks attenuated by the presence of the overlayer.
This procedure can be used both at LASSE and at the synchrotron facility, with the only difference of the XPS being done with different photon energies, thus requiring different normalization coefficients for the XPS intensity peaks: the ionization cross-section, the inelastic mean free path of electrons and the transmission of the analyser depend on the kinetic energy of electrons and therefore on the excitation photon energy (as discussed in section 3.4).

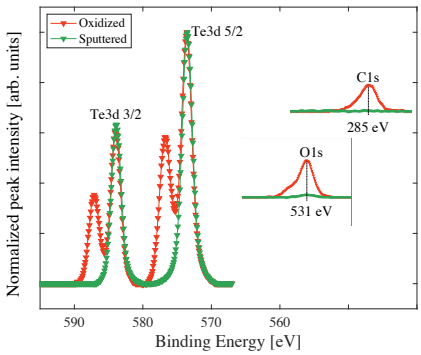

Figure 4.1: XPS spectra for sample ST3 (see section 4.2.1) during the sputtering process. The second peak in Te4d originates from the oxidized tellurium (after ambient exposure) due to chemical shift effect. In the second spectrum (green), this peaks are removed and the absence of oxygen and organic contaminants can be checked on their characteristic binding energies (on the two panels on the right).

4.1.2. SnTe deposition

The SnTe is grown on top of the GeTe film (18 nm thick) by mean of molecular beam epitaxy (MBE) from a single crucible containing SnTe fragments in the amorphous/ multicrystalline phase. In order to favour high crystal quality during growth, the deposition rate needs to be kept low ($\sim 2.4\,\text{Å}/min$) and the temperature of the sample needs to be $\sim$ 200°C. Higher substrate's temperature favours the surface mobility of the deposited material, which leads to layer by layer growth (see section 3.2), but also increases the desorption rate, so that the optimal temperature of 200°C has been found for SnTe. Another method that can be used in order to obtain crystalline SnTe is to perform the deposition at room temperature followed by an annealing at 200°C in order to let the lattice relax in the more stable configuration. This technique produces lower quality samples with polycrystalline structure, therefore it has not been exploited.
The stoichiometry of SnTe is cross-checked by an XPS analysis, while its crystallinity by XPD (reported in figure 4.2b), which allows to be chemically sensitive and characterize the single element behaviour. The measurement on the sample before annealing shows a similar geometrical distribution of Te and Sn atoms, corresponding to the ZA direction of the sample. The presence of an added peak at $\sim 20°$ for Sn could be related to the ferroelectric displacement of Sn atoms in the Te matrix. The presence of two different polarization domains within the investigated region could lead to multiple available axes for forward focusing (see section 3.4.2). This possibility is not excluded at this point, since the sample is not forced in one state or the other during growth (apart from the weak dipolar interaction of the GeTe underlayer), but it has been considered not crucial.

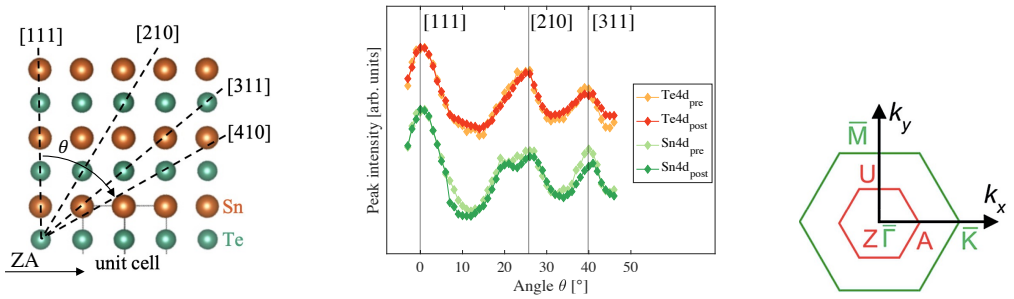

(a) (b) (c)

Figure 4.2: (a) Cross section of a SnTe sample and main crystallographic axis for the angle of XPD acquisition θ along the ZA direction. (a) XPD spectra for Sn and Te before and after the in situ annealing. The considered peaks are $Te4d_{5/2}$ at $E_b = 41\,\text{eV}$ and $Sn4d_{5/2}$ at $E_b = 25\,\text{eV}$. (c) Projection of the three dimensional Brillouin surface on the (111) direction.

4.1.3. Ge doping of SnTe

The presence of GeTe as underlayer allowed to exploit a quite unusual doping method: diffusion of Ge atoms from the GeTe film within the SnTe matrix was driven by an annealing at 250°C. Upon annealing, both Ge and Te atoms from the GeTe interdiffuse in the SnTe, causing either a substitutional or interstitial doping. The growth of SnTe is reported to show a high Sn vacancies concentration [94], also causing its p-doped character, therefore the dopants can fill the vacancies during the diffusion process.
In order to verify the quality of the sample after doping, stoichiometry and crystallinity are again investigated. Figure 4.2b reports the comparison of XPD spectra before and after doping for the Sn and Te atoms, respectively in green and orange with darker colours corresponding the post-doping, showing how the crystal structure of the SnTe matrix is preserved upon annealing. The data for Ge are not reported because of the low signal during the XPD acquisition: the Ge peaks are superimposed to the Te4d satellite, thus making them difficult to quantify in low counts measurements like XPD.
The XPS spectra in figure 4.3 show the different steps of the process: a first spectrum, figure 4.3b, is acquired to investigate the stoichiometry of the GeTe underlayer (thinner lines highlight the peaks components used for fitting); a second XPS is taken, after growth of SnTe in order to evaluate the stoichiometry before and after the doping process (the example in figure figure 4.3c is related to SnTe thickness of 20 nm).

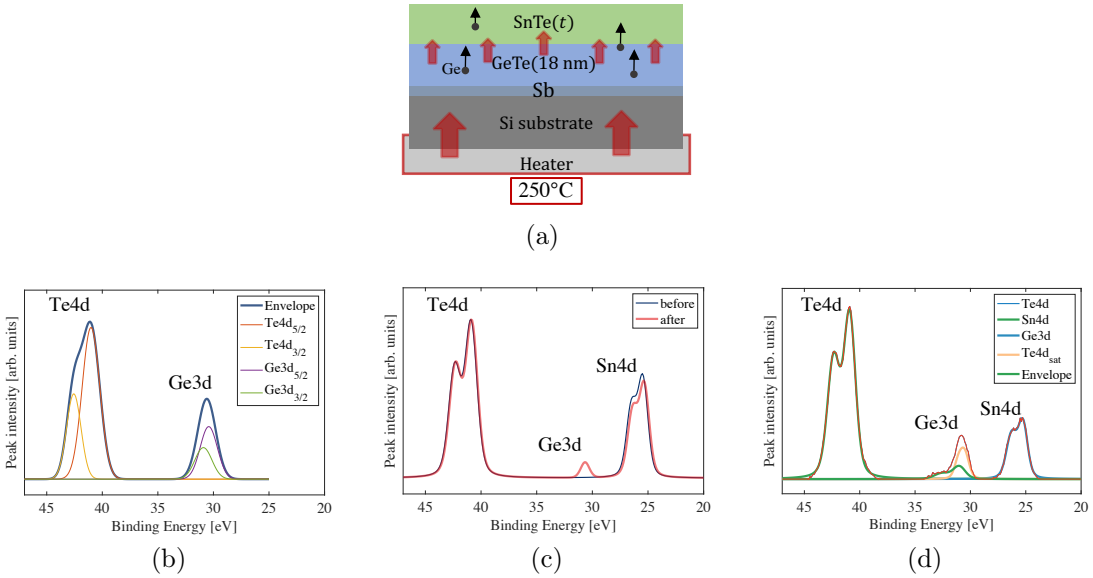

Figure 4.3: The schematic representation of the doping process activated by annealing is reported in (a). Both Ge and Te atoms tend to diffuse into the SnTe matrix. (b) XPS spectrum for GeTe underlayer before SnTe deposition, while (c) shows the spectra obtained on a GST sample with 20 nm SnTe layer before and after the doping process. (d) Spectrum used for stoichiometry of a GST sample with 5 nm of SnTe. The effect of satellite peaks is here highlighted. All the spectra were acquired with $u\nu = 1486.6$eV.

The final stoichiometry is obtained from equation (4.1), in which the intensity I of XPS peaks is normalized by the cross section σ (depending on the atomic orbital and the used photon energy), the inelastic mean free path λ_{IMFP} (depending on the material and electron's kinetic energy) and the transmission of the electron analyser T (depending on the electron's kinetic energy).

$$\frac{C_a}{C_a + C_b + C_c} = \frac{\left(\frac{I}{\sigma\lambda_{IMFP}T}\right)_a}{\left(\frac{I}{\sigma\lambda_{IMFP}T}\right)_a + \left(\frac{I}{\sigma\lambda_{IMFP}T}\right)_b + \left(\frac{I}{\sigma\lambda_{IMFP}T}\right)_c} \tag{4.1}$$

where C indicates the concentration of element a, b or c, which are Te, Sn or Ge (respectively considering the peaks Te_{4d}, Sn_{4d} and Ge_{3d}).
The photon energy used for in situ stoichiometry evaluation is 1486.6eV, corresponding to the Al(Kα) transition. For low binding energy peaks $E_k > 10^3$ eV and so $\lambda_{IMFP} \simeq 3\,\text{nm}$ (from equation (3.16)): normal incidence acquisition probes the bulk concentration and shows higher Ge contribution with respect to what expected on the outermost layers (due to the diffusion profile). A partial compensation of this bulk sensitivity on the final concentration estimates can be obtained by considering the attenuated contribution of the GeTe film to the measured intensity peaks. This allows to split the two contributions (GeTe, GeSnTe) and obtain a better estimate for the GST overlayer. The intensity of an electron beam propagating in a slab of material with thickness t is given by the Lambert-Beer law:

$$I_i(t) = I_i e^{-t/\lambda_{IMFP}} \tag{4.2}$$

Both I_{Ge}^{GeTe} and I_{Te}^{GeTe} present this attenuation (proportional to the deposited thickness t), while the intensity of electrons coming from elements in the upper slab are:

$$I_i^{GeSnTe} = C_i N_i \Phi T \sigma_i \int_0^t e^{-z/\lambda_i}\, dz = C_i N_i \Phi T \sigma_i \lambda_i (1 - e^{t/\lambda_i}), \tag{4.3}$$

where i could be either Ge, Te, Sn. Therefore the measured peak intensities are $I_{Sn}(t) = I_{Sn}^{GeSnTe}(t)$, $I_{Ge}(t) = I_{Ge}^{GeSnTe}(t) + I_{Ge}^{GeTe}(t)$ and $I_{Te}(t) = I_{Te}^{GeSnTe}(t) + I_{Ge}^{GeTe}(t)$ and it is possible to retrieve the composition of the GeSnTe layer.
The used doping method allows to obtain different concentrations of Ge atoms in the uppermost layers by a careful tuning of the thickness of the deposited SnTe.
This method also allows to both ensure the SnTe growth in the α-phase (the dipolar interaction with GeTe underlayer is needed) and dope the sample. Post-processing analysis has shown that the doping concentration distribution is satisfying for the purpose of the work, as reported in section 4.2.1. The diffusion profile is expected to produce a vertical

diffusion gradient in the sample, but since the spectroscopy techniques used are highly sensitive to the outermost layers, this is not a relevant issue.
Before exposing the samples to atmospheric pressure (to transport them to the synchrotron), a capping layer of 20 nm Te is deposited in order to prevent contamination. This capping layer has been then removed at the Elettra synchrotron, with the same decapping procedure shown in section 4.1.1, before the S-ARPES experiments.

4.2. ARPES and S-ARPES characterization

The grown samples with different Ge concentrations were characterized by mean of XPS and S-ARPES in order to evaluate respectively the composition and the band structure. The results of this analysis are presented in this section, by introducing the four samples taken into account and finally comparing their Rashba bands with the ones predicted by DFT modelling.

4.2.1. $Ge_xSn_{1-x}Te$ samples

Four different samples were taken into account for the band structure characterization, with a varying concentration x of Ge ($Ge_xSn_{1-x}Te$). As presented in the previous section, the doping was performed by an annealing-driven interdiffusion: the doping can be controlled by tuning the SnTe layer thickness.
Given the same GeTe film's thickness of 18 nm, a varying thickness of SnTe, from 5 to 20 nm, was used to obtain x values between 31.3 % and 54.2 %. The samples are labeled according to the increasing Ge concentration as ST1, ST2, ST3 and GT (this last being the pure GeTe sample), and presented in table 4.1.

name	SnTe thickness [nm]	x (Ge fraction) [%]	Te concentration [%]
ST1	20±1	31.3 ± 4.6	50.2 ± 4.8
ST2	10±1	43.0 ± 3.0	51.2 ± 5.1
ST3	5±1	54.2 ± 1.4	48.6 ± 4.9
GT	0	100	50.0 ± 1.5

Table 4.1: Ge-doped SnTe samples with the relative concentrations of Ge of the final compound $Ge_xSn_{1-x}Te$. The thickness of the SnTe layer and the estimated total concentration of Te are also reported in right columns. The sample GT is taken as a reference from previous studies of the team ([83, 98]).

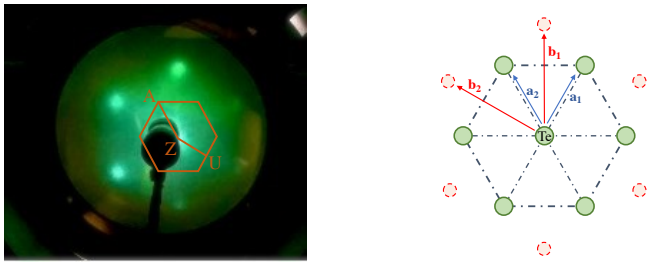

(a) (b)

Figure 4.4: (a) LEED image for the sample ST3 taken at the Elettra synchrotron. (b) Interpretation of the LEED considering the atoms on the surface for the (111) orientation. Vectors a_1 and a_2 define the direct lattice, while b_1 and b_2 the reciprocal lattice, which is observed by LEED.

Before the ARPES experiments, the samples were decapped applying the dedicated procedure presented in section 4.1.1 and a LEED image was taken to verify that the crytallographic order of the GST surface was preserved during transport and decapping. An example of the LEED pattern is reported in figure 4.4a.

After decapping, other XPS measurements were performed in order to check the stoichiometry of samples, with a synchrotron radiation at $h\nu = 70\,\text{eV}$ and $h\nu = 425\,\text{eV}$, for which the IMFP is respectively $\lambda_{IMFP}(70\text{ eV}) = 0.48\,\text{nm}$ and $\lambda_{IMFP}(425\text{ eV}) = 0.95\,\text{nm}$. The small λ_{IMFP} allows to obtain higher surface sensitive estimate of the stoichiometry with respect to the in-situ analysis without the GeTe underlayer contribution (being $t_{alloy} > 5\ \lambda_{IMFP}$ for all samples).

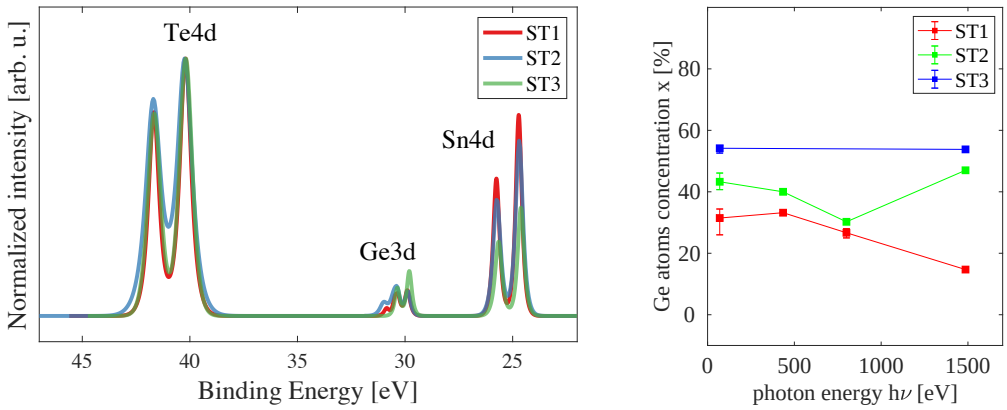

(a) (b)

Figure 4.5: (a) XPS spectra for the sample ST1, ST2, ST3 at the photon energies of 70 eV. The intensities are normalized at the Te4$d_{5/2}$ peak. The germanium concentration x estimates for the three samples are reported in panel (b) as a function of the photon energy. The error bar is here defined as the range of values obtained from different models/tabulated data for the σ, when available. For the energy 1486 eV (due to the higher IMFP of electrons), a suitable model has been used in order to account for the underlayer contribution.

For samples ST1 and ST2 it was also performed a measurement at 800 eV (λ_{IMFP} =

1.5 nm) in order to verify the bulkier concentration of Ge (this was not performed on ST3 since its smaller thickness makes the analysis less interesting). The estimated concentrations are reported in figure 4.5 as a function of the photon energy and the ones at 70 eV are reported in table 4.1. The reduction in Ge concentration observed at 800 eV is quite unexpected, since the Ge concentration should be higher in the underlayer. This suggests that the obtained samples, upon annealing (in-situ) and decapping (ex-situ), present a higher Ge concentration on the surface with respect to the immediate underlayer.
The stoichiometry obtained with 70 eV is taken as a reference in this discussion since it has the most similar surface sensitivity to ARPES measurements, in which $h\nu = 16 - 25\,\text{eV}$. The XPS spectra comparison at the photon energy $h\nu = 70\,\text{eV}$ is reported in figure 4.5a. The peaks are normalized to Te4$d_{5/2}$ intensity and the difference in height is also related to the element specific cross section of photoionization σ_i. Ge peaks in sample ST1 and ST2 do not show a single doublet, but a superposition of two of them. This is possibly related to a different chemical bonding in the samples: part of the Ge atoms may present a different chemical environment due to substitutional or interstitial doping, thus leading to the presence of the observed weak chemical shift. No further clarification has been possible from this point of view, due to the limited duration of the beamtime. Further investigation, focusing on the type of doping obtained and using a set of samples with similar characteristics, would be needed to clarify the doping dynamic (whether substitutional or interstitial) and the related chemical environments obtained.

4.2.2. Band structure analysis by angle-resolved PES

The band structure analysis for the set of samples has been performed during different beamtimes at the APE beamline in the Elettra synchrotron in Trieste with the support of the APE beamline staff.
The aim of these measures was to investigate the type of bands present in the alloy and whether the contribution of the doping was relevant. In order to do so, the energy bands were investigated at different photon energies (to distinguish between bulk and surface states, figure 4.6) and different temperatures (to evaluate the robustness of the band structure characteristics, figure 4.8).
The bands of interest for the alloy $Ge_xSn_{1-x}Te$ are located on the ZAU plane of brillouin zone (BZ) (figure 2.10a), where the bulk gaps of both GeTe and SnTe open and the topological states of SnTe reside. Remembering equations (3.20) to (3.22), the excited electrons have crystal momentum determined by their kinetic energy, which is in turns related to the photon energy used. Therefore, for a correct investigation of the ZAU

plane, photons with energy from 14 eV to 25 eV have been used [1].
In figure 4.6, the ARPES spectra of ST1 (x=31.3%) are reported for the different photon energies and $T = 77\,K$. In a typical ARPES dispersion map of binding energy vs $k_x(k_y)$,

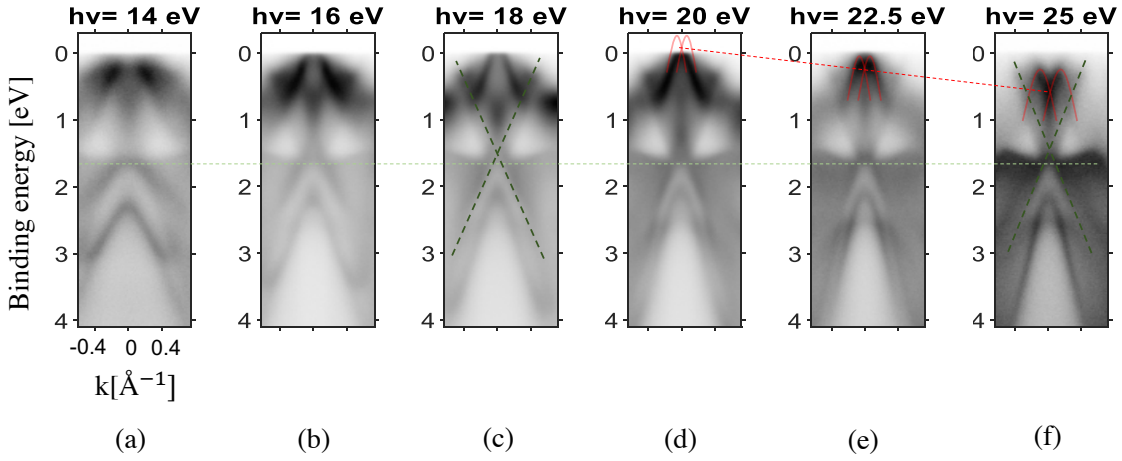

Figure 4.6: Photon energy dependent ARPES measurements for sample ST1. (a-f) Carpets along the ZA direction for $h\nu$ spanning from 14 eV to 25 eV. Green dotted lines highlight the two sets (darker and lighter green) of surface states (SS), present at all the photon energies, but enhanced only on the 18 eV and 25 eV spectra as a reference. Red parabola-shaped lines highlight the Rashba bands (RB), whose bulk behaviour is evident from the rigid shift of their intersection (dotted red line) with the photon energy.

bulk bands present a shift in energy with the photon energy, while the surface states are fixed. This same behaviour is recognizable in figure 4.6, in which two distinct features are visible:

- *Rashba bulk bands RB.* The bulk bands highlighted in red take the shape typical of Rashba bands. The crossing point is visible only at $h\nu \geq 20\,eV$, while at lower energies only the sides of the parabola-shaped bands are visible.
- *Surface states SS.* Some bands do not shift with the photon energy and are highlighted in green. These states have a cone like dispersion (darker green), whose centre lays around at $E_b \simeq 1.5\,eV$, which recall the topological states of SnTe. Other surface states are present, showing an almost flat dispersion at $E_b \sim 1.7\,eV$ (lighter green), which are less distinguishable due to the crossing with bulk states.

The sets of bulk and surface states depicted for ST1 in figure 4.6 can also be found in ST2 and ST3, with the signal coming from the "conic" surface states vanishing with the increase of x. This trend of the surface states suggest their SnTe origin, corresponding to

[1] previous calculations on GeTe showed that the momentum at $3\Gamma Z$ is $k = 2.73\text{Å}^{-1}$ and the photon energy suitable to probe the ZAU plane is $h\nu = 18$eV [83], similar to the values used in this work.

the topological states of SnTe. The almost total absence of this cone can be seen in panel figure 4.7d, reporting the GeTe case. In GeTe, surface states are located closer to the A and U points in the ZAU plane as reported in [83].

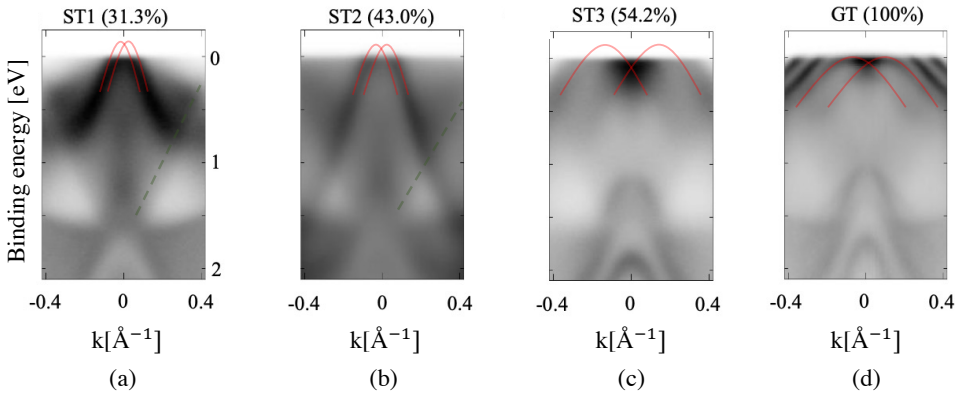

Figure 4.7: (a-d) ARPES carpets for four different samples with different Ge concentrations (written in brackets). The measurements are performed at $h\nu = 20\,eV$ and temperature $T = 77\,K$ along the ZA direction. The surface states with conic shape are highlighted with the dashed green line at positive k and left visible at negative values of k for the comparison between different figures. The bulk Rashba bands are highlighted and a broadening trend is visible increasing the concentration. Sample GT has been analysed in previous work [83].

Experiments conducted at the temperatures of $150\,K$ and $320\,K$ showed a similar behaviour of bands, with a lower resolution given by the increase of thermal noise. In figure 4.8 the constant energy cuts are presented (i.e. with both k_y and k_x dispersion) for two different photon energies, being $h\nu = 20$eV in figure 4.8a and $h\nu = 25$eV in figure 4.8b. From this representation it is possible to recover the hexagonal symmetry of energy bands and verify the alignment of the sample with the electron analyzer in order to find the $k_y = 0$ and $k_x = 0$ points (identifying the ΓZ direction in BZ).
Referring to the presented isoenergy cuts, the k_x and k_y axis correspond to the ZA and ZU directions respectively. At 20 eV it is possible to see higher density of states in the proximity of the Fermi edge (lowest binding energy) along the ΓZ direction with respect to the 25 eV case. This last shows a wider gap, related to the fact that we are sampling electrons located below the ZAU plane, as previously seen in the carpets vs photon energy (figure 4.6).
For what concerns the temperature dependence, no evident sign of band modification can be noted from the measurements. Overall, this proves the stability of the band structure at room temperature. Being the presence of Rashba bands strongly related to the distortion of the lattice, the stability of Rashba bands at RT implies the presence of a structural distortion in the GeSnTe alloy samples, thus proving the stabilization of α-SnTe by dop-

ing with Ge atoms. At low concentration of Ge (e.g. ST1, x=30%, and ST2, x=43%), both the topological states originated from SnTe and the Rashba splitting caused by the lattice distortion are proved to be present.

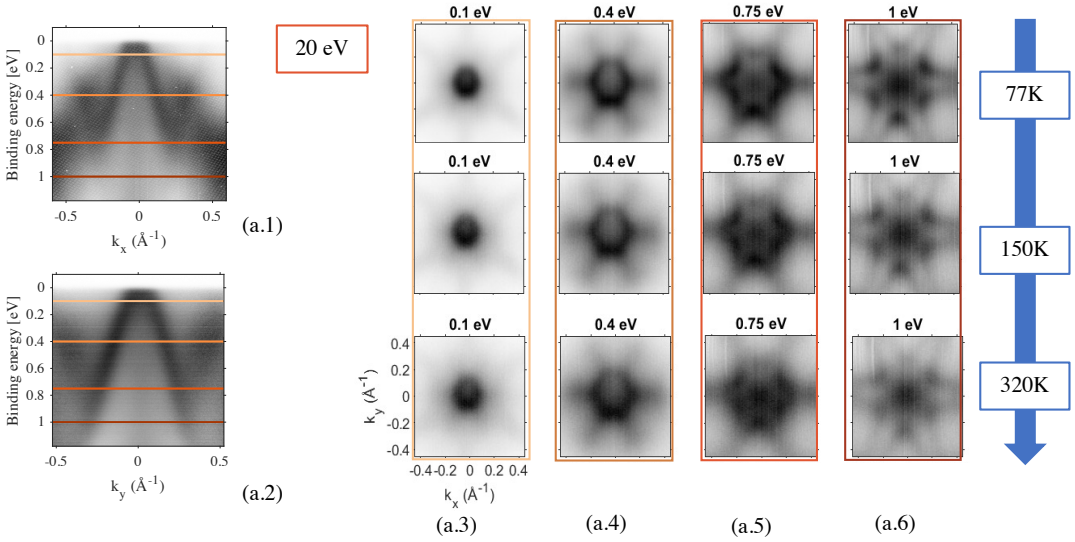

Figure 4.8: (a) ARPES data relative to ST1 obtained at $h\nu$ = 20eV while (b) at $h\nu$ = 25eV. The reported figures show the carpet along the k_x(a.1-b.1) and k_y(a.2-b.2) with the colored lines highlighting the binding energies of the isoenergy cuts presented in (.3-.6) panels for either (a) and (b). The panels in (.3-.6) show the isoenergy cuts at varying sample's temperature going from 77 K to 320 K, at binding energies of 0.1 (a.3),0.4 (a.4), 0.75 (a.5) and 1 eV (a.6) for $h\nu$ = 20eV and 0.05 (b.3),0.3 (b.4), 0.5 (b.5) and 1 eV (b.6) for $h\nu$ = 25eV.

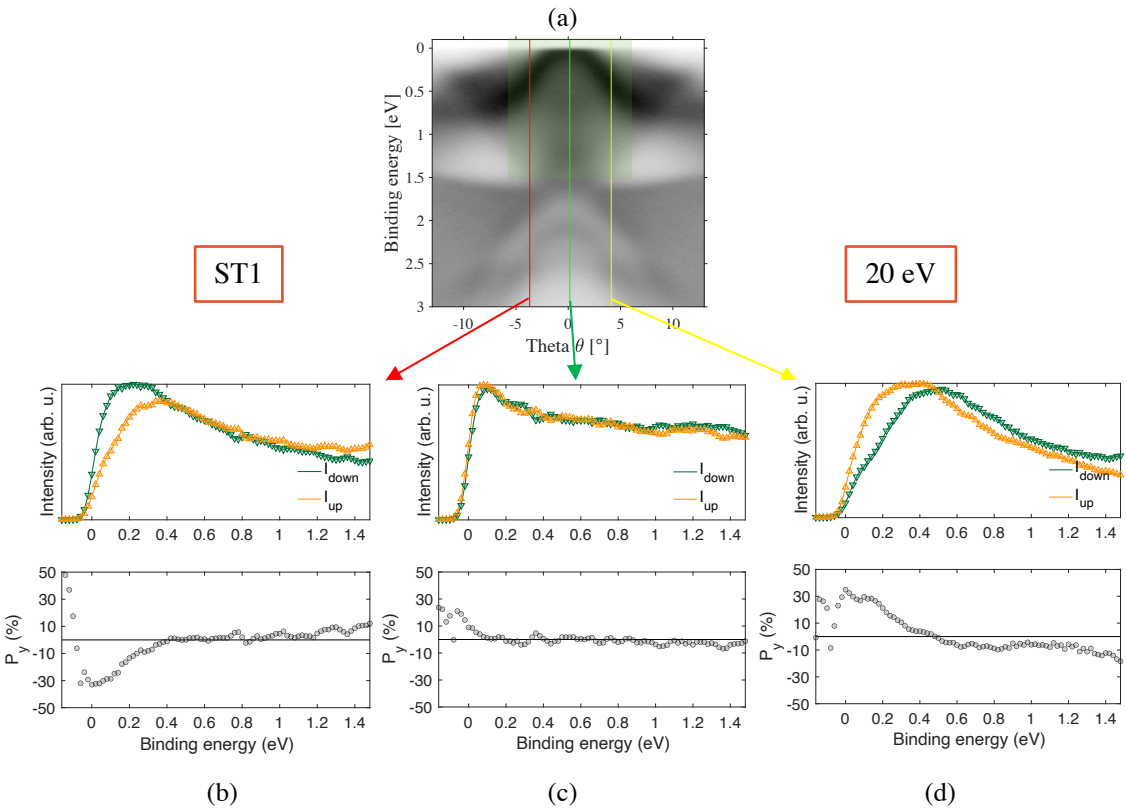

Figure 4.9: SARPES measurements relative to ST1. Working conditions: $h\nu = 20\,\text{eV}$, $T = 77\,\text{K}$. (a) ARPES carpet along the ZA direction, with highlighted lines corresponding to the three spectra acquired at fixed momentum k_x and k_y. (b-c-d) Spin dependent measurements performed with a VLEED detector, in the upper panels I_{up} and I_{down} are shown, while the spin polarisation is presented in the bottom panel, calculated with equation $P = A/S$, where A is the asymmetry and S the Sherman function (see equation (3.25) for its expression).

4.2.3. Spin resolved band structure analysis by S-ARPES

The availability of a spin-resolved spectroscopy allows for a deeper understanding of the previously seen bands. In this work, the spin-resolved ARPES (S-ARPES) was used in order to observe the spin polarization in the bulk Rashba bands. Some spin-resolved spectra at fixed k_y and k_x were acquired (also called *spin scan*) sampling the relevant points along the ZA direction, therefore at fixed $k_y = 0$.

The spin sensitivity is obtained thanks to the VLEED detector showed in figure 3.13a. The intensity of upward (downward) oriented spin polarization electrons is obtained by two consecutive spectra acquisition, between which a magnetic field pulse is applied to the detector in order to switch the spin sensitivity. The effective polarization has to be computed afterwards accounting for the experimental coefficients characteristic of the VLEED, represented by the Sherman coefficient (see equation (3.25)).

Three of these spin scans, acquired at $T = 77\text{K}$ and related to the sample ST1, are

reported in figure 4.9. The choice of k_x is driven by the interest in the spin-polarization of energy bands at opposite values of momentum, while the $k_x = 0$ acquisition is needed to verify the correct alignment of the detector with the ΓZ direction.
Some relevant features can be remarked:

- At $k_x = 0$ (corresponding to ΓZ direction), the spin polarization is almost absent, as expected by symmetry for the Rashba bands (e.g. figure 2.3c).
- The spectra at θ equal to $+4.5^\circ$ and - 4.5° show opposite sign of the spin polarization, as expected the Rashba model.
- At larger binding energy ($E_b \sim 1.4\,\text{eV}$) the spectra intersect the cone-shaped surface states and also here an opposite direction of spin polarization is measured for the two opposite acquisition angles.

It can be noted that the obtained polarization values, shown in figure 4.9b-d, are more reliable in the regions with a larger counting rate, above the Fermi energy, since the noise contribution gets dominant for fewer counts.
The same analysis, involving spin-resolved spectra (spin scans), has been performed for all samples in order to confirm the spin-polarization characteristic of bands. The results concerning ST3 are reported in figure 4.10. In this case, three different spin scans relative to positive k-vector are reported, in order to highlight the dispersion of spin-polarized bands with respect to k. The same unpolarized structure is find along the ΓZ direction ($k_x = 0$), while it can be noticed that the spin-polarized bands tend to split increasing the momentum k. Two distinguished bands with opposite spin polarization can be identified and are highlighted in figure 4.10a with the dashed yellow and green lines, respectively.
The analysis on ST3 also consisted of a spin-resolved carpet acquisition, shown in figure 4.11, with the focus on a limited area of the BZ due to the extremely time-consuming type of measure. In the reported spin map, it is possible to recover the characteristic trait of Rashba bands, with two parabolas having opposite spin-polarization that cross each other. The crossing point is located at $E_b \simeq 0.3\,\text{eV}$, while the k-vector at the maximum of the parabolas is $|k_{edge}| = k_r = 0.05\text{Å}$. This type of measurement offers a straightforward characterization of the spin-polarization in the band structure (much easier to interpret with respect to spin scans previously shown), thus allowing to retrieve the Rashba parameters k_r and α_r. These parameters are used to quantify the intensity of Rashba band splitting and comparing different materials, as will be done in section 4.4.

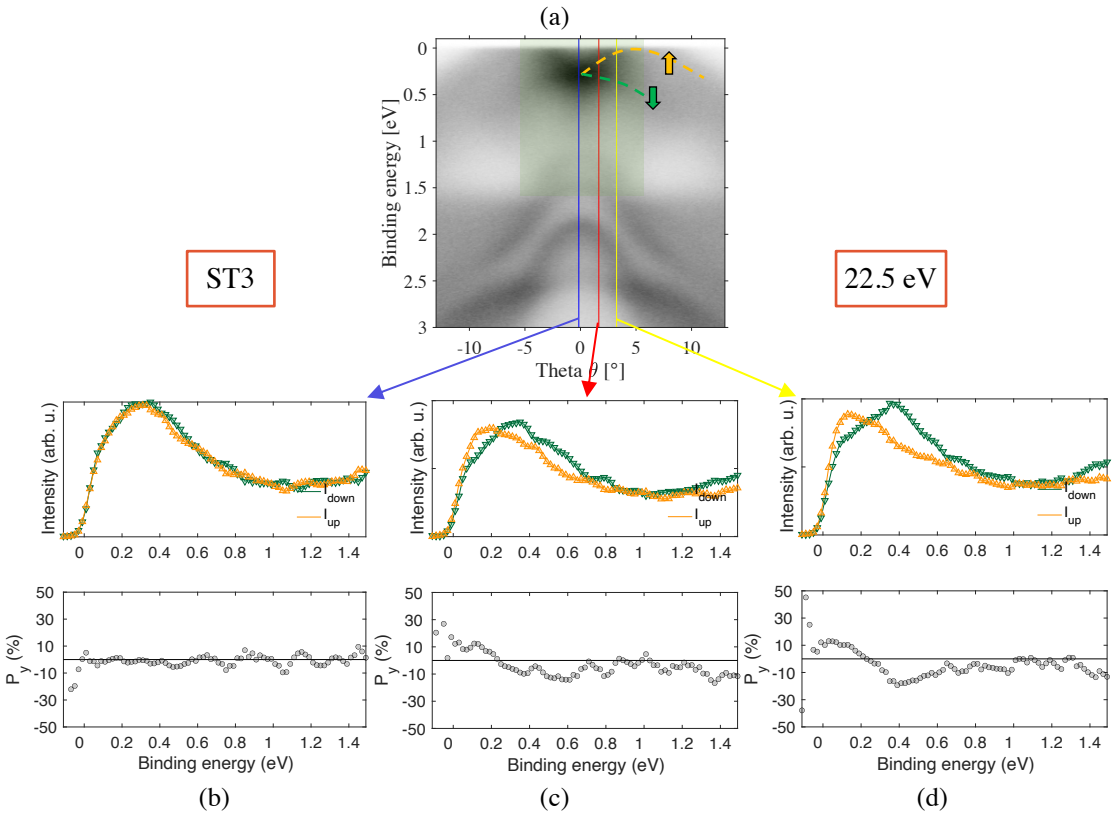

Figure 4.10: SARPES measurements relative to ST3. Working conditions: $h\nu = 22.5\,\text{eV}$, $T = 77\,\text{K}$. (a) ARPES carpet along the ZA direction, with highlighted vertical lines corresponding to the three spectra acquired at fixed momentum k_x and k_y. The yellow and green dashed lines in (a) show the resulting spin-polarized band dispersion. (b- c-d) Spin dependent measurements performed with a VLEED detector, in the upper panels I_{up} and I_{down} are shown, while the spin polarisation is presented in the bottom panel, calculated as in figure 4.9.

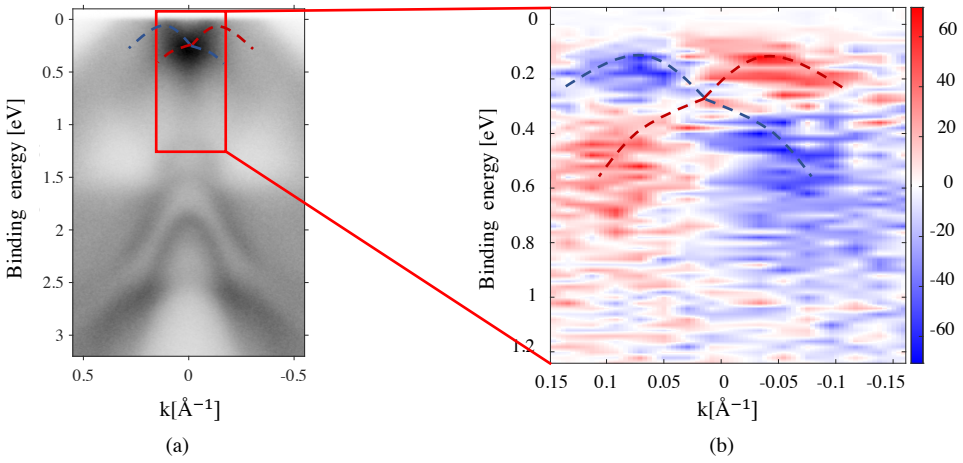

Figure 4.11: (a) ARPES carpet related to the 22.5 eV photon energy measurement along the ZA direction for the sample ST3, performed at $T = 77\,K$. (b) Two dimensional spin-map of the highlighted region in panel (a). The blue and red colors represent the two opposite states of the in-plane spin polarization while the dotted lines are used to highlight the Rashba bands in the two figures.

4.3. Ferroelectric characterization

Once found the Rashba bands in the alloy samples, it is interesting to verify whether they present also the ferroelectricity character typical of FERSC. For this scope, electrical measurements were performed on the sample ST3 in order to investigate its out-of-plane spontaneous polarization.

Typical ferroelectric materials are oxides, and therefore the PUND technique is usually employed to this scope (see section 3.5). As shown for GeTe [98], also SnTe presents an issue with this type of measurement due to its high conductivity (caused by the p-doped character). Therefore the ferroelectric characterization was performed by bipolar resistive switching measurement (see section 3.5).

A grid of Ti pads ($\sim 40 \times 40\,\mu\mathrm{m}^2$, thickness of 100 nm) was deposited on the GeSnTe surface as electrodes. The measurement was performed at a probe station, with small needle contacts (shown in figure 4.12a), where the voltage pulses are applied to the electrodes by a source measure unit (SMU). Considering the heterostructure of our samples, some considerations on the relevant interfaces in this experiment can be done for both configurations.

In the *top-bottom* scheme, the current flows perpendicularly to the heterostructure, encountering three main resistive terms (shown in figure 4.12b): (i) $R_{met\text{-}SC} = R_{met\text{-}SC}(\mathbf{P})$, representing the Schottky interface between the semiconductor (SC) and metal pad, which is the interesting term for bipolar switching, (ii) R_{int}, being the internal resistance of the SC, negligible with respect to the interfacial contributions, (iii) $R_{SC\text{-}Si}$, for the SC-silicon interface, including also the Sb buffer layer (this term is expected to be smaller with respect to $R_{met\text{-}SC}$ since the contact surface is much larger, but still not negligible due to the insulating character of Si). The contribution of the SC-metal interface plays the most relevant role, being the only term affected by the switching process, while $R_{SC\text{-}Si}$ leads to a backgorund in the measurements. For the *top-top* scheme, the current within the sample flows parallel to the surface, allowing to neglect internal interfaces contributions (due to the relatively high conductivity of the SC). The relevant resistances terms are now: (i) $R_{met\text{-}SC(1)}$, (ii)$R_{met\text{-}SC(2)}$ and the negligible (iii) R_{int}. The contribution of (i) and (ii) should be opposite, representing them two counterposed Schottky diodes, so that no resistive switching should be measured. Nevertheless, due to the stochastic variance of the resistance for different pads, it can happen that the difference between (i) and (ii) allows one of the two terms to be dominant (higher absolute resistance leads to an uncompensated switching). This second method prevents the current to flow in the Si substrate, thus avoiding the additional resistance $R_{SC\text{-}Si}$.

Both *top-top* and *top-bottom* configurations were used and the results for the first one

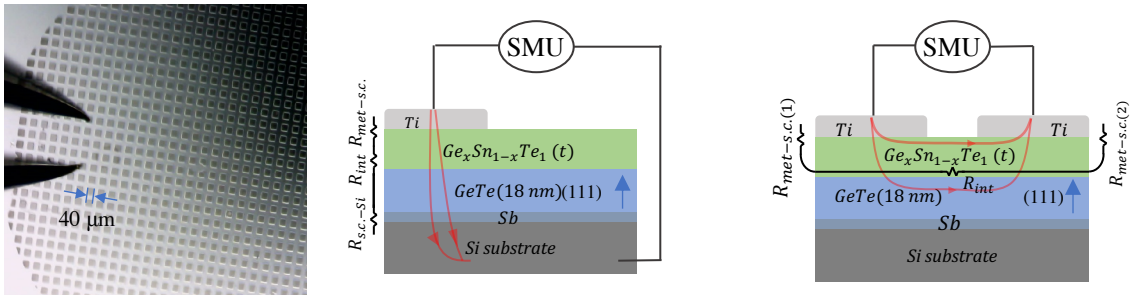

(a) (b) (c)

Figure 4.12: (a) 2-probe setup for top-top measures of ferroelectric resistive switching. (b) and (c) report the schematic of the two probing configuration, respectively top-bottom and top-top, for the GST alloy films grown in this work. The relevant resistances are reported in figure for the two cases, with R_{met-SC} the variable resistance with the sample polarization.

are reported in figure 4.13. For both cases, the probing technique consists of two steps, presented in figure 4.13a:

- *writing step*, in which a pulse of variable intensity V_{write} and duration t_{on} is used to modify the sample's state (e.g. the direction of **P**). Typical values are $V_{write} = [-10 : 10]\,\mathrm{V}$ and $t_{on} = [0.2 : 5]\,\mathrm{ms}$.
- *reading step*, in which a positive and a negative triangular pulses, with peak voltage $V_{read} = [-0.2 : 0.2]\,\mathrm{V}$, are applied. A characteristic I(V) is recorded in order to retrieve the resistance value. Low applied voltages are needed in order to both stain in the linear resistance region of the Schottky diode and avoid any perturbation of the polarization state.

Recording the estimated resistances as a function of V_{write}, we obtained the hysteresis loop of the resistance.
The t_{on} can be used in order to evaluate the speed of response of the process, while it should be kept as low as possible in order to avoid local over-heating (e.g. the working value used are $1 \div 5\,ms$). For $t_{on} < 0.2\,\mathrm{ms}$, no polarization-switching was recorded, while more repeatable measures were performed with $t_{on} = 2\,\mathrm{ms}$, as the example presented in figure 4.13.
The results obtained for ST3 show an hysteresis loop with $\Delta R \sim 170\%$ and a coercive voltage $V_c = 2.05\,V$, shifted towards positive values by the presence of built-in potential $V_{b.i.} \sim 0.9\,V$.
These preliminary studies confirm the ferroelectric nature of the sample at room temperature. The choice of the *top-top* scheme for the analysis aims to exclude the contribution of the GeTe underlayer. In order to support the results obtained so far, measurements on a sample not presenting the GeTe underlayer are needed. This would allow to exploit

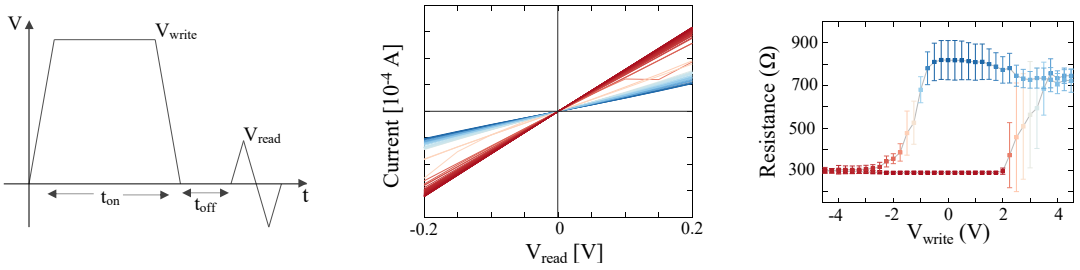

(a) (b) (c)

Figure 4.13: (a) Voltage pulses scheme for a bipolar resistive switching measurement, in which V_{read} varies in order to perform an hysteresis loop. The current (b) and resistance (c) measured as a function of V_{read} show the hysteretic loop expected for the sample ST3 in *top-top* configuration.

also the *top-bottom* configuration and isolate the pure contribution of the alloy GST. The aim is to find support of these preliminary results with measurements on samples of $Ge_xSn_{1-x}Te$ directly grown by co-evaporation MBE.

4.4. Discussion of the results

The results shown in previous sections have been compared to Density Functional Theory (DFT) calculations, performed by co-workers of the author, in order to support the experimental data. The ARPES measurements presented in section 4.2.2 demonstrated the possibility to engineer the band structure of the alloy thanks to the control of Ge doping. The possibility of reaching an intermediate state between the cubic SnTe, not presenting any Rashba splitting, and the fully distorted rhombohedral structure of GeTe, presenting Giant Rashba splitting, proves the tunability of these bands upon doping. The presence of the ferroelectric phase was verified by the current-voltage measurements shown in section 4.3 after the evidence for bulk Rashba bands to survive at room temperature (figure 4.8).

A common estimate for the Rashba splitting is the Rashba k vector k_{Rashba}, representing the k vector at which valence Rashba bands reach their maximum. The values retrieved from this work are reported in figure 4.14a in comparison with the values predicted by DFT. A steep increase of k_{Rashba} is present at the concentration of ST3 ($x \sim 54\%$) and in the pure GeTe sample. Further investigations are still needed, anyway we notice that the increasing trend of k_R vs. %Ge qualitatively agrees with calculations.

Unfortunately, the resolution of ARPES measurements was not enough to retrieve precisely the Rashba bands crossing point, therefore not allowing to compute the α_{Rashba} (see section 2.2).

In figures 4.14b to 4.14e are also shown the DFT-calculated bulk bands at different values

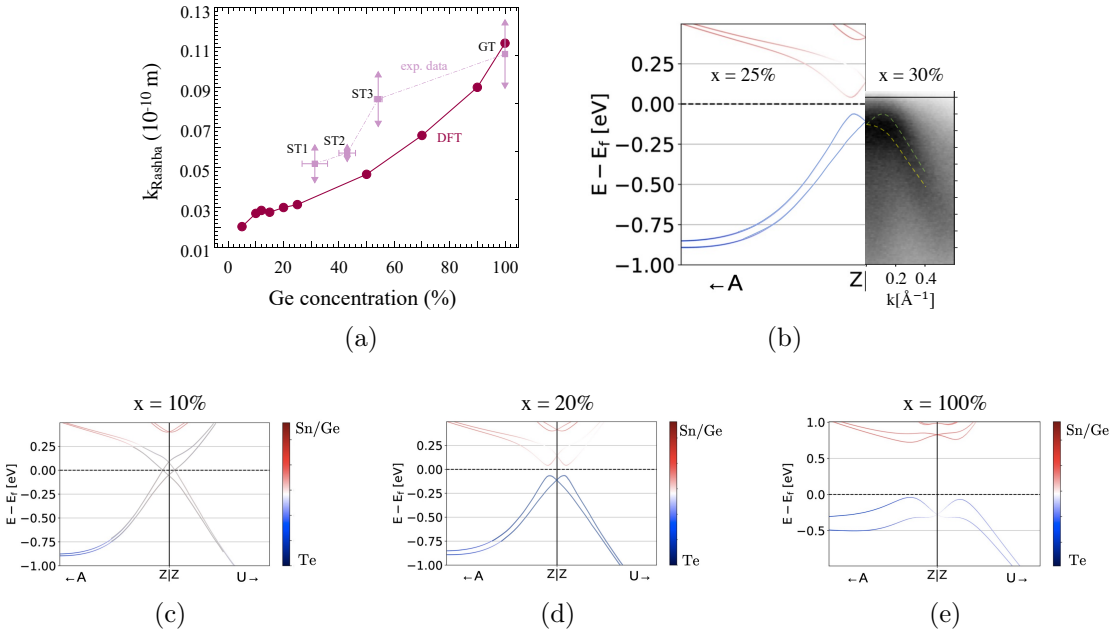

Figure 4.14: Density Functional Theory (DFT) results compared with experimental data. (a) Shows the exp. data for the Rashba k vector (i.e. the k vector at which the valence band has its maximum) compared to the ones predicted by DFT. Panels (b-c-d-e) show the predicted bulk bands for DFT at germanium concentration x of 10% (c), 20% (d) and 100% (e). The experimental ARPES carpet for sample ST1 ($h\nu$ = 22 eV, T=77 K) is reported in (b) together with the predicted bands at a similar concentration of Ge ($x = 25\%$). The yellow and green lines highlight the spin polarization of the bands.

of the Ge concentration x ($Ge_xSn_{1-x}Te$). The comparison between the ARPES measurement for ST1 ($x \simeq 30\%$) and the DFT bands for $x = 25\%$ is reported in figure 4.14b and shows a good agreement between the two. The spin-resolved analysis also allowed to determine the spin polarization of the two bands presented in the figure, highlighted with different colors (see also figure 4.9).

We so far observed the presence of bulk Rashba states and surface topological states (at x<40%), but new peculiar band structures are predicted to be appear reducing the x. It is worth noting as both the bandgap at the Z point and the splitting of bands decreases by reducing the amount of germanium. At low concentrations of Ge (e.g. $x < 20\%$) the bandgap vanishes, originating non trivial bulk conducting states. Therefore, close to the Fermi edge, are expected both bulk and surface states with topological non-trivial properties (contributing to conduction properties), thus opening new captivating paths of further investigation.

5 | Electron gun control unit: design and realization

The scope of this chapter is to present the design, implementation and characterization of the control unit (CU) for the electron gun available in the Measurement Chamber (MC) at LASSE. The electron gun is a fundamental component for electron beam manipulation in the instrumental setup. The electrons are first generated by photoemission from a GaAs photocathode, excited by a laser with energy close to its energy gap ($\lambda = 808$ nm, corresponing to $h\nu \simeq 1.5$ eV$> E_{gap} = 1.42$ eV), and then accelerated into the electron gun, whose scope is to transport and focus the electrons to the sample's position. The electron gun is constituted by a set of electrodes, to which a voltage is applied (ranging from 10 to 500-700 V) that is controlled by the CU. The complete working principle is presented in section 3.6.

The previously used CU was composed by a set of voltage generators, analogically controlled by high precision potentiometers. The electrodes require stable voltages over all the operating range (0-700 eV) since small variations could affect the beam shape and/or orientation, reducing the output current (e.g. a $\Delta V = 1\,\mathrm{V}$ at one of the electrodes Se or Si can lead to a change in transmission of the overall system $\Delta T \sim 20\%$).

The beam deflection caused by a wrong potential set leads to the scatter of electrons on the electrodes (and consecutive adsorption) instead of their propagation across them. The adsorption of electrons can be readily measured by reading the current flowing between the electrodes and the power supply (that in principle should be zero being the electrode an open circuit), as depicted in figure 5.1. This measure is performed at a potential higher than ground (the one of the considered electrode itself) and therefore has to be requires a floating ammeter. The overall transmission of the system can be then improved by reading and minimizing the current at the electrodes. The previously used control unit (CU) did not allow for current readings at the electrodes, for which a temporary solution was found by reading some values with an external multimeter (which is floating), but that requires to be operated at high voltages by the end-user.

Moreover, a reason for the development of the new CU was found aiming at reducing

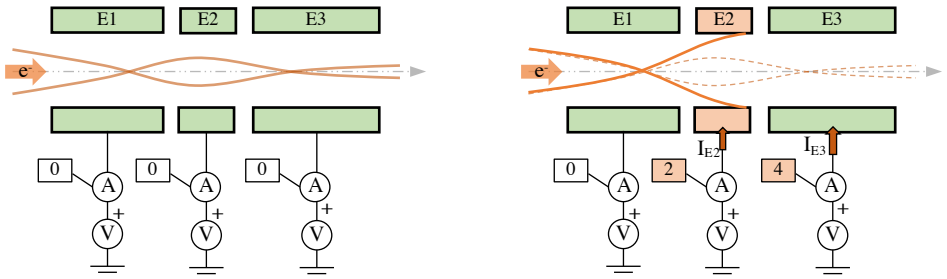

Figure 5.1: (a) Example of an electron beam correctly propagating through the electron optical system and (b) a wrongly focused beam leading to a readable current at the electrodes that adsorb part of the electrons. The potential is set by the voltage generator V, while the current is read by the ammeter A in series with the electrode, whose value is expressed in μA.

the beam diameter: the beam diameter gets monotonally smaller while increasing the potential on the electrode E2, limited at 430 V for the previous CU, therefore suggesting an improvement in the beam focusing with higher voltages availability.
Building a new control CU also allows to improve the easiness of use of the present system, passing from an analogic control to a digital one, software controlled.
Therefore, the requirements for a control unit (CU), taken into account during the design process, are: (i) stable output voltages, (ii) extended voltage range, (iii) possibility to read the current on the electrodes and (iv) easiness of use.

5.1. Structure of the control unit

The control unit is digitally controlled via computer through a USB port. Two power generators are needed at the input in order to provide the maximum value for the output voltage: one at 700 V is used for the electrodes requiring particularly high voltages, a second one at 500 V used for all the other electrodes.
The unit was realized with discrete components, accounting for a total cost of $\sim$ 1400€ including the cost of 2 high voltage supplies ($\sim$ 500€ each), to be compared with industrial high voltage generators costing $\sim$ 500€ each (thus leading to a minimum cost of the unit of $7 \cdot 500€ = 3500€$, to which additional rack components needs to be added, e.g. case, switches, connectors, wires, etc ...).
The CU working principle is depicted in figure 5.2a and can be divided in five blocks:

- *Matlab interface.* A Matlab-designed app is used in order to set the electrodes voltages and to read the corresponding currents.

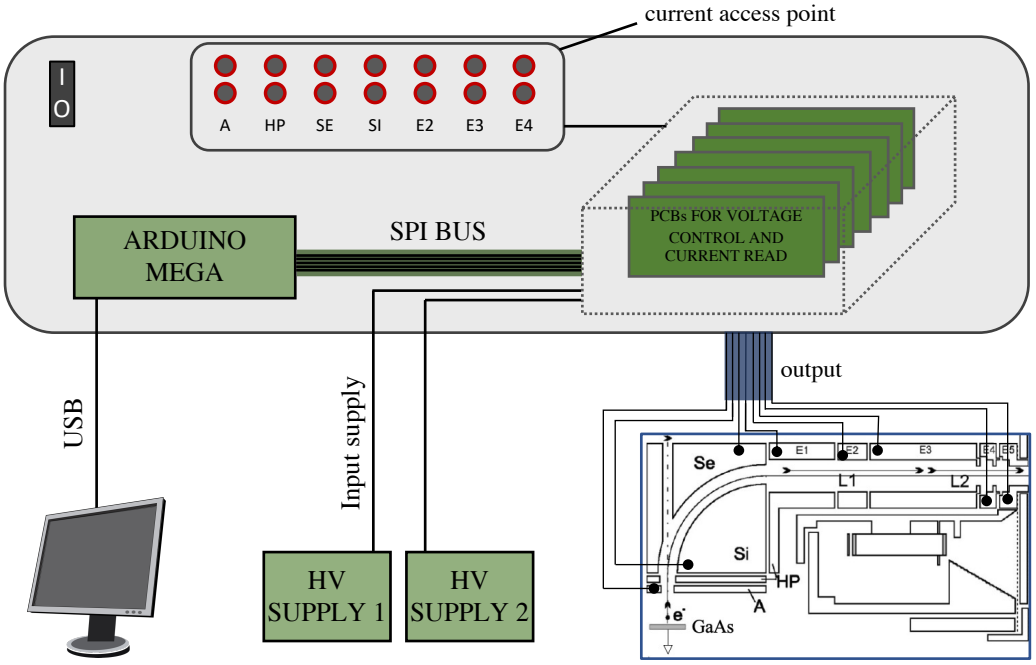

(a)

(b)

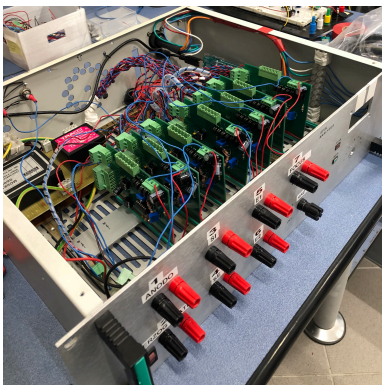

(c)

Figure 5.2: (a) Schematic of the control unit for the electron gun. The unit is controlled by a software interface and receives a constant High Voltage (HV, 700 V) from an external supply. The digital signal is converted in the control unit and set at the electrodes of the electron gun. The current sensed at the electrodes is also acquired by the internal circuitry with a floating ammeter. (b) Rack configuration of the CU, with the two Ortec power supplies mounted beneath. (c) Inside view of the CU.

- *Arduino Mega.* It is used as microcontroller (μC) for the CU in order to control the digital communication with the seven different electrodes-dedicated PCBs.
- *Electrode Voltage control.* For every electrode, a PCB is used to control the output voltage taking as input the fixed high voltage (700 V) and the reference value from the μC (0 - 700 V).
- *Electrode Current reading.* For every electrode, a second PCB connected to the previous one is used as floating micro-ammeter ($\sim \mu$A) to sense the current. The digital signal is then sent to μC through a digital communication isolator.
- *Electronde Current reading by shunt resistance.* The current can also be read by measuring the voltage drop across the shunt resistances present at the "current access point".

For what concerns the software, the Arduino script is presented in the appendix A, together with the preview of the software interface and some useful tables for troubleshooting (command table and error messages table).

5.2. Design of the circuits

The circuit design for the *voltage control* PCBs started from an analog circuit presented in [33, 85], where it was used for similar purposes to ours (analogically-controlled high-voltage supply for acceleration of an ion beam in a sputtering gun). Its characterization, by previous authors, showed a good stability of the output voltage ($\leq 0.5\%$) after 30 min warm-up and ripple of less than 300 mV for output $V_{out} = 2$ kV, therefore well above the voltages used in the considered case (presented in section 5.3).
The upgrades introduced by the author regard the additional digital control and the development of the *current read* circuit, added *ex-novo* in order to solve the issue of current detection on the electrodes. The full list of components used in the project is reported in appendix B, while the circuit characteristic are presented in the following.

5.2.1. Voltage control PCB

The analog circuit for the voltage control is a voltage amplifier which takes a reference voltage V_{ref}, in the 0-5 V range, at the input and multiplies it through a feedback loop. The circuit schematic is shown in figure 5.3a, while the PCB design in figure 5.4a. The maximum output is set by the arbitrary supplied High Voltage (VCC in figure 5.3a) provided by the external HV power supplies. In order to control the circuit from the μC, a 12-bit Digital to Analog Converter (DAC) is used to set the V_{ref}, whose value is checked

by the μC through a 12-bit Analog to Digital Converter (ADC). The digital to analog (and viceversa) conversion section is highlighted in a blue dashed line in the schematic. DAC and ADC communicate with the μC through an SPI bus made of three shared lines (SCLK, MISO, MOSI) plus individual chip select (CS) lines to select every device (either a DAC or an ADC).
The output voltage is obtained by the simple resistance partition:

$$V_{out} = \frac{R_1 + R_2}{R_2} V_{ref} \simeq \frac{R_1}{R_2} V_{ref} \tag{5.1}$$

being usually $R_1 \ll R_2$. The gain can be tuned by varying the value of R_2 during the testing phase and used values are $G \simeq R_1/R_2 = 100 \sim 200$.
The optocouplers role is to isolate the low-voltage side from the high-voltage one (as separated by the orange line in figure 5.3a), while limiting the current flowing from HV to V_{out}. As a matter of fact, this current control is essential to limit the output value:

$$V_{out} = I_{opto} \cdot (R_1 + R_2) \tag{5.2}$$

The number of optocouplers is set by the choice of HV, considering that their breakdown collector-emitter voltage is limited to $\sim 100\,\mathrm{V}$ and more of them in series are needed to avoid their breaking. For example, considering a worst case scenario of $V_{HV} = 500$ V and $V_{out} = 0$, all the voltage drop falls on the optocoupler series, so that the safety requirement for the system is:

$$V_{tot,breakdown} = N \cdot V_{breakdown} < V_{HV} \tag{5.3}$$

In the used setup, being $V_{breakdown} = 100\,\mathrm{V}$, we used 7 optocouplers.

5.2.2. Current read PCB

The values of current flowing at the electrodes, as mentioned above, give information on the position of the electron beam. The typical electron beam current in the experiments is $10\,\mu$A, so that the PCB, whose schematic is shown in figure 5.3b, needs to sense $I_e = 0 - 10\,\mu$A (in the worst case scenario all electrons are adsorbed by one electrode, therefore setting the maximum current that the circuit is able to read). In order to do so, a shunt resistor $R_s = 10\,\mathrm{k}\Omega$ is inserted in series with the output of the voltage control PCB, leading to $\Delta V_{out,max} = 100\,\mathrm{mV}$. The voltage drop across R_s is amplified by a non-inverting amplifier with gain G = 30 (highlighted by the blue dashed contour in figure 5.3b)and fed into a 12 bit ADC with input range 0-4.096 V, thus obtaining a least significant bit

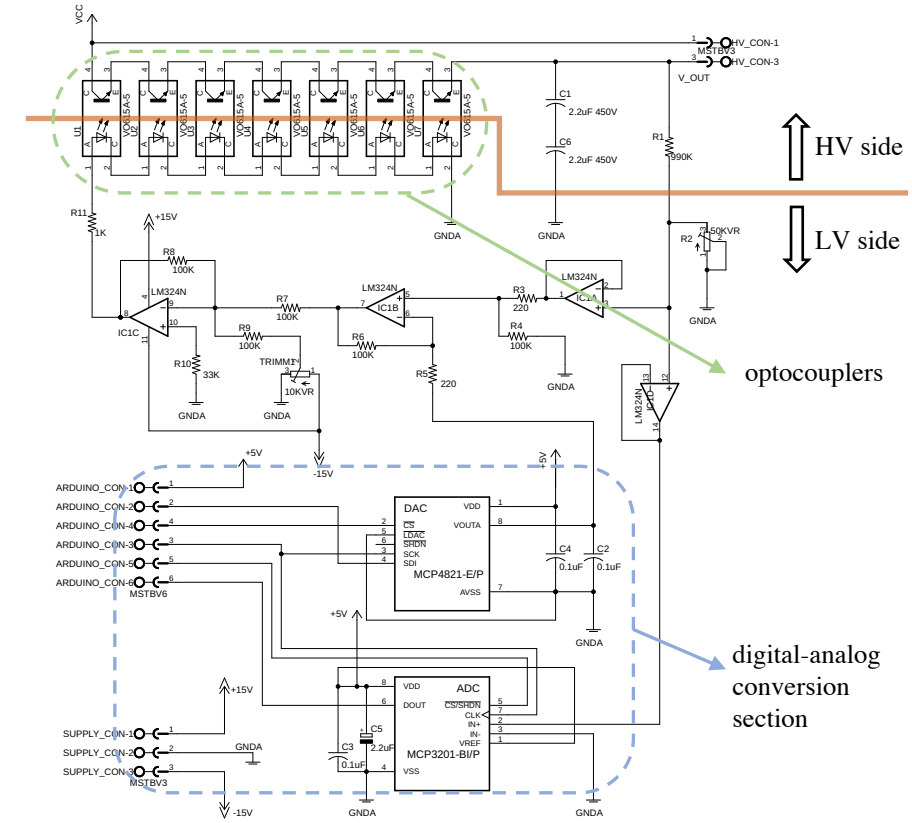

(a)

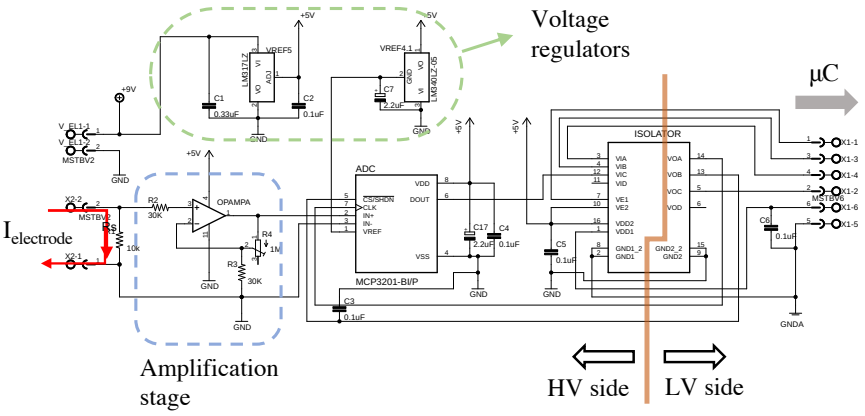

(b)

Figure 5.3: (a) Schematic for the *voltage control* PCB while (b) the schematic for the *current read* PCB. Inputs of the PCBs are set on the left side, while the output on the left. The signal GNDA in the two schematic is shared and stands for the ground value of the system, while GND signal in (b) is the floating ground plane, set at the output voltage V_{out}. The orange lines in both cases separate the High Voltage (HV) side from the Low Voltage (LV) side. The components names are labeled in figure and the main building blocks are also highlighted by the colored dashed lines.

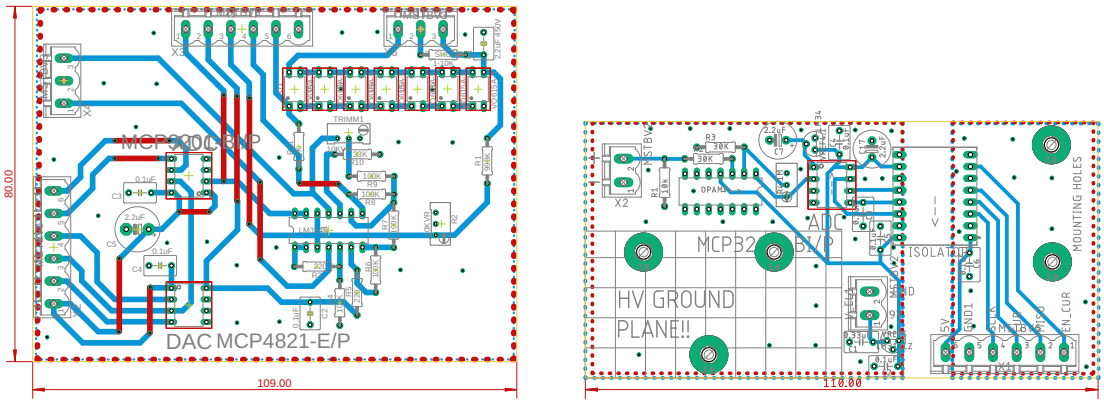

(a) (b)

Figure 5.4: PCB designs for the *voltage control* (a) and *current read* (b) boards, realized with a 2-layer structure. The reported dimensions are expressed in mm.

(LSB) value of $\sim 3\,\text{nA}$. A section of the circuit (left side in figure, or "HV side") has the requirement of being floating, due to the current measurement taking place at the variable voltage V_{out}, so that a 9V battery is used as power supply, coupled with voltage regulators at 5V and 4.096 V for the supplies of the integrated components.
The ADC digital output signal passes from the floating part of the circuit to the real ground side (and to the μC) thanks to a low-power triple-channel digital isolator: this component allows to isolate two circuit sides up to $2500\,V_{RMS}$ while transferring the digital signal referred to the respective ground levels and supplies of the two sides.
Considering for example an electron current of $I_{el} = 2\,\mu\text{A}$ flowing into R_s, the voltage drop would be $V_s = I_{el} \cdot R_s = 20\,\text{mV}$, therefore negligible for the stability requirements of the electrode voltage. This voltage drop is amplified by G = 30 and fed into the ADC, $V_{in,ADC} = 600\,\text{mV}$. The output digital signal is sent across the digital isolator and received by the μC.

5.3. Performances characterization

The test procedure for the control unit consisted in a first part of benchmarking in which the PCBs were tested from the point of view of output stability, communication stability with the μC and single components performances. The gain coefficients were manually tuned by mean of a trimmer and the software interface opportunely tested. A second part was instead dedicated to the electron gun performances evaluation.

5.3.1. PCBs benchmarking

For what concerns the benchmarking of *voltage control*, the output voltage stability has been analysed through an oscilloscope, showing a quite high time constant for the V_{out}, $t = RC \simeq 1\,s$, due to the high output capacitance $C_{out} = 1.1\,\mu F$. This limits the discharge time of electrodes, but it also reduces the output ripple, which wasn't observed to be measurable with the used instrumentation. The low ripple is also obtained thanks to the high stability of the used HV supply (Ortec 556 high-voltage power supply), thus the circuit was proved to not add any contribution on it.
The stability of the output was also tested and it was observed a drift $\sim 0.3\%$ in the first 10/15 minutes after setting V_{out}. This phenomenon was attributed to the thermal stabilization of the circuit: the Temperature Coefficient of Resistance (TCR) in R_1 has a strong influence on the output gain, thus causing a drift during warm-up, dependent on the current flowing I_{opto} (equation (5.2)). After 30 minutes no more evident drift was observed, with a resolution of 0.03 % (e.g. 100 mV over 300 V output).
Therefore, some minutes wait is needed when significantly changing the electrode voltage, while this is not necessary for small voltage variations (e.g. < 20 V).
For the *current read* PCBs, two tests were performed: (i) test of the correctness of the digital transmission and stability of the read values and (ii) test for the quality of isolation of the two sides of the board. Both tests were considered successful and the few errors in digital transmission are compensated by the software oversampling.

5.3.2. Overall performance of the control unit

Once integrated in the LASSE setup, the performances of the electron gun were tested from the point of view of the total transmission and size of the electron beam. In order to do so, the electron gun was used in the configuration with grounded photocathode and positive V_s applied to the manipulator, which was located at the output aperture of the electron gun, as shown in figure 5.5.
To measure the total transmission, a varying voltage V_s was applied to the manipulator and the total current of electrons striking on it was measured.
To characterize the beam size, we used the Faraday cup located on the sample holder, with entrance diameter of 0.5 mm, set at a fixed voltage of 28 V while varying the manipulator voltage V_s between 10 and 20 V. The electron beam's shape was characterized along two perpendicular axes, keeping a fixed distance between the Faraday cup and the electron gun's output of $x = 10$ mm and calibrating the manipulator angle in order to have the

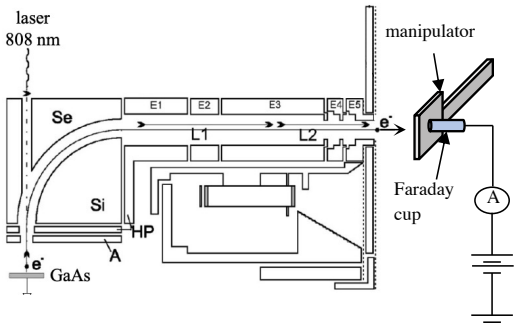

Figure 5.5: Setup for the beam size and transmission characterization. The Faraday cup located on the manipulator is set at 28 V by a battery, while the current absorbed is measured by an ammeter inserted in series.

Name	Acronym	voltage [V]
Photocathode	PC	0
Anode	A	230
Herzog plates	HP	305
Internal sphere	SI	355.4
External sphere	SE	233.8
Electrode 2	E2	505
Electrode 3	E3	83
Focus	F	50
Retina	E5	10
Faraday cup	FC	28

Table 5.1: Electron gun's electrodes potentials used for the setup characterization.

Faraday cup entrance aligned with the beam direction.

The reference quantities for these tests were the ones from [16], also presented in figure 3.20a, showing a minimum spot size of $\sim$ 1 mm and a transmission of $\sim$ 70% at $V_s > 12$V. It was noticed that the voltages needed for a good beam propagation depends on the position and orientation of the photocathode, therefore they may be slightly different in future experiments[1]. The used electrodes potentials are reported in table 5.1. During the characterization process, at different V_s, the voltage for the focus was slightly changed, within 48 and 53 V, in order to maximize the central spot intensity (higher values of focus were used for lower V_s).

Looking at figure 5.6a, it is possible to note that the renewed setup brought an improvement on the spot size, passing from a best spot size of 1 mm with the previous control unit to 0.5 mm with the new one. For what concerns the total transmission at variable

[1]This issue mainly affect the electrodes SI and SE, which are more sensitive to small variations.

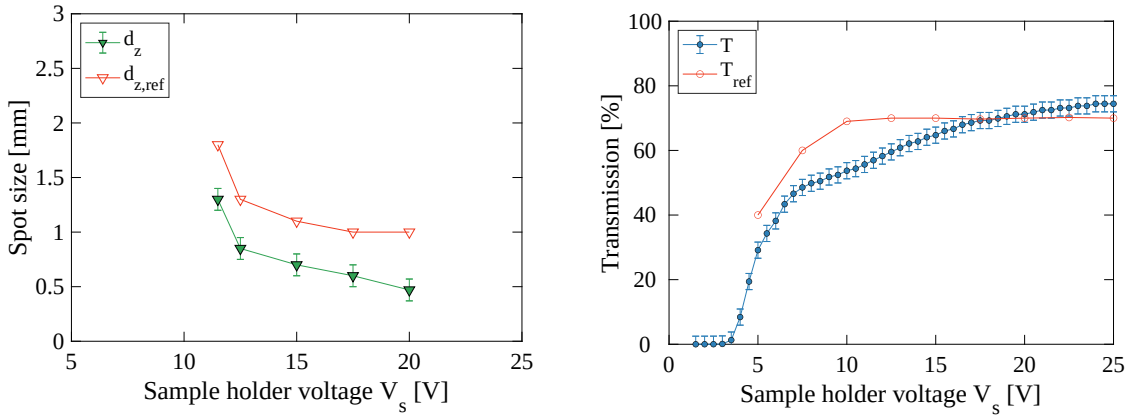

(a) (b)

Figure 5.6: Characterization of the electron beam with the new control unit and laser ($\lambda = 808\,nm$) in comparison with the values stated in [16]. (a) Comparison of the spot size, while (b) is the comparison of the overall transmission.

V_s, presented in figure 5.6b, an improvement has been obtained at $V_s > 17\,\mathrm{V}$, while a performance worsening was obtained at lower potentials. The aim is to improve this last result by exploiting a different set of voltages used for the electrodes. On this point, investigation is still in progress.

5.4. Discussion of the results and further improvements

These preliminary results on the characterization of the control unit prove its correct working functionality. Some considerations can be done recalling the fundamental requirements introduced at the beginning of the chapter: stability of the output, extended voltage range, current reading possibility, easiness of use.

The stability of the CU output voltages has been proved to be satisfying for the requirement of a stable electron beam current on the sample manipulator. The presence of a drift during warm up makes the stability of the CU slightly worse than the one of an industrial power supply, which presents internal compensation circuits, but nevertheless satisfying for the purpose of this application.

The increased voltage range for the electrodes, from 0-430 V to 0-700 V, allows for stronger electric fields inside the system and for a smaller spot size of the beam (since before it was limited by the potential of electrode E_2, set at the maximum available voltage, which can now be raised up to its optimal value of 505 V).

The possibility of reading the electron currents absorbed by the electrodes through an

internal floating circuit constitutes an extremely safe way to monitor the beam deflection correctness. Furthermore, these currents (7 electrodes) can be now acquired in parallel, allowing for a much easier and faster interpretation of the measured values.
The easiness of use is guaranteed by the software interface, that allows to set the electrode voltages, thus making the calibration process repeatable, and to read the electron currents absorbed by them, thus allowing for a more rapid tuning of the calibration. The digital control represents a strong improvement with respect to the previous analogical unit from the point of view both of repeatability of the experiments.
Overall, the tests performed on the CU showed how the low cost component CU (cost $\leq$ 1500€) can be used for an electron gun system, with satisfying results, instead of a more complex and costly CU made by independent high-voltage power supply modules (rough cost estimate $\sim$ 4000€).
The improvement in performances opens the way to new experiments of electron transmission, exploiting the smaller spot size obtained. The electron beam presents a spin polarization, obtained by using circularly polarized light on the GaAs photocathode, and experiments on the polarization using a Fe-p(1x1)O target confirmed the correct behaviour of the system.

6 | Conclusions

The overall result of this thesis concerns the two distinct but related topics of $Ge_xSn_{1-x}Te$ (GST) characterization and instrumental-tool improvement. GST belongs to the FERSC family and is a promising material for spin-to-charge conversion (SCC).

The growth and characterisation of $Ge_xSn_{1-x}Te$ presented in **chapter 4** allowed to investigate an intermediate region between two already known materials, namely GeTe and SnTe, looking for a combination of them that would mix and engineer their band structure, in particular combining the Rashba (GeTe) and topological (SnTe) characters.

It was demonstrated that the Ge doping is beneficial for the stabilization of the ferroelectric phase of SnTe, otherwise requiring T<100 K. This phase was proved to resist up to room temperature, as verified by the current-voltages measurements of ferroelectricity and by the presence of Rashba bands in the ARPES spectra from T=77 K up to T=320 K (in the FERSC class of materials, both Rashba bands and ferroelectricity originate from the structural distortion, so that they are coupled).

The novel doping technique adopted, consisting in an annealing-driven interdiffusion from of Ge atoms from the GeTe underlayer, provides an innovative method to both induce the ferroelectric phase in the overlayer (by dipolar interaction with the out-of-plane polarization of GeTe) and dope it with Ge atoms.

The ARPES and S-ARPES analysis allowed to confirm the spin-momentum locking of Rashba bands in the investigated samples. Furthermore, the analysis provided evidence for the modulation of the giant Rashba splitting with the different concentrations of germanium. The experimental results showed the increase of the Rashba wave-vector k_r with the increase in Ge doping x, from $k_r = 5\text{Å}^{-1}$ at $x \simeq 30\%$ to $k_r = 11\text{Å}^{-1}$ at $x = 100\%$ (pure GeTe). The same trend was confirmed by independent DFT calculations for the Rashba wave-vector k_r as a function of the Ge doping (figure 4.14a), thus supporting the experimental results.

The interest for FERSC materials characterization by SCC experiments inspired the development of a new experimental tool. This exploits a spin-polarized electron beam for spin-injection in the material, while measuring the current flowing due to SCC. In order to do so, better performances for the existing electron gun setup, corresponding to smaller

spot size and easiness of use, were required and so implemented in this work. Other issues with this measurement technique are still under investigation, e.g. the implementation of contact electrodes in the vacuum system, and are not discussed in the present work.
The development of the new control unit for the electron gun electrodes was presented in **chapter 5**. This CU is controlled via software and has the role of setting the voltages of the electron gun's electrodes, while acquiring the current flowing at these electrodes (current reading performed with a floating dedicated circuit).
The performed tests provided satisfying results in terms of the easiness of use, stability of the voltage outputs and the shape of the output electron beam, which was reduced in spot size by 50% with respect to the previous setup (from 1 mm to 0.5 mm).
The solution developed in this work constitutes an extremely economic alternative to the use of seven independent industrial high-voltage power supplies, allowing to split the two input high-voltage power supplies towards multiple output channels independently controlled.

The perspective of this work are several. The ARPES experimental data obtained so far are in agreement with DFT calculations over the region investigated ($x > 30\,\%$). This set the foundation for new studies investigating the lower Ge concentration region (e.g. $x < 20\,\%$), expecting similar experimental confirmation. This region is expected to show both Rashba states originating from the lattice distortion and the topological conducting surface states typical of SnTe, combined to a smaller bandgap which could result in interesting outcomes for the transport properties of these materials.
For what concerns the perspectives on electron gun's applications, the electron beam could be used to test the novel technique of spin-injection in vacuum, representing the final aim of the improvements carried out. This kind of measurement would be of paramount importance for the spin-charge characterization in spintronic materials, allowing to investigate their conversion efficiency without the indirect spin-injection processes through ferromagnetic layers (which introduces spurious effects and interface issues).

A | Script appendix

The Arduino code consists in a set of variables which are shared with the Matlab interface app. This app has the only function to update its variables values by getting them from arduino, while it can also set the output voltages at the arduino. The ramp function and all the data reading procedures (from PCBs) are performed by the μC. In this appendix the Arduino code (C++) is first reported, followed by the preview of the software interface and of the trouble-shooting table.

A.1. Arduino code

```
/*copyright Federico B.
  last update 22/02/2022
 sketch to allow communication from Matlab to Arduino through Serial port
 Matlab sends voltage values that Arduino write to the DAC.
 Arduino reads the ADC values and send them back to Matlab
*/

#include <MCP_DAC.h>
#include <SPI.h>
#include <String.h>
// Pin connections.
#define SCLK         52    // connected to ADC pin 7 and DAC pin 3
#define MISO         50    // connected to ADC pin 6
#define MOSI         51    // connected to DAC pin 4

// being "Device" from 1->8:
#define DAC 19      // so DACs are DAC+3*Device-->[22,25,28,31,34,37,40,43]
#define ADC 20      //    ADC are ADC+3*Device-->[23,26,29,32,35,38,41,44]
#define CUR 21      //    CUR are CUR+3*Device-->[24,27,30,33,36,39,42,45]
#define EN_CUR 22   // EN_CUR are CUR-Device-->  [21,20,19,18,17,16,15,14]

//properties vectors 9 elements
int      MaxDevices=7;
float    VoutMAX[MaxDevices]= {300,300,300,300,300,300,300};
float    VoutSetpoint[MaxDevices]= {0,0,0,0,0,0,0};   //setpoint to be reached
float    VoutActual[MaxDevices]= {0,0,0,0,0,0,0};     //Actual value fed at the DAC
float    VoutRead[MaxDevices]= {0,0,0,0,0,0,0};       //value read and converted from ADC
float    G1[MaxDevices]= {100,100,150,150,150,100,100};     // gain on DAC
float    G2[MaxDevices]= {124,123,185.5,184,186.5,124,124}; // gain on ADC
float    G3[MaxDevices]= {1,1,1,1,1,1,1};                   // gain on CUR
int      SamplesPerReading[MaxDevices]= {5,5,5,5,5,5,5};
float    RampRate[MaxDevices]= {5,5,5,5,5,5,5};    //ramprate set in V/s
boolean  verbouse=LOW;
float    CurrentRead[MaxDevices]= {0,0,0,0,0,0,0};  //I_read values

//operative variables
byte ReturnedByte1 =0x00;
byte ReturnedByte2 =0x00;
int      Device=0;                 // index to acces the HV desired 1->9
boolean  Set=LOW;                  //LOW to get values, HIGH to set
int      Input=0;                  //value in mV read from ADC
String   Command="EMPTY";          //acquisition from serial Code
```

```
String   CommandValue="EMPTY";      //acquisition from serial Value
String   CommandDevice="EMPTY";     //acquisition from serial Device
boolean  CommandSuccess=LOW;
float    Delta=0;
float    Step=1;
long int t1[9];     //ramp managment
long int t2[9];
long int t3;        //update output values management
long int t4;
int      ii=1;
int      jj=1;
float    Value=0;

boolean newData = false;
const byte numChars = 32;    // limit to char acquisition on single command
char receivedChars[numChars];
char endMarker = '\n';

void setup() {
  Serial.begin(115200);
  //Serial.println(__FILE__);
for (ii=1;ii<(MaxDevices+1);ii++){// all pins from 22 to 48 are Chip Select
    pinMode(DAC+(3*ii), OUTPUT);
    pinMode(ADC+(3*ii), OUTPUT);
    pinMode(CUR+(3*ii), OUTPUT);
    pinMode(EN_CUR-ii,OUTPUT);
    digitalWrite(DAC+(3*ii), HIGH);
    digitalWrite(ADC+(3*ii), HIGH);
    digitalWrite(CUR+(3*ii), HIGH);
    digitalWrite(EN_CUR-ii, LOW);
    if (verbouse){
      Serial.print("HV");
      Serial.print(ii);
      Serial.println("␣activated");
    }
}
  SPI.begin();
  delay(10);
  for (ii=1;ii<(MaxDevices+1);ii++){
    DACwrite(DAC+(3*ii),0,0);
    t1[ii-1]=millis();
    t2[ii-1]=t1[ii-1];
  }
  t3=millis();
}

void loop (){
  if (Serial.available()>0){
    // requires a message in the form "ABC:1234" or "ABC?"
    Command= recvWithEndMarker();

    if (newData){           //full message received
      if (Command.substring(3,4)==":"){
        CommandValue=Command.substring(4); //takes from index 4 to the end
        Set=HIGH;
        CommandSuccess=HIGH;
      }else if(Command.substring(3,4)=="?"){
        Set=LOW;
        CommandSuccess=HIGH;
      }else{
        Serial.println("INCORRECT_FORMAT");
        CommandSuccess=LOW;
      }
      if(CommandSuccess){
        CommandDevice=Command.substring(2,3); //takes the index 3
        Device=CommandDevice.toFloat();
        if (verbouse){
          Serial.print("device␣selected->");
          Serial.println(Device);
        }

        Command.remove(2); // Command only contains the "AB" commands
        if(Device==0){
          //test mode, do the desired controls here
          if (Command.compareTo("CN")==0){ //connection check
            if (verbouse){
```

```
119             Serial.println("11");
120           }else{
121             Serial.println("10␣");
122           }
123         }else if(Command.compareTo("VR")==0){
124           verbouse=1-verbouse;
125           Serial.println(verbouse);
126         }
127       }else{
128         if (Command.compareTo("GP") == 0) { // get the set parameters
129           Serial.println(G1[Device-1],2);
130           Serial.println(G2[Device-1],2);
131           Serial.println(SamplesPerReading[Device-1]);
132           Serial.println(RampRate[Device-1]);
133           Serial.println(VoutMAX[Device-1]);
134           Serial.println(VoutSetpoint[Device-1]);
135
136         }else if (Command.compareTo("GS") == 0) { // Get state, composed by AV,SP,RV
137           if(Set){ //Set==HIGH, error
138             Serial.println("GS_SET_ERROR");
139           }else{   //Set==LOW, get the actual values
140             Serial.println(VoutActual[Device-1]);
141             Serial.println(VoutSetpoint[Device-1]);
142             Serial.println(VoutRead[Device-1]);
143             Serial.println(CurrentRead[Device-1]);
144           }
145
146         }else if (Command.compareTo("SP") == 0) { // Setpoint
147           if(Set){                              //set the new value
148             Value=CommandValue.toFloat();
149             if(Value<VoutMAX[Device-1]){
150               VoutSetpoint[Device-1]=Value;
151               Serial.println(VoutSetpoint[Device-1]);
152             }else{
153               VoutSetpoint[Device-1]=VoutMAX[Device-1];
154               Serial.println("LIMIT_REACHED");
155             }
156           }else{                              // get value
157             Serial.println(VoutSetpoint[Device-1]);
158           }
159
160         }else if (Command.compareTo("RR") == 0) { // RampRate
161           if(Set){                              //set the new value
162             RampRate[Device-1]=CommandValue.toFloat();
163             Serial.println(RampRate[Device-1]);
164           }else{                              // get value
165             Serial.println(RampRate[Device-1]);
166           }
167
168         }else if (Command.compareTo("G1") == 0) { // G1
169           if(Set){ //Set==HIGH, so we set the new value
170             G1[Device-1]=CommandValue.toFloat();
171             Serial.println(G1[Device-1]);
172           }else{                              // get value
173             Serial.println(G1[Device-1]);
174           }
175
176         }else if (Command.compareTo("G2") == 0) { // G2
177           if(Set){                              //set the new value
178             G2[Device-1]=CommandValue.toFloat();
179             Serial.println(G2[Device-1]);
180           }else{                              // get value
181             Serial.println(G2[Device-1]);
182           }
183
184         }else if (Command.compareTo("SR") == 0) { // SamplesPerReading
185           if(Set){                              //set the new value
186             SamplesPerReading[Device-1]=CommandValue.toFloat();
187             Serial.println(SamplesPerReading[Device-1]);
188           }else{                              // get value
189             Serial.println(SamplesPerReading[Device-1]);
190           }
191
192         }else if (Command.compareTo("AV") == 0) { // VoutActual
193           if(Set){                            //Set==HIGH,ERROR
194             Serial.println("AV_SET_ERROR");
```

```
195             }else{                              // get value
196               Serial.println(VoutActual[Device-1]);
197             }
198
199           }else if (Command.compareTo("RV") == 0) { // VoutRead
200             if(Set){                            //Set==HIGH, ERROR
201               Serial.println("RV_SET_ERROR");
202             }else{                              // get value
203               Serial.println(VoutRead[Device-1]);
204             }
205
206           }else if (Command.compareTo("VM") == 0) { // VoutMAX
207             if(Set){                            //set the new value
208               VoutMAX[Device-1]=CommandValue.toFloat();
209               Serial.println(VoutMAX[Device-1]);
210             }else{                              // get value
211               Serial.println(VoutMAX[Device-1]);
212             }
213
214           }else if (Command.compareTo("AC") == 0) { //ActualCurrent
215             if(Set){                            //Set==HIGH, ERROR
216               Serial.println("SET_CURRENT_ERROR");
217             }else{                              // get value
218               digitalWrite(EN_CUR-Device, HIGH);
219               delay(100);
220               CurrentRead[Device-1]=readMultiple(CUR+(3*Device),G3[Device-1],SamplesPerReading[Device-1]);
221               digitalWrite(EN_CUR-Device, LOW);
222             }
223           }else{
224             Serial.println("INVALID_COMMAND");
225           }
226
227         }
228       }
229       Command="EMPTY"; CommandValue="EMPTY"; CommandDevice="EMPTY";
230       CommandSuccess=LOW; Set=LOW; newData=false;
231     }
232   }
233
234   //ramp:
235   //update the value in the ramp if needed differently.
236   for (Device=1;Device<MaxDevices+1;Device++){
237     t2[Device-1]=millis();
238     if(VoutActual[Device-1]!=VoutSetpoint[Device-1]&&(t2[Device-1]-t1[Device-1])>(1000/RampRate[Device-1])){
239       Delta=VoutSetpoint[Device-1]-VoutActual[Device-1];
240       if(Delta>0){
241         Step=1;
242         if(Delta<Step){
243           VoutActual[Device-1]=VoutSetpoint[Device-1];
244         }else{
245           VoutActual[Device-1]=VoutActual[Device-1]+Step;
246         }
247       }else{
248         Step=-1;
249         if(Delta>Step){
250           VoutActual[Device-1]=VoutSetpoint[Device-1];
251         }else{
252           VoutActual[Device-1]=VoutActual[Device-1]+Step;
253         }
254       }
255       DACwrite(DAC+(3*Device),G1[Device-1],VoutActual[Device-1]);
256       delay(10);
257       VoutRead[Device-1]=readMultiple(ADC+(3*Device),G2[Device-1],SamplesPerReading[Device-1]);
258       digitalWrite(EN_CUR-Device, HIGH);
259       delay(5);
260       CurrentRead[Device-1]=readMultiple(CUR+(3*Device),G3[Device-1],SamplesPerReading[Device-1]);
261       digitalWrite(EN_CUR-Device, LOW);
262       t1[Device-1]=t2[Device-1];
263     }
264   }
265
266   t4=millis(); // refresh output values once every 1.5s
267   if (t4-t3>200){
268     if(jj==(MaxDevices+1)){
269      jj=1;
270     }else if (jj>(MaxDevices+1)||jj<1){
```

```
     Serial.println("ERROR_REFRESH");
    }else{
      DACwrite(DAC+(3*jj),G1[jj-1],VoutActual[jj-1]);
      VoutRead[jj-1]=readMultiple(ADC+(3*jj),G2[jj-1],SamplesPerReading[jj-1]);
      digitalWrite(EN_CUR-jj, HIGH);
      delay(5);
      CurrentRead[jj-1]=readMultiple((CUR+(3*jj)),G3[jj-1],SamplesPerReading[jj-1]);
      digitalWrite(EN_CUR-jj, LOW);
      jj=jj+1;
    }
    t3=t4;
  }}


/************************************************
                FUNCTIONS
 ************************************************
*/
String recvWithEndMarker() {
    static byte ndx = 0;
    //char endMarker = '\n';
    char rc;
    while (Serial.available() > 0 && newData == false) {
        rc = Serial.read();
        if (rc != endMarker) {
            receivedChars[ndx] = rc;
            ndx++;
            if (ndx >= numChars) {
                ndx = numChars - 1;
            }
        }
        else {
            receivedChars[ndx] = '\0'; // terminate the string
            ndx = 0;
            newData = true;
        }
    }
    String output=String(receivedChars);
    return output;
}

/*********************************************************************/

void DACwrite(int DAC_CS_PIN, float G1,float Vout) {
  float mVDAC=Vout*1000/G1;
  uint16_t value=(uint16_t) mVDAC;   // convert to mV (from V)
  uint16_t data = 0x1000 | value; // gain=2-> [0:4096]->[0:4096] gain=1-> [0:4096]->[0:2048]

  digitalWrite(DAC_CS_PIN, LOW);
  SPI.beginTransaction(SPISettings(5000000, MSBFIRST, SPI_MODE0));
  SPI.transfer((uint8_t)(data >> 8));
  SPI.transfer((uint8_t)(data & 0xFF));
  SPI.endTransaction();
  digitalWrite(DAC_CS_PIN, HIGH);
}

/*********************************************************************/

float readMultiple(int ADC_CS_PIN, float G2, int numOfReadings){
   float Vread=0;
   int Input=0;
   int ii=0;
   for(ii=0 ; ii<numOfReadings ; ii++){
     if (ii==0){
       Input= Input+ (int)ADCread(ADC_CS_PIN,HIGH);
     }else{
       Input= Input+ (int)ADCread(ADC_CS_PIN,LOW);
     }
     delay(1);
   }
   Vread=Input;
   Vread=Vread/numOfReadings;
   Vread=Vread*G2;
   Vread=Vread/1000;     //conversion from mV to V
   return Vread;
}
```

```
347
348 /*****************************************************************/
349
350 uint16_t ADCread(int ADC_CS_PIN, boolean FirstRead) {
351   uint16_t result;
352   int output;
353   digitalWrite(ADC_CS_PIN,LOW);
354
355   SPI.beginTransaction(SPISettings(100000, MSBFIRST, SPI_MODE3));
356   byte returnedByte1 = SPI.transfer(0); // first byte, with LSBs
357   byte returnedByte2 = SPI.transfer(0); // second byte, has LSB in the 7MSB
358   SPI.endTransaction();
359   digitalWrite(ADC_CS_PIN,HIGH);
360    result=returnedByte1;     // composition of the two bytes:
361    result=result<<8;
362    result=result|returnedByte2;
363    if (FirstRead){
364    result=result>>2;
365    }else{
366    result=result>>1;
367    }
368    result=result & 0x0FFF;  // cuts the 4 MSB
369    return result;
370 }
```

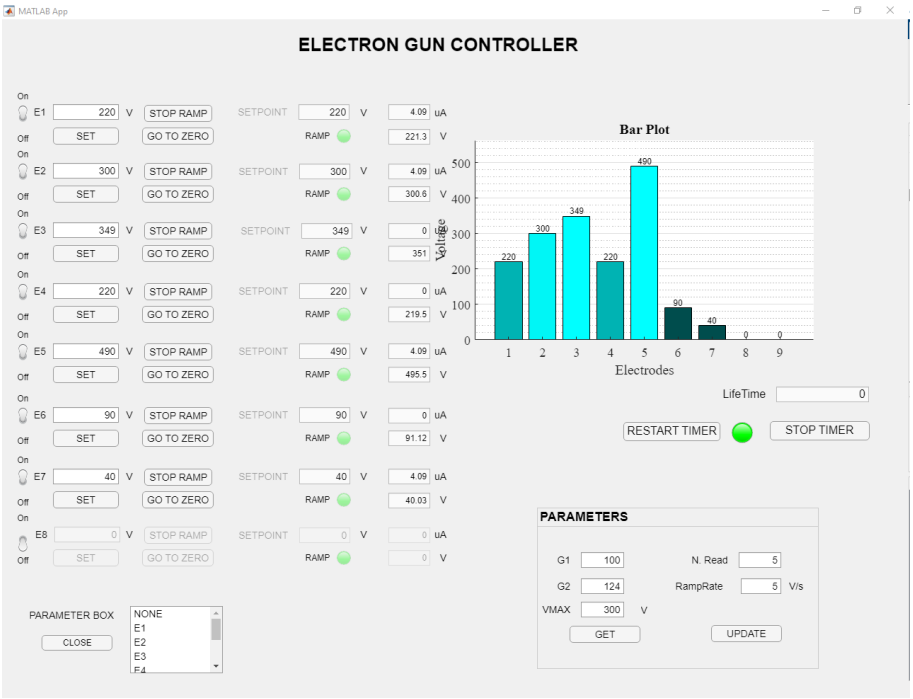

Figure A.1: Overview of the software interface. E1-E7 electrodes voltages can be set using the left boxes, while the current and voltage values acquired are showed in the central column. The figure bar plot shows the potentials set at the electrodes. The *parameters box* shows parameters relative to the selected electrode.

A.2. List of commands and errors

Name	Description	Electrodes	Set/Get
GP	get working parameters (G1,G2,SR,RR,VM,SP)	1 - 7	get
GS	gets actual state (SP,AV,RV,AC)	1 - 7	get
SP	set/get SetPoint	1 - 7	get/set
RR	set/get RampRate	1 - 7	get/set
G1	set/get G1 of DAC writings	1 - 7	get/set
G2	set/get G2 of ADC readings	1 - 7	get/set
G3	set/get G3 of CUR readings	1 - 7	get/set
SR	set/get SamplesPerReading	1 - 7	get/set
AV	get the output voltage at DAC	1 - 7	get
RV	get the read voltage at ADC	1 - 7	get
VM	set/get VoutMAX	1 - 7	get/set
AC	get actual current for device set	1 - 7	get
CN	check connection	0	get
VR	change verbouse state	0	set

Table A.1: List of commands allowed by the μC.

Message	Description
INCORRECT_FORMAT	The command received is not in the form "XYD:1234" or "XYD?"
GS_SET_ERROR	Set option not allowed for the Get State command
LIMIT_REACHED	Maximum value allowed for Sepoint reached
AV_SET_ERROR	Set option not allowed for the Actual Voltage command
RV_SET_ERROR	Set option not allowed for the Read Voltage command
AC_SET_ERROR	Set option not allowed for the Actual Current command
INVALID_COMMAND	The command received is not supported
ERROR_REFRESH	Indexing error during the outputs refresh

Table A.2: List of errors that μC may send to the computer.

B | List of Components for electron gun's control unit

In this appendix, the list of all components used in order to build the control unit are presented. The number of components of table B.2 and table B.3 are referred to the single PCB, while 8 of each were realized. The components present in table B.1 are instead necessary for the rack box assembly or are shared by all the control unit. All components were supplied by RS components and the components can be searched on the website by copying the *order code* from the tables.

Part	Quantity	Designator	Supplier	Order-code	Part number
microcontroller	1	arduino		715-4084	A000067
PCB holder	10	guide	RS PRO	500-550	952-223616
connector	7	terminal black	RS PRO	423-201	423-201
connector	7	terminal red	RS PRO	423-239	423-239
switch	7	switch	amazon		
BNC_connector	2	BNC	RS PRO	564-4897	564-4897
power supply1	1	supply5V			
power supply2	1	supply12V			

Table B.1: Components required for the control unit. Data for power supplies are not given since they were reused from previous projects.

Part	Quantity	Designator	Value	Supplier	Order-code	Part number
DAC	1	DAC		Microchip	770-9798	MCP4821-E/P
ADC	1	ADC		Microchip	379-2364	MCP3201-BI/P
op amp	1	OP		Texas Instruments	661-0530	LM324N
optocoupler	7	opto		Vishay	773-3693	VO615A-5
capacitor	2	C1	2.2 uF	RS PRO	520-1321	UVR2W2R2MPD
capacitor	3	C2, C3, C4	0.1uF	Vishay	181-6538	K104M15X7RF53H5
capacitor	1	C5	2.2 uF	RS PRO	711-2012	RS225-400V-RL8x11
trimmer	2	R2, R12	0-50 k	Bourns	769-2195	PV36W503C01B00
connector	2	con6 M		RS PRO	897-1272	CTB9359/6
connector	2	con6 F		RS PRO	897-1228	CTB9209/6
connector	1	con3 M		RS PRO	897-1266	CTB9359/3
connector	1	con3 F		RS PRO	97-1212	CTB9209/3
connector	1	con2 H		Phoenix Contact	193-0592	1729131
IC socket	7	Zdip4		Preci-Dip	702-0644	110-87-304-41-001101
IC socket	2	Zdip8		ASSMANN WSW	674-2435	A 08-LC-TT
IC socket	1	Zdip14		ASSMANN WSW	674-2438	A 14-LC-TT
resistor	1	R1	1 M	RS PRO	707-7903	707-7903
resistor	5	R4, R6-9	100 K	RS PRO	707-8388	RS-Carbon-100k-5%-0.5W
resistor	1	R10	33 K	TE Connectivity	135-960	CFR16J33K
resistor	1	R11	1 K	RS PRO	707-7666	707-7666
resistor	2	R3, R5	220	TE Connectivity	135-819	CFR16J220R

Table B.2: List of components needed for a single *voltage control* board.

Part	Quantity	Designator	Value	Supplier	Order-code	Part number
op amp	1	OP		Texas Instruments	661-0530	LM324N
ADC	1	ADC		Microchip	379-2364	MCP3201-BI/P
digital isolator	1	ISO		Silicon Labs	753-2232	Si8431AB-D-IS1
voltage regulator	1	VREF5V	5V	DiodesZetex	885-5423	AS78L05ZTR-E1
voltage regulator	1	VREF4.1V	4.096V	Microchip	681-1083	MCP1541-I/TO
IC socket	1	Zdip8		ASSMANN WSW	674-2435	A 08-LC-TT
IC socket	1	Zdip14		ASSMANN WSW	674-2438	A 14-LC-TT
package adapter	1	adapter		amazon		
connector	2	con2		Phoenix Contact	193-0586	1729128
connector	1	con6 M		RS PRO	897-1272	897-1272
connector	1	con6 F		RS PRO	897-1228	897-1228
resistor	2	R2-R3	33 K	TE Connectivity	135-960	CFR16J33K
resistor	1	R1	10 K	RS PRO	707-7745	707-7745
trimmer	1	TRIM1	1.2 M	Bourns	785-9723	3296W-1-125LF
capacitor	4	C1	0.1uF	Vishay	181-6538	K104M15X7RF53H5
capacitor	1	C2	2.2 uF	RS PRO	520-1321	UVR2W2R2MPD
capacitor	1	C3	1 uF	AVX	699-5137	SR215E105MARTR2
battery holder	1	PB		RS PRO	185-4797	
battery	1	B	9V			

Table B.3: List of components needed for a single *current read* board.

Bibliography

[1] Abplanalp, M., Eng, L., and Günter, P. (1998). Mapping the domain distribution at ferroelectric surfaces by scanning force microscopy. *Applied Physics A: Materials Science & Processing*, 66(7).

[2] Ahluwalia, G. K. (2017). *Applications of chalcogenides: S, Se, and Te*. Springer.

[3] Antonova, L. and Denissov, V. (1997). High-efficiency photocathodes on the nea-gaas basis. *Applied surface science*, 111:237–240.

[4] Ashcroft, N. and Mermin, N. (2011). *Solid State Physics*. Cengage Learning.

[5] Bahramy, M., Arita, R., and Nagaosa, N. (2011). Origin of giant bulk rashba splitting: Application to bitei. *Physical Review B*, 84(4):041202.

[6] Baskaran, A. and Smereka, P. (2012). Mechanisms of stranski-krastanov growth. *Journal of Applied Physics*, 111(4):044321.

[7] Berry, M. V. (1984). Quantal phase factors accompanying adiabatic changes. *Proceedings of the Royal Society of London. A. Mathematical and Physical Sciences*, 392(1802):45–57.

[8] Bertacco, R., Cantoni, M., Riva, M., Tagliaferri, A., and Ciccacci, F. (2005). Epitaxial growth and characterization of layered magnetic nanostructures. *Applied surface science*, 252(5):1754–1764.

[9] Bertacco, R., De Rossi, S., and Ciccacci, F. (1998a). High-quality fe (001) single crystal films on mgo (001) substrates for electron spectroscopies. *Journal of Vacuum Science & Technology A: Vacuum, Surfaces, and Films*, 16(4):2277–2280.

[10] Bertacco, R., Merano, M., and Ciccacci, F. (1998b). Spin dependent electron absorption in fe (001)-p (1× 1) o: A new candidate for a stable and efficient electron polarization analyzer. *Applied physics letters*, 72(16):2050–2052.

[11] Bigi, C. (2015). Complete photoemission experiment for probing spin texture at surfaces: commissioning of vleed detectors for 3d spin-resolved arpes and first experiments. Master's thesis, Università degli studi di Milano. An optional note.

[12] Bloch, F. (1929). Über die quantenmechanik der elektronen in kristallgittern. *Zeitschrift für physik*, 52(7):555–600.

[13] Blom, P., Wolf, R., Cillessen, J., and Krijn, M. (1994). Ferroelectric schottky diode. *Physical Review Letters*, 73(15):2107.

[14] Boschker, J. E. and Calarco, R. (2017). Growth of crystalline phase change materials by physical deposition methods. *Advances in Physics: X*, 2(3):675–694.

[15] Caldwell, M. A., Jeyasingh, R. G. D., Wong, H.-S. P., and Milliron, D. J. (2012). Nanoscale phase change memory materials. *Nanoscale*, 4(15):4382–4392.

[16] Cantoni, M. and Bertacco, R. (2004). High efficiency apparatus for spin polarized inverse photoemission. *Review of scientific instruments*, 75(7):2387–2392.

[17] Cao, W. (2008). Constructing landau-ginzburg-devonshire type models for ferroelectric systems based on symmetry. *Ferroelectrics*, 375(1):28–39.

[18] Chai, X., Jiang, J., Zhang, Q., Hou, X., Meng, F., Wang, J., Gu, L., Zhang, D. W., and Jiang, A. Q. (2020). Nonvolatile ferroelectric field-effect transistors. *Nature communications*, 11(1):1–9.

[19] Chandra, P. and Littlewood, P. B. (2007). A landau primer for ferroelectrics. In *Physics of ferroelectrics*, pages 69–116. Springer.

[20] Chang, K., Liu, J., Lin, H., Wang, N., Zhao, K., Zhang, A., Jin, F., Zhong, Y., Hu, X., Duan, W., et al. (2016). Discovery of robust in-plane ferroelectricity in atomic-thick snte. *Science*, 353(6296):274–278.

[21] Chiaia, G., De Rossi, S., Mazzolari, L., and Ciccacci, F. (1993). Thin fe films grown on ag (100) studied by angle-and spin-resolved inverse-photoemission spectroscopy. *Physical Review B*, 48(15):11298.

[22] Ciccacci, F., Vescovo, E., Chiaia, G., De Rossi, S., and Tosca, M. (1992). Spin-polarized electron gun for electron spectroscopies. *Review of scientific instruments*, 63(6):3333–3338.

[23] Deringer, V. L., Lumeij, M., and Dronskowski, R. (2012). Ab initio modeling of α-gete (111) surfaces. *The Journal of Physical Chemistry C*, 116(29):15801–15811.

[24] Devonshire, A. (1954). Theory of ferroelectrics. *Advances in physics*, 3(10):85–130.

[25] Di Sante, D., Barone, P., Bertacco, R., and Picozzi, S. (2013). Electric control of the giant rashba effect in bulk gete. *Advanced materials*, 25(4):509–513.

[26] Djani, H., Garcia-Castro, A. C., Tong, W.-Y., Barone, P., Bousquet, E., Picozzi, S., and Ghosez, P. (2019). Rationalizing and engineering rashba spin-splitting in ferroelectric oxides. *npj Quantum Materials*, 4(1):1–6.

[27] Dyakonov, M. I. and Khaetskii, A. (2008). *Spin physics in semiconductors*, volume 157. Springer.

[28] D'Yakonov, M. I. and Perel, V. (1971). Possibility of orienting electron spins with current. *ZhETF Pisma Redaktsiiu*, 13:657.

[29] Fei, Z., Zhao, W., Palomaki, T. A., Sun, B., Miller, M. K., Zhao, Z., Yan, J., Xu, X., and Cobden, D. H. (2018). Ferroelectric switching of a two-dimensional metal. *Nature*, 560(7718):336–339.

[30] Fu, L. (2011). Topological crystalline insulators. *Physical Review Letters*, 106(10):106802.

[31] Fu, L., Kane, C. L., and Mele, E. J. (2007). Topological insulators in three dimensions. *Physical review letters*, 98(10):106803.

[32] Ganichev, S. D., Ivchenko, E., Bel'Kov, V., Tarasenko, S., Sollinger, M., Weiss, D., Wegscheider, W., and Prettl, W. (2002). Spin-galvanic effect. *Nature*, 417(6885):153–156.

[33] Gostein, M. and Sitz, G. O. (1994). An inexpensive high-voltage regulator for charged-particle optics. *Review of scientific instruments*, 65(11):3589–3589.

[34] Guo, L., Kuriki, M., Iijima, H., and Uchida, K. (2017). Nea surface activation of gaas photocathode with different gases. *Surface Science*, 664:65–69.

[35] Hanani, Z. (2020). *Design of flexible lead-free ceramic/biopolymer composite for energy storage and energy harvesting applications*. PhD thesis.

[36] Hankiewicz, E. and Vignale, G. (2009). Spin-hall effect and spin-coulomb drag in doped semiconductors. *Journal of Physics: Condensed Matter*, 21(25):253202.

[37] Hasan, M. Z. and Kane, C. L. (2010). Colloquium: topological insulators. *Reviews of modern physics*, 82(4):3045.

[38] Herman, M. A. and Sitter, H. (2012). *Molecular beam epitaxy: fundamentals and current status*, volume 7. Springer Science & Business Media.

[39] Hoffman, J., Pan, X., Reiner, J. W., Walker, F. J., Han, J., Ahn, C. H., and Ma, T. (2010). Ferroelectric field effect transistors for memory applications.

[40] Hsieh, D., Qian, D., Wray, L., Xia, Y., Hor, Y. S., Cava, R. J., and Hasan, M. Z. (2008). A topological dirac insulator in a quantum spin hall phase. *Nature*, 452(7190):970–974.

[41] Hsieh, T. H., Lin, H., Liu, J., Duan, W., Bansil, A., and Fu, L. (2012). Topological crystalline insulators in the snte material class. *Nature communications*, 3(1):1–7.

[42] Ielmini, D. (2018). Brain-inspired computing with resistive switching memory (rram): Devices, synapses and neural networks. *Microelectronic Engineering*, 190:44–53.

[43] Ielmini, D. and Wong, H.-S. P. (2018). In-memory computing with resistive switching devices. *Nature electronics*, 1(6):333–343.

[44] Iizumi, M., Hamaguchi, Y., F. Komatsubara, K., and Kato, Y. (1975). Phase transition in snte with low carrier concentration. *Journal of the Physical Society of Japan*, 38(2):443–449.

[45] Ishizaka, K., Bahramy, M., Murakawa, H., Sakano, M., Shimojima, T., Sonobe, T., Koizumi, K., Shin, S., Miyahara, H., Kimura, A., et al. (2011). Giant rashba-type spin splitting in bulk bitei. *Nature materials*, 10(7):521–526.

[46] Johnson, P. and Hulbert, S. (1990). Inverse photoemission. *Review of scientific instruments*, 61(9):2277–2288.

[47] Kane, C. L. and Mele, E. J. (2005a). Quantum spin hall effect in graphene. *Physical review letters*, 95(22):226801.

[48] Kane, C. L. and Mele, E. J. (2005b). Z 2 topological order and the quantum spin hall effect. *Physical review letters*, 95(14):146802.

[49] Kang, S. and Lee, K. (2013). Emerging materials and devices in spintronic integrated circuits for energy-smart mobile computing and connectivity. *Acta Materialia*, 61(3):952–973.

[50] Kasap, S. and Capper, P. (2017). *Springer handbook of electronic and photonic materials*. Springer.

[51] Kato, Y. K., Myers, R. C., Gossard, A. C., and Awschalom, D. D. (2004). Observation of the spin hall effect in semiconductors. *science*, 306(5703):1910–1913.

[52] Kessler, J. (1976). Description of polarized electrons. In *Polarized Electrons*, pages 7–20. Springer.

[53] Kimura, T., Otani, Y., Sato, T., Takahashi, S., and Maekawa, S. (2007). Room-temperature reversible spin hall effect. *Physical review letters*, 98(15):156601.

[54] Kolobov, A., Kim, D., Giussani, A., Fons, P., Tominaga, J., Calarco, R., and Gruverman, A. (2014). Ferroelectric switching in epitaxial gete films. *APL Materials*, 2(6):066101.

[55] Kooi, B. J. and Noheda, B. (2016). Ferroelectric chalcogenides—materials at the edge. *Science*, 353(6296):221–222.

[56] Laczkowski, P., Fu, Y., Yang, H., Rojas-Sánchez, J.-C., Noel, P., Pham, V., Zahnd, G., Deranlot, C., Collin, S., Bouard, C., et al. (2017). Large enhancement of the spin hall effect in au by side-jump scattering on ta impurities. *Physical Review B*, 96(14):140405.

[57] Liebmann, M., Rinaldi, C., Di Sante, D., Kellner, J., Pauly, C., Wang, R. N., Boschker, J. E., Giussani, A., Bertoli, S., Cantoni, M., et al. (2016). Giant rashba-type spin splitting in ferroelectric gete (111). *Advanced materials*, 28(3):560–565.

[58] Lines, M. E. and Glass, A. M. (2001). *Principles and applications of ferroelectrics and related materials*. Oxford university press.

[59] Lopez-Varo, P., Bertoluzzi, L., Bisquert, J., Alexe, M., Coll, M., Huang, J., Jimenez-Tejada, J. A., Kirchartz, T., Nechache, R., Rosei, F., et al. (2016). Physical aspects of ferroelectric semiconductors for photovoltaic solar energy conversion. *Physics Reports*, 653:1–40.

[60] Lüth, H. (2001). *Solid surfaces, interfaces and thin films*, volume 4. Springer.

[61] Lv, Y., Kally, J., Zhang, D., Lee, J. S., Jamali, M., Samarth, N., and Wang, J.-P. (2018). Unidirectional spin-hall and rashba- edelstein magnetoresistance in topological insulator-ferromagnet layer heterostructures. *Nature communications*, 9(1):1–7.

[62] Manchon, A., Koo, H. C., Nitta, J., Frolov, S., and Duine, R. (2015). New perspectives for rashba spin–orbit coupling. *Nature materials*, 14(9):871–882.

[63] Manipatruni, S., Nikonov, D. E., Lin, C.-C., Gosavi, T. A., Liu, H., Prasad, B., Huang, Y.-L., Bonturim, E., Ramesh, R., and Young, I. A. (2019). Scalable energy-efficient magnetoelectric spin–orbit logic. *Nature*, 565(7737):35–42.

[64] Markov, I. L. (2014). Limits on fundamental limits to computation. *Nature*, 512(7513):147–154.

[65] Moore, J. E. (2010). The birth of topological insulators. *Nature*, 464(7286):194–198.

[66] Morozovska, A. N., Svechnikov, S. V., Eliseev, E. A., Jesse, S., Rodriguez, B. J., and Kalinin, S. V. (2007). Piezoresponse force spectroscopy of ferroelectric-semiconductor materials. *Journal of Applied Physics*, 102(11):114108.

[67] Morresi, L. (2013). Basics of molecular beam epitaxy (mbe) technique. *Silicon Based Thin Film Sol. Cells, Bentham Science Publishers*, pages 81–107.

[68] Nakahara, M. (2018). *Geometry, topology and physics*. CRC press.

[69] Nakayama, H., Kanno, Y., An, H., Tashiro, T., Haku, S., Nomura, A., and Ando, K. (2016). Rashba-edelstein magnetoresistance in metallic heterostructures. *Physical review letters*, 117(11):116602.

[70] Nessi, L. (2021). *Group-IV tellurides as a playground for enhanced performances in spin and angle-resolved photoemission spectroscopy*. PhD thesis, Doctoral program in Physics, Politecnico di Milano, Piazzale Leonardo da Vinci, Milano.

[71] Noé, P. and Hippert, F. (2018). Structure and properties of chalcogenide materials for pcm. In *Phase Change Memory*, pages 125–179. Springer.

[72] Nomura, K., Koshino, M., and Ryu, S. (2007). Topological delocalization of two-dimensional massless dirac fermions. *Physical review letters*, 99(14):146806.

[73] Osterwalder, J. (2012). Can spin-polarized photoemission measure spin properties in condensed matter? *Journal of Physics: Condensed Matter*, 24(17):171001.

[74] Pendry, J. (1981). Theory of inverse photoemission. *Journal of Physics C: Solid State Physics*, 14(9):1381.

[75] Persad, A. and Ward, C. (2011). Expressions for the evaporation and condensation coefficients in the hertz-knudsen relation. *62nd International Astronautical Congress 2011, IAC 2011*, 1:695–700.

[76] Petaccia, L. (2016). Angle-resolved photoemission spectroscopy (arpes). Elettra, Sincrotrone Trieste, Italy. Lecture Notes.

[77] Picozzi, S. (2014). Ferroelectric rashba semiconductors as a novel class of multifunctional materials. *Frontiers in Physics*, 2:10.

[78] Pierce, D. T., Celotta, R., Wang, G.-C., Unertl, W., Galejs, A., Kuyatt, C., and Mielczarek, S. (1980). The gaas spin polarized electron source. *Review of Scientific Instruments*, 51(4):478–499.

[79] Plekhanov, E., Barone, P., Di Sante, D., and Picozzi, S. (2014). Engineering relativistic effects in ferroelectric snte. *Physical Review B*, 90(16):161108.

[80] Radaelli, G., Petti, D., Plekhanov, E., Fina, I., Torelli, P., Salles, B., Cantoni, M., Rinaldi, C., Gutiérrez, D., Panaccione, G., et al. (2014). Electric control of magnetism at the fe/batio3 interface. *Nature communications*, 5(1):1–9.

[81] Resta, R. and Vanderbilt, D. (2007). Theory of polarization: a modern approach. In *Physics of Ferroelectrics*, pages 31–68. Springer.

[82] Rinaldi, C., Rojas-Sánchez, J., Wang, R., Fu, Y., Oyarzun, S., Vila, L., Bertoli, S., Asa, M., Baldrati, L., Cantoni, M., et al. (2016). Evidence for spin to charge conversion in gete (111). *APL Materials*, 4(3):032501.

[83] Rinaldi, C., Varotto, S., Asa, M., Sławińska, J., Fujii, J., Vinai, G., Cecchi, S., Di Sante, D., Calarco, R., Vobornik, I., et al. (2018). Ferroelectric control of the spin texture in gete. *Nano letters*, 18(5):2751–2758.

[84] Rojas-Sánchez, J.-C., Reyren, N., Laczkowski, P., Savero, W., Attané, J.-P., Deranlot, C., Jamet, M., George, J.-M., Vila, L., and Jaffrès, H. (2014). Spin pumping and inverse spin hall effect in platinum: the essential role of spin-memory loss at metallic interfaces. *Physical review letters*, 112(10):106602.

[85] Rossi, C. (2000). Progetto, realizzazione e test di un'unità di controllo per un nunovo polarimetro ad alta efficienza. Master's thesis, Politecnico of Milan.

[86] Sauerbrey, G. (1959). The use of quarts oscillators for weighing thin layers and for microweighing. *Z. Phys.*, 155:206–222.

[87] Scheer, R. and Schock, H.-W. (2011). *Chalcogenide photovoltaics: physics, technologies, and thin film devices*. John Wiley & Sons.

[88] Scott, J. (2007). Applications of modern ferroelectrics. *science*, 315(5814):954–959.

[89] Sih, V., Myers, R., Kato, Y., Lau, W., Gossard, A., and Awschalom, D. (2005). Spatial imaging of the spin hall effect and current-induced polarization in two-dimensional electron gases. *Nature physics*, 1(1):31–35.

[90] Sławińska, J., Cerasoli, F. T., Wang, H., Postorino, S., Supka, A., Curtarolo, S., Fornari, M., and Nardelli, M. B. (2019). Giant spin hall effect in two-dimensional monochalcogenides. *2D Materials*, 6(2):025012.

[91] Spicer, W., Chye, P., Skeath, P. R., Su, C. Y., and Lindau, I. (1979). New and unified model for schottky barrier and iii–v insulator interface states formation. *Journal of Vacuum Science and Technology*, 16(5):1422–1433.

[92] Stashkevich, A. (2020). Spin-orbitronics a novel trend in spin oriented electronics. . , 22(6):45–54.

[93] Stern, N., Ghosh, S., Xiang, G., Zhu, M., Samarth, N., and Awschalom, D. (2006). Current-induced polarization and the spin hall effect at room temperature. *Physical review letters*, 97(12):126603.

[94] Tanaka, Y., Ren, Z., Sato, T., Nakayama, K., Souma, S., Takahashi, T., Segawa, K., and Ando, Y. (2012). Experimental realization of a topological crystalline insulator in snte. *Nature Physics*, 8(11):800–803.

[95] Tusche, C., Krasyuk, A., and Kirschner, J. (2015). Spin resolved bandstructure imaging with a high resolution momentum microscope. *Ultramicroscopy*, 159:520–529.

[96] Valet, T. and Fert, A. (1993). Theory of the perpendicular magnetoresistance in magnetic multilayers. *Physical Review B*, 48(10):7099.

[97] Varotto, S. (2020). *Nonvolatile control of spin and charge transport in Ferroelectric Rashba Semiconductors*. PhD thesis, Doctoral program in Physics, Politecnico di Milano, Piazzale Leonardo da Vinci, Milano.

[98] Varotto, S., Nessi, L., Cecchi, S., Sławińska, J., Noël, P., Petrò, S., Fagiani, F., Novati, A., Cantoni, M., Petti, D., et al. (2021). Room-temperature ferroelectric switching of spin-to-charge conversion in germanium telluride. *Nature Electronics*, 4(10):740–747.

[99] Vaz, D. C., Barthélémy, A., and Bibes, M. (2018). Oxide spin-orbitronics: New routes towards low-power electrical control of magnetization in oxide heterostructures. *Japanese Journal of Applied Physics*, 57(9):0902A4.

[100] Végh, J. (2006). The shirley background revised. *Journal of electron spectroscopy and related phenomena*, 151(3):159–164.

[101] Vignale, G. (2010). Ten years of spin hall effect. *Journal of superconductivity and novel magnetism*, 23(1):3–10.

[102] Vorotilov, K. A. and Sigov, A. (2012). Ferroelectric memory. *Physics of the Solid State*, 54(5):894–899.

[103] Wang, C.-R., Tung, J.-C., Sankar, R., Hsieh, C.-T., Chien, Y.-Y., Guo, G.-Y., Chou, F., and Lee, W.-L. (2013). Magnetotransport in copper-doped noncentrosymmetric bitei. *Physical Review B*, 88(8):081104.

[104] Wang, R., Boschker, J. E., Bruyer, E., Sante, D. D., Picozzi, S., Perumal, K., Giussani, A., Riechert, H., and Calarco, R. (2014). Toward truly single crystalline gete films: The relevance of the substrate surface. *The Journal of Physical Chemistry C*, 118(51):29724–29730.

[105] Wen, X.-G. (1995). Topological orders and edge excitations in fractional quantum hall states. *Advances in Physics*, 44(5):405–473.

[106] Woodruff, D. (2016). Low energy electron diffraction. In *Reference Module in Materials Science and Materials Engineering*. Elsevier.

[107] Wu, H., Zhang, P., Deng, P., Lan, Q., Pan, Q., Razavi, S. A., Che, X., Huang, L., Dai, B., Wong, K., et al. (2019). Room-temperature spin-orbit torque from topological surface states. *Physical review letters*, 123(20):207205.

[108] Wunderlich, J., Irvine, A., Sinova, J., Park, B. G., Zârbo, L., Xu, X., Kaestner, B., Novák, V., and Jungwirth, T. (2009). Spin-injection hall effect in a planar photovoltaic cell. *Nature Physics*, 5(9):675–681.

[109] Xu, X., Ding, Y., Hu, S. X., Niemier, M., Cong, J., Hu, Y., and Shi, Y. (2018). Scaling for edge inference of deep neural networks. *Nature Electronics*, 1(4):216–222.

[110] Yang, Z., Chang, B., Zou, J., Qiao, J., Gao, P., Zeng, Y., and Li, H. (2007). Comparison between gradient-doping gaas photocathode and uniform-doping gaas photocathode. *Applied Optics*, 46(28):7035–7039.

[111] Zahnd, G., Vila, L., Pham, V., Cosset-Cheneau, M., Lim, W., Brenac, A., Laczkowski, P., Marty, A., and Attané, J. (2018). Spin diffusion length and polarization of ferromagnetic metals measured by the spin-absorption technique in lateral spin valves. *Physical Review B*, 98(17):174414.

[112] Zhang, H., Liu, C.-X., Qi, X.-L., Dai, X., Fang, Z., and Zhang, S.-C. (2009). Topological insulators in bi2se3, bi2te3 and sb2te3 with a single dirac cone on the surface. *Nature physics*, 5(6):438–442.

[113] Zhou, W., Apkarian, R., Wang, Z. L., and Joy, D. (2006). Fundamentals of scanning electron microscopy (sem). In *Scanning microscopy for nanotechnology*, pages 1–40. Springer.

[114] Zhuravlev, M. Y., Sabirianov, R. F., Jaswal, S., and Tsymbal, E. Y. (2005). Giant electroresistance in ferroelectric tunnel junctions. *Physical Review Letters*, 94(24):246802.